

**Assessment of maize crop health and water stress based on
multispectral and thermal infrared unmanned aerial vehicle
phenotyping in smallholder farms**

by

Kiara Brewer

Submitted in fulfilment of the academic requirements of

MASTER OF SCIENCE

in Agrometeorology

Agrometeorology Discipline

School of Agricultural, Earth and Environmental Sciences

College of Agriculture, Engineering and Science

University of KwaZulu-Natal

Pietermaritzburg

South Africa

December 2021

PREFACE

The research contained in this dissertation was completed by the candidate while based in the Discipline of Agrometeorology, School of Agricultural, Earth and Environmental Sciences of the College of Agriculture, Engineering and Science, University of KwaZulu-Natal, Pietermaritzburg, South Africa. The Water Research Commission of South Africa is acknowledged for funding through the WRC Project, No. K5/2971//4, 'Use of drones to monitor crop health, water stress, crop water requirements and improve crop water productivity to enhance precision agriculture and irrigation scheduling'. The research was also financially supported by the National Research Foundation (Grant Number: 122140).

The contents of this work have not been submitted in any form to another university and, except where the work of others is acknowledged in the text, the results reported are due to investigations by the candidate.



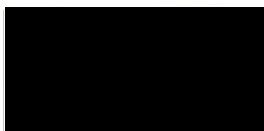
Signed: Professor Alistair Clulow (Supervisor)

Date: 01 December 2021



Signed: Doctor Mbulisi Sibanda (Co-Supervisor)

Date: 01 December 2021



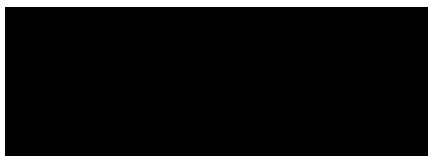
Signed: Professor Tafadzwa Mabhaudhi (Co-Supervisor)

Date: 01 December 2021

DECLARATION: PLAGIARISM

I, Kiara Brewer declare that:

- (i) the research reported in this thesis, except where otherwise indicated or acknowledged, is my original work;
- (ii) this thesis has not been submitted in full or in part for any degree or examination to any other university;
- (iii) this thesis does not contain other persons' data, pictures, graphs or other information, unless specifically acknowledged as being sourced from other persons;
- (iv) this thesis does not contain other persons' writing, unless specifically acknowledged as being sourced from other researchers. Where other written sources have been quoted, then:
 - a) their words have been re-written but the general information attributed to them has been referenced;
 - b) where their exact words have been used, their writing has been placed inside quotation marks, and referenced;
- (v) where I have used material for which publications followed, I have indicated in detail my role in the work;
- (vi) this thesis is primarily a collection of material, prepared by myself, published as journal articles or presented as a poster and oral presentations at conferences. In some cases, additional material has been included;
- (vii) this thesis does not contain text, graphics or tables copied and pasted from the Internet, unless specifically acknowledged, and the source being detailed in the thesis and in the References sections.



Signed: Kiara Brewer

Date: 01 December 2021

ABSTRACT

Smallholder farming systems contribute significantly to agricultural production, livelihood sustenance, and socio-economic growth in developing nations. Despite their relative importance, smallholder farmers tend to lack the resources required to maximize their potential and generally face the challenges of unhealthy and water-stressed crops, resulting in low yields. Hence, it is imperative to provide smallholder farmers with innovative, objective, low-cost solutions to assist them in optimizing productivity. Recent precision agricultural developments, in the form of unmanned aerial vehicles (UAVs) mounted with very high-resolution cameras, provide spatially explicit near real-time information that is useful in monitoring and assessing farm and plot scale crop growth dynamics. The synergistic use of UAV technology with remote sensing techniques allows for a deeper understanding of crop characteristics that could assist with operational decisions related to crop health at the field level, allowing the timely implementation of remedial solutions to ensure productivity.

In light of these recent developments, the focus of the study was to explore the utility of multispectral and thermal infrared UAV technology in determining crop health and water stress levels during different phenological stages. In this regard, the study analyzed maize due to it being the most important staple grain crop that is extensively cultivated in South Africa, especially by smallholder farms, for economic gain and food security. The study utilized crop health and water stress indicators of chlorophyll content, foliar temperature, and stomatal conductance. Specifically, chlorophyll content was used as the main proxy for crop health because of its well-known biochemical pigment that serves as an indicator of plant productivity. Additionally, crop foliar temperature and stomatal conductance were used as proxies for water stress due to their ability to indicate the water content and crop water productivity status. A random forest machine learning algorithm was used to predict chlorophyll, temperature, and stomatal conductance over the various maize phenological stages, and determine the most optimal growth stage(s) for the prediction of each crop characteristic. Furthermore, automated, in-field, time-series data of normalized difference vegetation index (NDVI) and foliar canopy temperature were measured to further understand maize health and water stress over the phenological stages through in-situ measurements.

The remotely sensed UAV data and its synergistic use with the robust machine learning algorithm were able to accurately predict chlorophyll, temperature, and stomatal conductance across phenotyping. Specifically, chlorophyll content was optimally predicted during the early vegetative

(RMSE = 13.9 $\mu\text{mol m}^{-2}$, $R^2 = 0.80$, RRMSE = 11 %), early reproductive (RMSE = 87.4 $\mu\text{mol m}^{-2}$, $R^2 = 0.89$, RRMSE = 7 %) and late vegetative (RMSE = 96.2 $\mu\text{mol m}^{-2}$, $R^2 = 0.85$, RRMSE = 8 %) growth stages through the near-infrared, red-edge, and vegetation indices derived from these sections. The foliar temperature was optimally estimated during the mid-vegetative growth stage (RMSE = 0.59 $^{\circ}\text{C}$, $R^2 = 0.81$, RRMSE = 2.6 %) through the thermal infrared, near-infrared, red-edge, and UAV-derived vegetation indices. Finally, stomatal conductance was optimally predicted during the early reproductive growth stage (RMSE = 25.9 $\text{mmol m}^{-2} \text{s}^{-1}$, $R^2 = 0.85$, RRMSE = 11.5 %) through the thermal infrared, near-infrared red-edge, and UAV-derived vegetation indices. The resulting maps of chlorophyll, temperature and stomatal conductance variation captured the spatial heterogeneity over the maize field for the various growth stages. The maize crop was found to be relatively healthy throughout phenotyping; however, it suffered mild water stress during the early vegetative stage and after an unforeseen hailstorm during the mid and late reproductive stages.

Smallholder farming is seldom the focus of innovation and precision agriculture. However, this study illustrated the use of smart agro-climatic, high-resolution and quick turn around technology for smallholder agricultural systems. Such technology provides smallholder farmers with important in-field information on crop biophysical factors allowing them to make informed, tactical decisions for improved interventions on crop management through various stages of phenology.

ACKNOWLEDGMENTS

Firstly, thanks to God Almighty who has provided me with the opportunity to reach my postgraduate studies and conduct research at a Masters level. Jesus, you have kept me optimistic when the going got tough, allowed me to realize my potential, and most importantly kept me healthy, and strong during these challenging times of the COVID-19 pandemic. Thank you, Lord. Amen.

“It takes a village to raise a child”, so does it to conduct successful research in academia. Thus, I would like to extend my thanks and uttermost gratitude to the host of institutions and individuals who contributed to the successful completion of my Master of Science Degree. Thank you to the following:

- The Water Research Commission (WRC) Project No K5/2971//4 for allowing me to be a part of the team and conduct much required research. It has been such an enriching and fulfilling project to be a part of. I will forever be grateful to be part and parcel of research tailored to 4th Industrial Revolution and the trajectory the world is now on.
- The University of KwaZulu-Natal for supporting my higher education since 2016. I am thankful to have obtained a Bachelors, Honours and Masters degree through such a renowned institution.
- My supervisors, Professor Alistair Clulow, Doctor Mbulisi Sibanda, and Professor Tafadzwanashe Mabhaudhi for their constant guidance, support, and assistance. I cannot thank you all enough for being great mentors, always providing me with valuable advice and the enthusiasm to conduct my research. I truly value being a part of your niche and hope to continue my research journey with you all in the future.
- My family, Claudele, Andrew, Kaidan and Michael for their ongoing motivation, love, and reassurance, which allowed me to successfully complete my Masters degree. You have been the backbone of my development as an individual, and I thank you for always encouraging me to strive for excellence.
- The Agrometeorology department, especially Vivek Naiken for his unwavering assistance in the field and laboratory. I am so appreciative of the constant advice and assistance you provided.

- A special thanks to Shaeden Gokool, Vimbayi Chimoyo and Trylee Matongera for their research guidance and assistance with the fieldwork. You are all great researchers that students at my level should strive to become. Thank you for everything.
- The Geography department, especially Professor Onesimo Mutanga and Professor John Odindi for their assistance throughout. Thank you both for being great mentors and assisting in areas I fell short.
- I would like to acknowledge my colleagues, Helen Ndlovu, Siphiwokuhle Buthelezi, Amanda Nyawose for all their assistance. I wish you all success in the future.
- Furthermore, the smallholder farming community of Swayimane for all their efforts throughout the duration of this project.

This work is based on the research supported by the Water Research Commission of South Africa through the WRC Project No. K5/2971//4, ‘Use of drones to monitor crop health, water stress, crop water requirements and improve crop water productivity to enhance precision agriculture and irrigation scheduling’ and the National Research Foundation of South Africa (Grant Number: 122140).

TABLE OF CONTENTS

	<u>Page</u>
PREFACE.....	I
DECLARATION: PLAGIARISM.....	II
ABSTRACT.....	III
ACKNOWLEDGMENTS	V
TABLE OF CONTENTS.....	VII
LIST OF ACRONYMS	X
LIST OF TABLES.....	XI
LIST OF FIGURES	XII
CHAPTER 1: INTRODUCTION	1
1.1. Background of the study	1
1.2. Aim	3
1.3. Objectives	4
1.4. Research questions.....	4
1.5. Thesis structure	4
CHAPTER 2: PREDICTION OF THE CHLOROPHYLL CONTENT OF MAIZE USUNG OVER UAV BASED PHENOTYPING AS A PROXY FOR CROP HEALTH IN SMALLHOLDER FARMING SYSTEMS (PAPER 1).....	7
ABSTRACT	7
2.1. INTRODUCTION.....	8
2.2. MATERIALS AND METHODS	11
2.2.1. Study site description.....	11
2.2.2. Maize phenotyping.....	13
2.2.3. Field data collection, sampling, and survey.....	14
2.2.4. UAV multispectral-thermal camera and platform	16
2.2.5. Image acquisition and processing	18
2.2.6. Statistical analysis.....	20

2.2.7. Accuracy assessment	21
2.3. Results.....	21
2.3.1. Descriptive analysis of UAV-derived data and ground-based maize data	21
2.3.2. Descriptive statistics of chlorophyll content from SPAD.....	23
2.3.3. Random forest models of maize chlorophyll content	24
2.4. Discussion	27
2.5. Conclusion	30

CHAPTER 3: ESTIMATION OF FOLIAR TEMPERATURE AND STOMATAL CONDUCTANCE VARIABILITY AS A PROXY FOR MAIZE WATER STRESS USING UNMANNED AERIAL VEHICLE BASED PHENOTYPING IN SMALLHOLDER FARMS (PAPER 2).....33

Abstract.....	33
3.1. Introduction.....	34
3.2. Materials and Methods.....	36
3.2.1. Study site description.....	36
3.2.2. The maize growth cycle and characteristics	38
3.2.3. Field data collection, temperature, and stomatal conductance measurements.....	39
3.2.4. UAV: DJI Matrice 300 and MicaSense Altum	42
3.2.5. Image acquisition and processing	43
3.2.6. Statistical Analysis.....	45
3.2.7. Accuracy assessment	47
3.3. Results.....	47
3.3.1. Descriptive analysis of UAV-derived data and SI-111 IRR maize temperature data.....	47
3.3.2. Descriptive statistics of in-situ maize temperature and stomatal conductance measurements.....	49
3.3.3. UAV-derived data: estimation of maize temperature and stomatal conductance.....	52
3.4. Discussion	58
3.4.1. Prediction of maize water stress using foliar temperature and stomatal conductance.....	58
3.4.2. Implications of the study.....	61
3.5. Conclusion	62

CHAPTER 4: SYNTHESIS AND CONCLUSIONS64

4.1. A reflection of using UAV-derived data for crop health and water stress.....64

4.2. Limitations and recommendations for future research65

REFERENCES.....66

APPENDIX A76

LIST OF ACRONYMS

CRP	Calibrated reflectance panel
DEM	Digital elevation model
DOY	Day of year
FOV	Field of view
GPS	Global positioning system
GSD	Ground sampling distance
NDVI	Normalized difference vegetation index
NIR	Near infrared
IRR	Infrared radiometer
IRT	Infrared thermometer
LWIR	Long wave infrared
R ²	Coefficient of determination
RMSE	Root mean squared error
RRMSE	Relative root mean squared error
SPAD	Soil plant analysis development
SRS	Spectral reflectance sensors
T _c	Canopy temperature
T _a	Air temperature
UAV	Unmanned aerial vehicle
VHR	Very high resolution
VI _s	Vegetation indices
VTOL	Vertical take-off and landing

LIST OF TABLES

<u>Table</u>	<u>Page</u>
Table 1: Maize growth stages and characteristics.....	13
Table 2: MicaSense Altum camera specifications.....	17
Table 3: UAV flight specifications.....	18
Table 4: Spectral UAV-derived vegetation indices used to predict chlorophyll content	19
Table 5: Descriptive statistics of maize chlorophyll content throughout the various growth stages...	24
Table 6: Maize growth stages	39
Table 7: MicaSense Altum camera specifications.....	43
Table 8: UAV flight specifications.....	44
Table 9: Spectral vegetation indices utilized to predict foliar temperature and stomatal conductance	46
Table 10: Descriptive statistics of IRR and IRT foliar temperature throughout the maize growth stages	50
Table 11: Descriptive statistics of stomatal conductance throughout the maize phenological cycle ..	51

LIST OF FIGURES

<u>Figure</u>	<u>Page</u>
Figure 1: Swayimane weather conditions over the period of maize phenotyping.....	12
Figure 2: Location of the Swayimane study area, study site, and smallholder maize field.....	12
Figure 3: (a) Automated in-field meteorological tower in the maize field, (b) meteorological tower mounted with SRS-NDVI and SRS-PRI sensors held 4-meters above the ground, (c) CR1000 data logger, Em50 datalogger and 12 V battery.	15
Figure 4: (a) DJI Matrice 300 platform and, (b) MicaSense Altum multispectral-thermal camera	17
Figure 5: (a) DJI M-300 flight plan, (b) MicaSense Altum calibration reflectance panel.....	18
Figure 6: Daily SRS-NDVI values of maize throughout the phenological cycle. Red points indicate the days of field visits to collect field data. Blue point indicates day of crop disturbance due to a hailstorm.	22
Figure 7: Correlation of (a) in-field sensor SRS-NDVI and UAV-derived NDVI (b) measured maize chlorophyll content and UAV-derived NDVI across the maize growth stages.....	23
Figure 8: Linear relationships between measured and predicted maize chlorophyll content for vegetative stages (a) V5 – V10, (b) V12, (c) V14 to VT, and reproductive stages (d) R1 – R3, (e) R3 – R4, (f) R5 – R6.	25
Figure 9: Variable importance scores of optimal chlorophyll content VIs and bands for vegetative stages (a) V5 – V10, (b) V12, (c) V14 to VT, and reproductive stages (d) R1 – R3, (e) R3 – R4, (f) R5 – R6.....	26
Figure 10: Spatial distribution of chlorophyll content over the maize field for vegetative stages (a) V5 – V10, (b) V12, (c) V14 to VT, and reproductive stages (d) R1 – R3, (e) R3 – R4, (f) R5 – R6.	27
Figure 11: Location of the Swayimane study area, study site, and smallholder maize field.....	37
Figure 12: Daily weather conditions in Swayimane over the period of maize phenotyping.....	38

Figure 13: (a) Automated in-field meteorological tower in the maize field, (b) meteorological tower mounted with SI-111 Apogee IRR sensors held 4-meters above the ground, (c) CR1000 data logger, Em50 datalogger and 12 V battery40

Figure 14: (a) DJI Matrice 300 UAV platform and, (b) MicaSense Altum multispectral-thermal camera43

Figure 15: (a) DJI M-300 flight plan, (b) MicaSense Altum calibration reflectance panel.....44

Figure 16: Daily average $T_c - T_a$, solar radiation, and rainfall throughout the maize phenological cycle.48

Figure 17: Correlation of in-field IRR sensors and UAV-derived temperature throughout the maize phenological cycle49

Figure 18: Correlation of foliar temperature and stomatal conductance throughout the maize phenological cycle52

Figure 19: Regression models displaying the relationships between measured and predicted IRT foliar temperature and stomatal conductance throughout the maize phenological cycle: (a) V5 – V10, (b) V12, (c) V14 to VT, (d) R1 – R3, (e) R3 – R4, (f) R5 – R654

Figure 20: Variable importance scores of optimal foliar temperature and stomatal conductance bands and VIs throughout the phenological cycle: (a) V5 – V10, (b) V12, (c) V14 to VT, (d) R1 – R3, (e) R3 – R4, (f) R5 – R655

Figure 21: Foliar temperature of maize over the smallholder field for vegetative stages (a) V5 – V10, (b) V12, (c) V14 to VT, and reproductive stages (d) R1 – R3, (e) R3 – R4, (f) R5 – R6.56

Figure 22: Maize stomatal conductance over the smallholder field for vegetative stages (a) V5 – V10, (b) V12, (c) V14 to VT, and reproductive stages (d) R1 – R3, (e) R3 – R4, (f) R5 – R6.57

Figure 23 (a – d): Photographs of western portion of maize field (lower slope) where weeds/grasses were still present during mid-vegetative growth.76

CHAPTER 1: INTRODUCTION

1.1. Background of the study

The demand for agricultural products is fuelled by the ever-increasing worldwide population, which is expected to reach 9 billion people by 2050 (Nhamo et al., 2020). An additional 2.4 billion people are expected to be concentrated in developing regions such as sub-Saharan Africa by 2050, placing a further strain on agricultural production, even though more than 20% of the population is already food insecure (Lipper et al., 2014). Additional impacts of weather and climate further challenge agriculture, especially in smallholder agricultural systems that are dependent on rainfall for irrigation needs (Kurukulasuriya and Ajwad, 2007). Maize (*Zea mays L.*) is a staple grain crop grown in South Africa, and its yields account for over 50 % of the population's energy needs (Dhau et al., 2018). Amongst rural smallholder farmers, maize is a favoured crop and is predominantly cultivated for socio-economic growth, food security and livelihood sustenance (Abraha and Savage, 2006; Adisa et al., 2018). However, the reduced seasonal rainfall and high maximum temperatures of this decade, have caused inconsistencies in the growth and overall health of maize crops (Adisa et al., 2018). Consequently, smallholder farmers face challenges of unproductive and water-stressed crop yields that are generally lower than the potential of the land (Adisa et al., 2018; Walker et al., 2018). Specifically, in South Africa, the majority of smallholder farms are located in rural areas and generally lack the resources of larger-scale commercial agriculture (Thamaga-Chitja and Morojele, 2014). Such resource limitations reduce the productivity and potential of smallholder fields, as most of the on-farm decisions are based on indigenous knowledge (Soropa et al., 2015). To remedy such situations, rural smallholder farmers require innovative, objective, and low-cost solutions to assist them in gaining a deeper understanding of their crop productivity and to ensure a sustainable provision of food security (Baiphethi and Jacobs, 2009; Kumar and Sharma, 2013; Nhamo et al., 2020).

Several studies have illustrated the potential use of remote sensing technologies for agricultural applications; however, these applications typically use satellite-borne earth observation or manned aerial vehicles (Manfreda et al., 2018). Satellite-earth observation data is known to provide useful datasets at various spatial, spectral, and temporal resolutions (Dube and Mutanga, 2015; Slagter et al., 2020; Timothy et al., 2016). However, the major limitation of freely available satellite imagery is the spatial resolution, which is generally far too coarse to capture the spatial heterogeneity of small-scale farms and fields (Sandbrook, 2015). Moreover, satellite revisit times and the influence of atmospheric

perturbations such as cloud cover, reduce the frequency of data capture and processing (Manfreda et al., 2018; Nhamo et al., 2020). Nevertheless, there are available satellite-borne observation datasets and manned aerial vehicles that are capable of overcoming such spatio-temporal resolution issues. These include Hyperion Earth Observing (EO)-1, Airborne Visible/Infrared Imaging Spectrometer (AVIRIS), Compact Airborne Spectrographic Imager (CASI) among others (Vorovencii, 2009). However, there are often far too costly for smallholder agricultural applications (Cucho-Padin et al., 2020). In recent years, precision agricultural practices facilitated by unmanned aerial vehicles (UAVs), commonly known as drones, have emerged as an option for small-scale agricultural remote sensing applications (Hoffmann et al., 2016; Hu et al., 2021; Messina and Modica, 2020). UAVs offer vast potential for smallholder applications, as the low-flying altitudes capture data at very-high spatial resolutions (up to a centimetre), as well as at various spectral resolutions that depend on the on-board camera (Maes and Steppe, 2019; Nhamo et al., 2020). Moreover, data is captured in almost near real-time at user-determined temporal intervals and ground sampling distances, which is useful for detecting and mapping phenological growth changes and individual crop canopy patches (Cucho-Padin et al., 2020). Thus, the use of such objective and time-efficient technology holds significant potential for providing near real-time agrometeorological data that informs farmers as to the status of their crops throughout phenotyping.

Advanced multispectral and thermal infrared UAV data makes crop image data analytics and objective assessments of crop characteristics possible. Existing research literature documents various indicators of crop health and water stress (Ahumada-Orellana et al., 2019; Carroll et al., 2017; Hernández-Clemente et al., 2019; Miller et al., 2020). Specifically, crop health and water stress can be detected based on three optical crop elements: (1) chlorophyll content, (2) foliar temperature, and (3) stomatal conductance. Generally, a crop is productive when there are dynamic photosynthetic rates, which result in strong chlorophyll concentrations, low foliar temperatures, and high levels of stomatal conductance. Specifically, the vigorous green pigments in the leaves are indicative of the plant chlorophyll content, informing on the state of the crops' biochemical productivity and overall health. Moreover, the photosynthetic productivity of the crop is also a result of dynamic stomatal conductance rates, which are affected by the crop moisture content and rate of transpiration. Hence, lower foliar temperatures are experienced by the crop when there are optimal rates of stomatal conductance and higher chlorophyll concentrations, indicating a healthy and productive crop with minimal water stress. Thus, the determination of chlorophyll content, foliar temperature, and stomatal conductance are often used as proxies for the evaluation of crop health and water stress through time i.e. growth season (Zhang et al., 2019c)

The three aforementioned crop characteristics are typically predicted through proximal remote sensing techniques premised on the reflectance of chloroplasts and foliar water molecules in the near-infrared (NIR) and shortwave infrared regions of the electromagnetic spectrum. Generally, most UAV-based assessments of crop health and water stress have assessed the use of the visible and NIR regions of the spectrum, yet few studies have assessed the utility of UAV red-edge and thermal infrared sections (Zhang et al., 2019a). Additionally, literature has illustrated the use of vegetation indices (VIs) from various sections of the electromagnetic spectrum to extract vegetation health and water status characteristics, whilst maximizing factors of soil background reflectance, sun angle effects or atmospheric effects (Matongera et al., 2017; Tahir et al., 2018; Zhang et al., 2019a). The most common indices used to evaluate crop health and water stress are the normalized difference vegetation index (NDVI), canopy chlorophyll content index (CCCI), red-edge chlorophyll index ($CI_{rededge}$), and the normalized difference water index (NDWI) amongst a variety of others (El-Hendawy et al., 2019; Liang et al., 2018; Zarco-Tejada et al., 2012; Zhang and Zhou, 2019). Furthermore, the use of machine learning algorithms such as the random forest, support vector machines and multiple linear regression, have proven to be instrumental in characterizing crop characteristics such as the water and health status of plants (Abdel-Rahman et al., 2013; Guo et al., 2020; Han et al., 2019; Hassanijalilian et al., 2020). The random forest ensemble has been widely proven to outperform the other two aforementioned algorithms (Ramos et al., 2020; Yao et al., 2013). Hence, it was anticipated that the use of UAV-derived data (spectral and thermal infrared bands with VIs) coupled with robust random forest regression could produce accurate estimations of chlorophyll, foliar temperature, and stomatal conductance as indicators of crop health and water stress in smallholder farms.

Although UAV remote sensing techniques have become a useful tool for predicting biophysical and biochemical components of crops, there are limited studies that have evaluated the utility of UAV-derived data in combination with machine learning algorithms to estimate crop health and water stress for smallholder farmers. Therefore, it is imperative that indicators of crop health and water stress such as chlorophyll, foliar temperature, and stomatal conductance are predicted, as findings of such crop factors over the various growth stages could provide useful information for smallholder farmers.

1.2. Aim

The aim of the research is to test the utility of multispectral and thermal infrared UAV-derived data in predicting maize crop health and water stress through indicators of chlorophyll, foliar temperature, and stomatal conductance.

1.3. Objectives

In this respect, the study seeks to:

1. Predict the chlorophyll content of maize over UAV based phenotyping as a proxy for crop health in smallholder farming systems,
2. Estimate foliar temperature and stomatal conductance variability as a proxy for maize water stress using UAV based phenotyping in smallholder farms.

1.4. Research Questions

1. At which phenological stage can UAV-derived multispectral remotely sensed data accurately predict the chlorophyll content variability of maize as a proxy for its overall health across the growing cycle?
2. At which stage can foliar temperature and stomatal conductance of maize variability be accurately estimated using multispectral and thermal UAV-derived data as a proxy for water stress in smallholder crop fields?

1.5. Thesis Structure

The thesis contains four chapters, two of which may be regarded as standalone manuscripts (Chapters 2 and 3). As such, the two chapters have their own introduction, materials and methods, results, discussion, and conclusion sections. It should be noted that the two chapters contain similarities as they address the same overarching aim of the study. The chapters are presented as follows:

Chapter One provides a general introduction to the thesis, outlining the use of UAV-derived data in estimating the health and water stress of maize in smallholder farms. The research aim, objectives, and research questions are included in this chapter.

Chapter Two serves as the first standalone manuscript which predicts maize chlorophyll concentrations using multispectral UAV-derived data coupled with a random forest regression to understand the maize crop health of the smallholder farm. This was achieved throughout maize phenotyping. Automated in-field time-series data of NDVI was also utilized to further understand the crop health over maize phenotyping.

Chapter Three, the second manuscript, estimates the foliar temperature and stomatal conductance of maize over phenotyping to understand potential water stress of the smallholder farm. This was done throughout the various growth stages of maize. Continuous in-field crop temperature measurements and meteorological data were used to further understand crop water stress over the maize growing cycle.

Chapter Four consolidates the findings of the study by synthesizing all the findings and conclusions from **Chapter Two** and **Chapter Three**. In addition, this chapter addresses limitations of the study and techniques and makes recommendations for future research.

Lead into Chapter 2:

Smallholder farmers depend on healthy crop yields, due to crops of higher productivity generally providing a greater source of revenue at sale. Consequently, smallholder farmers need to monitor crops throughout phenotyping to ensure that they remain healthy; however, they tend to lack the resource to do so. Objective and low-cost technological solutions such as UAVs and its derived data, are useful in assisting smallholder farmers in optimizing their productivity. Specifically, maize crop health can be optimally estimated through the indicator of chlorophyll, due to its vigorous green-pigment concentrations found in the foliar canopy. In this regard, Chapter 2 determines the maize crop health status of a Swayimane smallholder farm, through the prediction of maize chlorophyll concentrations over the various phenological stages and uses in-situ NDVI measurements to enhance crop health conclusions. Furthermore, prediction of the most optimal maize chlorophyll stage is determined using the random forest regression models. The findings from this chapter demonstrate the utility of UAV-derived data and further assist smallholder farmers in improving management throughout the various stages of maize growth.

CHAPTER 2: PREDICTION OF THE CHLOROPHYLL CONTENT OF MAIZE USUNG OVER UAV BASED PHENOTYPING AS A PROXY FOR CROP HEALTH IN SMALLHOLDER FARMING SYSTEMS (PAPER 1)¹

Abstract

Smallholder farmers are reliant on healthy and productive crop yields to sustain their socio-economic status and ensure livelihood security. Recent advances in South African precision agriculture, in the form of unmanned aerial vehicles (UAVs), provide spatially explicit, almost near real-time information that can be used to assess crop dynamics and inform smallholder farmers. The use of UAVs with remote sensing techniques allows for high spatial resolution data to be captured at various spatio-temporal resolutions, which is particularly useful towards the field and farm scale applications in smallholder farming systems. Specifically, crop chlorophyll content is assessed as it is one of the most well-known and reliable indicators of crop health, due to its biophysical pigment and biochemical processes that suggest plant productivity. In this regard, the study evaluated the utility of multispectral UAV imagery using a random forest machine learning algorithm, in order to estimate the chlorophyll content of maize through the various growth stages. The random forest model required in-field chlorophyll data that was collected for training and validation. The results illustrated that the near-infrared and red-edge wavebands, as well as vegetation indices derived from these wavelengths were fundamental in estimating chlorophyll content throughout maize phenotyping. Furthermore, the random forest model optimally estimated the chlorophyll content of maize over the various phenological stages. Particularly, maize chlorophyll was best predicted during the early vegetative, late vegetative, and early reproductive growth stages to RMSE accuracies of 13.9 $\mu\text{mol m}^{-2}$, 96.2 $\mu\text{mol m}^{-2}$, 87.4 $\mu\text{mol m}^{-2}$, respectively. The least accurate chlorophyll content results were predicted during the mid-reproductive and late reproductive growth stages to RMSE accuracies of 76.2 $\mu\text{mol m}^{-2}$ and 31.3 $\mu\text{mol m}^{-2}$, respectively, as a consequence of a hailstorm. A resultant chlorophyll variation map of the maize growth stages captured the spatial heterogeneity of chlorophyll within the maize field. Therefore, the findings of the study demonstrate that the use of UAV multispectral and thermal imagery with a robust machine algorithm is a critical tool to support the decision-making and management on smallholder farms.

¹ This chapter has been submitted for publication and is currently under review by the Journal of Remote Sensing (MDPI)

Keywords: drones, precision agriculture, random forest, vegetation indices, unmanned aerial vehicles

2.1. Introduction

Smallholder agricultural systems contribute significantly to agricultural production, livelihood sustenance, and socio-economic growth in developing nations (Kamara et al., 2019). Specifically, in sub-Saharan Africa, smallholder farming practices are threatened by a decline in productivity and profitability due to the recent and ongoing effects of climatic variability (Adisa et al., 2018; Salami et al., 2010; Vanlauwe et al., 2014). Maize (*Zea mays L.*) is one of the staple grain crops grown in South Africa and is extensively cultivated at a subsistence scale for household economic gain, food security, and for feedlots (Adisa et al., 2018; Tefera et al., 2011). Smallholder farmers typically cultivate maize under rainfed conditions, where they aim to maximize production and produce healthy crop yields. Despite the goals of smallholder farmers to optimise yields, small-scale farming systems often face a variety of challenges (Adisa et al., 2018; Uganai and Murwira, 2010). Their dependence on rainfall poses a significant threat to crop yields, as a reduced seasonal rainfall and severe weather phenomena impact the overall health, biochemical processes, and physical development of crops (Muzari et al., 2012; Okonya et al., 2013). Smallholder farms also lack the resources required to maximise their potential and are often faced with low unproductive yields that are significantly lower than the potential of the land (Walker and Schulze, 2006). Hence, it is imperative to provide smallholder farmers with innovative, effective, low-cost solutions to assist them in optimising their productivity to produce increased and healthy yields (Nhamo et al., 2020; Shi et al., 2016). Therefore, a deeper understanding of crop dynamics could assist smallholder farmers in identifying crop health issues at an early stage, allowing them to implement the necessary remedial solutions to ensure productivity.

Literature has documented various indicators of crop health (Hernández-Clemente et al., 2019; Nicholls et al., 2004; Whitford et al., 1998); however, chlorophyll content has been identified as one of the most important and reliable health and productivity indicators (Flynn et al., 2020). This is due to the biophysical pigment in the leaves and biochemical photosynthetic processes that suggest plant productivity (Tahir et al., 2018; Terashima et al., 2009). Hence, monitoring its concentration and variability in plants could aid in evaluating crop productivity through time (Zhang et al., 2019c), which is significant towards detecting subtle crop changes and optimising healthy yields in smallholder farming practices (Afzal and Mousavi, 2008; Li et al., 2015).

For many years, advanced and objective tools such as remote sensing have been used to estimate and monitor agricultural vegetative health and productivity (Pinter Jr et al., 2003; Wu et al., 2014). For example, Sibanda et al. (2020) estimated the foliar chlorophyll content of grasses using field-based hyperspectral data, Delegido et al. (2011) estimated the chlorophyll content of multiple agricultural crops using Sentinel-2 red-edge bands, and Kooistra and Clevers (2016) estimated the chlorophyll content in potato leaves using vegetation indices derived from RapidEye satellite imagery. Such studies have illustrated the use of remote sensing as a powerful tool in characterising chlorophyll concentrations in different vegetation, and thus, at a farm scale, it may be useful to use chlorophyll as a proxy for crop health and productivity (Kanning et al., 2018).

Remote sensing techniques obtain the potential to monitor crop productivity and map its spatial distribution based on high-resolution images of varied wavelengths (Duveiller et al., 2013; Miao et al., 2009; Nhamo et al., 2020). Conventional applications of earth observation techniques use satellite borne earth observation or manned aerial vehicles (Berra and Peppia, 2020; Nhamo et al., 2018). However, a major constraint of freely available satellite borne data is its inability to fulfil the ever-increasing need for high spatial and temporal resolution data, which is necessary for monitoring small-scale crop properties throughout phenotyping (Psirofonina et al., 2017). Moreover, manned aerial vehicles can overcome the issues of spatio-temporal resolution, but the associated costs are a major limitation for smallholder farms.

In recent years, unmanned aerial vehicles (UAVs) have been globally recognized as an innovative, low-cost, and effective precision technology for agricultural applications. UAVs offer state-of-the-art image data throughput analytics at very high resolutions (VHR) and have proven to be effective in overcoming the limitations of satellite imagery (Maes and Steppe, 2019; Nhamo et al., 2020). There is great potential for UAVs in small-scale agriculture as the low-flying altitudes capture VHR spatial and spectral data. High resolution images are acquired by multispectral cameras mounted onboard UAVs, which offer almost near real-time data that is critical for monitoring subtle shifts in crop phenology and crop vigour. Moreover, UAVs can be deployed frequently at user-determined ground sampling distances and revisit times, which is impossible with conventional freely accessible satellite-borne sensors such as Landsat 8 Operational Land Imager or Sentinel 2 Multispectral Instrument (Xiang and Tian, 2011). Thus, VHR UAV imagery has the ability to detect individual maize plants, canopy patches and ultimately, phenological growth patterns over the fragmented smallholder fields. Therefore, accurate mapping and analysis of smallholder maize fields using a VHR UAV holds significant

potential for providing data that could inform farmers on the health status of their crops through the phenological cycle.

Specifically, multispectral chlorophyll data can be optimally assessed through the use of UAV-derived vegetation indices (VIs) and a robust machine learning algorithm. VIs are mathematical transformations of image bands that are used quantitatively to extract spectral properties such as canopy cover, plant vigour and phenological dynamics (Khan et al., 2018; Xue and Su, 2017). The most common index used for plant health is the normalized difference vegetation index (NDVI), which is directly used to acquire information on the physiological health status of crops and crop growth changes (Boken and Shaykewich, 2002; Gitelson et al., 2014). Particularly, chlorophyll specific VIs have proven to be more valuable than normalized VIs in some instances as they include a variety of combinations from bands which reflect highly in vegetation (Wu et al., 2014). Such indices include the canopy chlorophyll content index (CCCI) and the modified chlorophyll absorption ratio index (MCARI), which have shown significant correlations to crop chlorophyll content (Haboudane et al., 2002; Raper and Varco, 2015). Furthermore, machine learning algorithms such as random forest, support vector machines and multiple linear regressions have proven to be instrumental in characterising crop chlorophyll content and health status (Abdel-Rahman et al., 2013; Guo et al., 2020; Han et al., 2019; Hassanijalilian et al., 2020). The random forest ensemble has been widely proven to outperform the other two aforementioned algorithms (Ramos et al., 2020; Yao et al., 2013). Hence, it is anticipated that the use of UAV-derived data (spectral bands and VIs) with robust random forest regression could produce accurate results to quantitatively assess the chlorophyll content of maize as an indicator of health in smallholder farms.

Thus, with maize being one of the dominant food crops grown across South Africa, there is a need to assess its health in smallholder agricultural systems through a robust multispectral sensor. A multispectral sensor enables proximal remote sensing analysis of maize and can potentially predict chlorophyll content, which serves as an informant on the health status of the crop. In this regard, this study aims to investigate the potential of multispectral UAV-derived data to assess maize crop chlorophyll content using the random forest model simulation, for an improved understanding of crop health and productivity in smallholder agricultural systems. Therefore, the objectives of the study were to: (1) estimate chlorophyll content variations across the different maize phenological stages using UAV-derived data, (2) determine the optimal maize growth stage(s) for chlorophyll model prediction.

2.2. Materials and Methods

2.2.1. Study site description

The research was conducted over a period of four months from February 2021 to May 2021 in the rural area of Swayimane, KwaZulu-Natal (29°31'24''S; 30°41'37'' E). Swayimane is in the uMshwathi Local Municipality and is located approximately 55 km north-east of Pietermaritzburg. The small, communal area covers a geographical extent of approximately 36 km², and land use is dominated by the smallholder farming systems of the local community. Common crops cultivated in the area include white and yellow maize, sugarcane, amadumbe (*taro*), and sweet potato. The smallholder farmers follow traditional farming methods of planting, maintaining, and manual harvesting of crops. Farm plots are rainfed, fertilized using livestock manure and hand-weeded by farmers. Alternatively, herbicide backpack sprayers are used by small growers to control weeds and grass. The area is predominantly characterized by semi-subsistence farming which is regarded as a form of food security and livelihood sustenance. The produce is sold at local markets for economic benefits, which sustain farmers' livelihoods.

Agriculture and crop production in Swayimane are supported by the favourable environmental conditions of the region. The climate is characterised by warm wet summers and cool dry winters, with an annual average air temperature of approximately 18 °C. The mean annual rainfall ranges between 600 and 1200 mm, with the majority of rain occurring during the summer in the form of thunderstorms. During the research period, Swayimane had a maximum average air temperature of 24 °C and total rainfall of 242.8 mm, amongst other weather data (Figure 1). Weather conditions were continuously monitored by the automatic weather station installed at a Swayimane high school. Weather data was downloaded from the Swayimane weather website. The weather station is situated approximately 2 km from the smallholder maize farm, and as such it is proximally adequate in capturing the weather conditions of the study site. The research was conducted on a 30 × 96 (2850 m²) smallholder maize field (Figure 2). The field was located on a slope that obtained a ranging field elevation of approximately 850 m to 839 m.

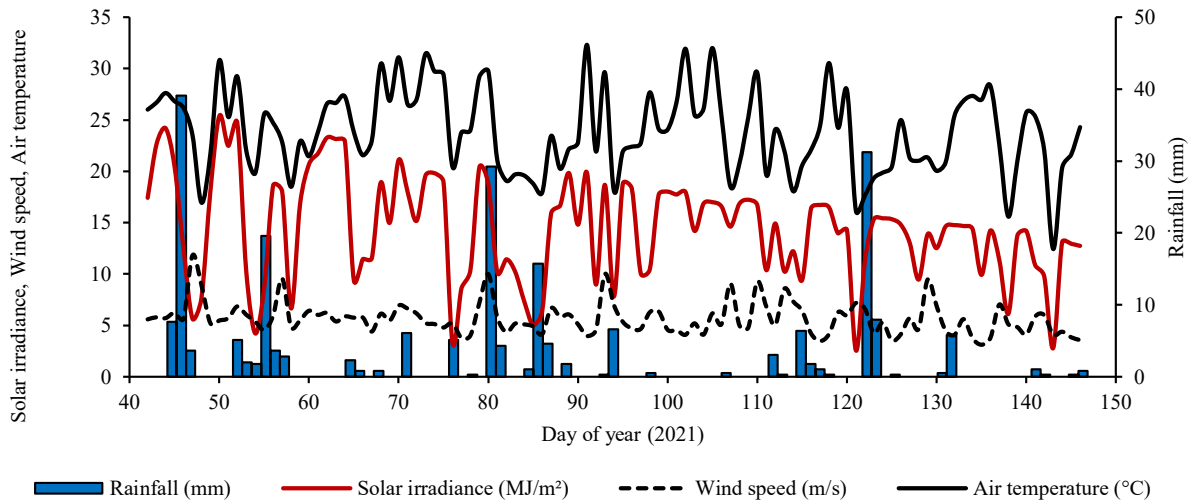


Figure 1: Swayimane weather conditions over the period of maize phenotyping

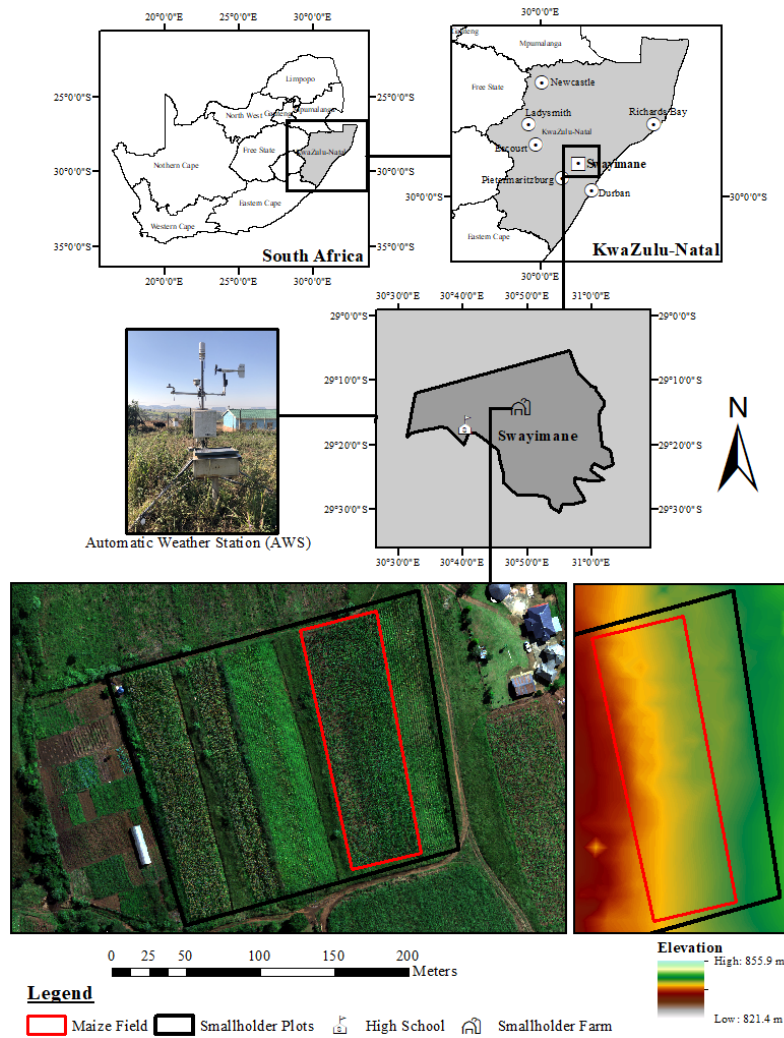





Figure 2: Location of the Swayimane study area, study site, and smallholder maize field.

2.2.2. Maize phenotyping





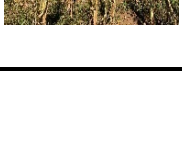
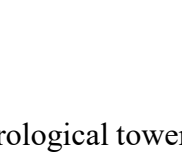
Maize seedlings were sown on the 8th of February 2021 and harvested on the 26th of May 2021 (Table 1), having a total growth cycle of 108 days. Chlorophyll was examined at different growth stages of the maize phenological cycle. Maize growth is divided into vegetative stages (which range from emergence to tasseling based on the number of fully expanded leaves) and reproductive stages (which range from silking to physiological maturity based on kernel development) (Cakir, 2004; Zhao et al., 2012). Within the various stages, certain transitions are important for monitoring and informing smallholder farmers. These are crop vegetative emergence (date of onset of photosynthetic activity, termed VE), tasseling (date when maximum leaf area is recorded and maize tassels emerge, termed VT), the beginning of senescence (date when green leaves visibly begin to become brown toned) (Du Plessis, 2003).

It is worth mentioning that during the mid-vegetative stage, the western portion (lower elevation) of the field appeared unhealthy. This may have been due to the fact that this portion of the field was not weeded during the early vegetative growth stage with the rest of the field. However, the farmer applied herbicide during the mid-vegetative growth stage to remove grasses and weeds that were found between maize rows. Consequently, the herbicide impacted the health status of these crops and the maize suffered herbicide burn (see Appendix A, Figure 23 for images of this portion of the field).

Table 1: Maize growth stages and characteristics

Days after emergence	Growth stage	Description	Pictures
0	VE	Germination and emergence. Planting depth 5-8 cm.	
	V2		
21	V5	Plant population established. Growth point 20-25 mm below surface. Leaf sheath and blades. Tassel initiation.	
32	V8	Ear initiation and early cob development.	
38	V10		
44	V12	Tassel at growth point begins to develop rapidly. Active growth of lateral shoots and cob	

Vegetative Growth Stages

49	V14	Reproductive Growth Stages	development from the sixth to eighth node above surface. Brace root development.	
56	VT		Tasseling stage. Silks are developing. The demand for water and nutrients is high. All leaves present. Pollination 5-10 days.	
63	R1		Kernel development. Silking stage.	
70	R2 - R3		Grain filling. Nutrients are transported to cob. Sugars converted into starch.	
77				
84				
91	R3 - R4		Physiological maturity and drying of kernels. Starch in kernels. End of mass gain.	
98				
105				
112	R5 - R6		Ready for harvest. Optimal moisture and nutrients.	
119				
160	R+			

2.2.3. Field data collection, sampling, and survey

Field data collection was conducted throughout the maize phenological cycle. A meteorological tower (Figure 3a) was installed in the center of the maize field monitoring NDVI through spectral reflectance sensors (SRS) (SRS sensors, Decagon Inc, Pullman, WA, USA). The SRS-NDVI sensors consist of a downward-facing and an upward-facing sensor. The upward-facing hemispherical sensor provided reference values of the sky radiance which normalized the downward-facing sensor values of maize foliar canopy irradiance. The SRS-NDVI measured wavelengths of 630 nm (red) and 800 nm (NIR) on a continuous basis at 10-minute intervals and 30-minute intervals (EM50G, Decagon, Pullman, WA, USA). To calculate upward reflected NDVI, the two-band radiometer measurements of incident radiation, within a 36° field of view (FOV), were used to measure the maize canopy reflected radiation (Figure 3b). The SRS data was calibrated using the information from the incident red and NIR radiation collected by the hemispherical SRS, and used to calculate a calibration constant α :

$$\alpha = Ir/In \quad (1)$$

where, Ir is the incident red radiation (630 nm) from above and In the incident NIR radiation (800 nm) from above, both obtained from the hemispherical sensor. Calibration of the values recorded by the Decagon sensors was then calculated:

$$\text{SRS NDVI} = \frac{\alpha Rn - Rr}{\alpha Rn + Rr} \quad (2)$$

where, Rn is the reflected NIR radiation and Rr the reflected red radiation (Anderson et al., 2016).

The data collected was downloaded from the datalogger to a laptop computer (ECH2O Utility, Decagon, Pullman, WA, USA) (Figure 3c). The SRS-NDVI data was used to monitor maize NDVI values through phenotyping. Importantly, the SRS-NDVI measurements of maize were used in conjunction with the multispectral UAV-derived NDVI imagery to assess the accuracy and reliability of the UAV-derived data. Since the SRS-NDVI sensor measures the NDVI of maize within its FOV, the average NDVI value of the same FOV was clipped and extracted from the multispectral UAV image. The SRS-NDVI measurements used for comparative correlation were taken at the same time as the UAV flight. Thus, environmental variance was assumed to be negligible.

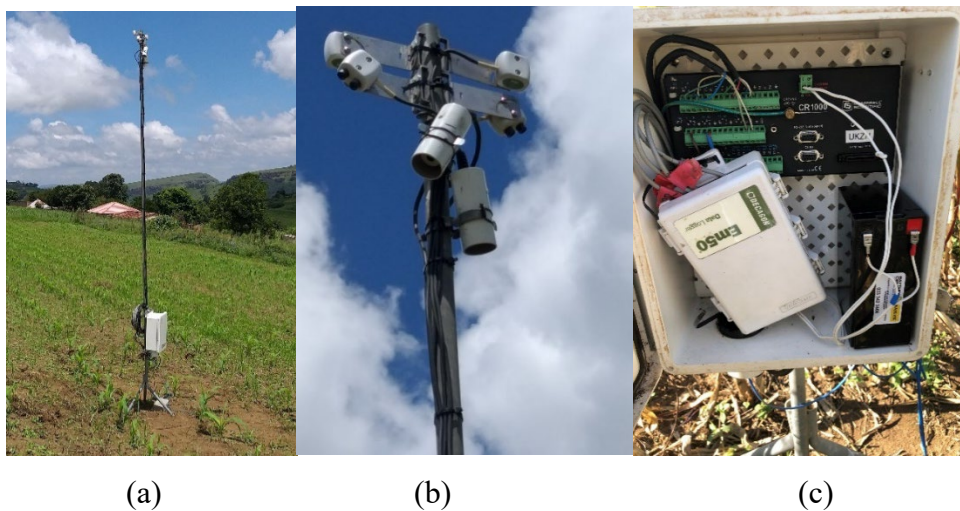


Figure 3: (a) Automated in-field meteorological tower in the maize field, (b) meteorological tower mounted with SRS-NDVI and SRS-PRI sensors held 4-meters above the ground, (c) CR1000 data logger, Em50 datalogger and 12 V battery.

In-field chlorophyll measurements of maize, at two-week intervals, were collected from the early vegetative (V5) growth stage to the late reproductive growth stages (R6). Pre-sampling of the maize smallholder field was conducted in Google Earth Pro where a polygon of the experimental field was digitized. The digitized polygon was then imported into ArcGIS 10.5 where it was used to generate sampling points. A total of 63 sample points were generated based on stratified random sampling within the digitised field boundary. These points were then uploaded onto a handheld Trimble Global Positioning System (GPS) with sub-meter accuracy. These locations were used to navigate to each sample point for field data collection. The maize plants at each sampling point were marked for consistent bi-weekly measurement.

A Konica Minolta soil plant analysis development (SPAD) 502 chlorophyll meter (Minolta corporation, Ltd., Osaka, Japan) was used to measure the chlorophyll content of maize leaves. SPAD meter readings are portable, non-destructive measurements of the of red (650 nm) and infrared (940 nm) radiation leaf transmittance. The device instantly calculates a unitless SPAD value that is proportional to the chlorophyll concentration within the sample leaf (Sibanda et al., 2020; Uddling et al., 2007). Field measurements were conducted between 10:00 am to 2:00 pm, corresponding with the optimal period of the day for crop photosynthetic activity. During the early growth stages (where a six leaf was present), the SPAD readings were measured on the newest fully expanded leaf with an exposed collar. Subsequent to tasseling, the ear leaf (i.e., the leaf attached to the same node as the primary ear shank) was measured (Costa et al., 2003). Readings were taken on one leaf per plant. The different locations of leaf measurement included: (a) the midpoint of each leaf blade, next to the main leaf vein, (b) approximately $1/3$ down from the leaf tip, and (c) approximately $1/3$ of the way down from the leaf tip. The three measurements were averaged per leaf and subsequently recorded. When conducting the chlorophyll readings, the SPAD meter was shielded from direct sunlight. SPAD meter measurements were conducted simultaneously with UAV image acquisition. SPAD measurements were converted into chlorophyll content values using the equation derived by Markwell et al. (1995) that achieved an $R^2 = 0.94$:

$$Chl = 110^{S^{0.0265}}$$

Where Chl represents the total chlorophyll per unit leaf area in $\mu\text{mol m}^{-2}$ and the S is the unitless SPAD value (Ling et al., 2011). The chlorophyll data was then added to the 63-sampling points map in a geographical information system (GIS). The point map was overlaid with the multispectral UAV image of the derived spectral reflectance values from each sampling point.

2.2.4. UAV multispectral-thermal camera and platform

The DJI Matrice 300 (DJI M-300) platform mounted with a MicaSense Altum camera and Downwelling Light Sensor 2 (DLS-2) was used to conduct aerial-based flights over the smallholder farms. The rotary-wing DJI M-300 series has vertical take-off and landing (VTOL) technology, making it well suited for small-scale agricultural crop imaging (Figure 4a). The DJI M-300 platform novelties include its 15 km transmission range, 7000 m maximum altitude, obstacle avoidance,

flightpath planning and locational position tracker. The maximum flight time of the M-300 is 55 minutes (without payload) and can reach a maximum speed of 27 m/s, which surpasses most drone platforms on the market. Moreover, the MicaSense Altum camera is a multispectral and thermal imaging sensor that integrates five spectral high-resolution narrow bands (blue, green, red, red-edge, and near-infrared) with a radiometric longwave infrared thermal camera (Figure 4b). The high-performance camera offers synchronized multispectral and thermal image capture and uses a global shutter that provides a one second capture rate for precise and aligned imagery (Hutton et al., 2020). The multispectral bands have a sensor resolution of 2064×1544 at 120 m (3.2 megapixels per multispectral band) and a ground sample distance (GSD) of 5.2 cm per pixel at a height of 120 m, suggesting the optimum flight altitude above the crop to receive high resolution images (Table 2). The camera also has a $48^\circ \times 37^\circ$ FOV, with an 8 mm focal length.

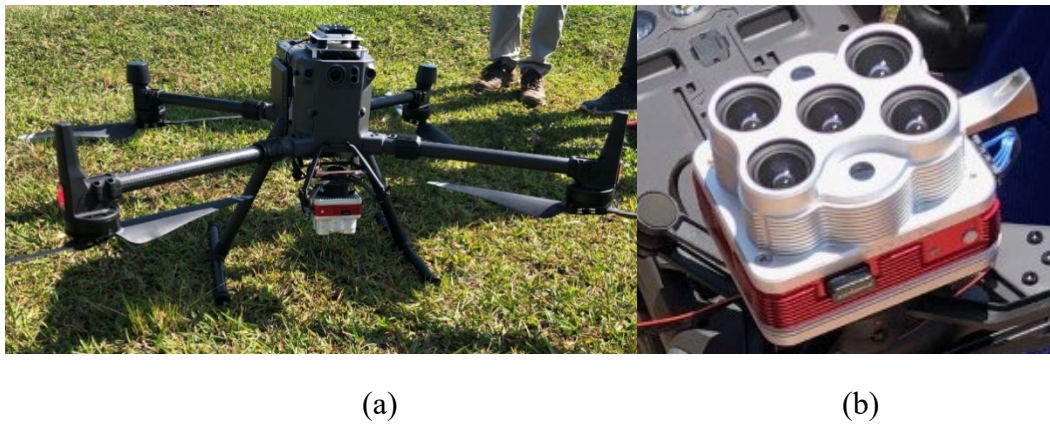


Figure 4: (a) DJI Matrice 300 platform and, (b) MicaSense Altum multispectral-thermal camera

Table 2: MicaSense Altum camera specifications

Band	Spectral colour	Band center/range	Ground sampling distance at flying height of 120 m
1	Blue	475 nm	5.2 cm per pixel
2	Green	560 nm	5.2 cm per pixel
3	Red	668 nm	5.2 cm per pixel
4	Red-edge	717 nm	5.2 cm per pixel
5	Near-infrared	842 nm	5.2 cm per pixel
6	Thermal infrared	8000 nm – 14 000 nm	81 cm per pixel

Source : (<https://micasense.com/altum/>)

2.2.5. Image acquisition and processing

A shapefile of the maize field was digitized in Google Earth Pro and imported into the DJI M-300 smart console, where it was used to design a flight plan covering the study area (Figure 5a). The flight plan enabled a hands-free drone flight mission over the study field and adjacent areas. Before and after the flight, the UAV was calibrated using the MicaSense Altum calibrated reflectance panel (CRP). This included the user manually taking an unshaded image directly over the CRP to discern the lighting conditions of the specific flight date, time, and location (Figure 5b). UAV flights were conducted every 2-weeks on selected days with clear sky conditions. UAV flights were conducted between 10:00 am and 12:00 pm as this is the time of optimal solar irradiance. This period also coincided with chlorophyll content measurements. Detailed flight conditions are presented in Table 3.

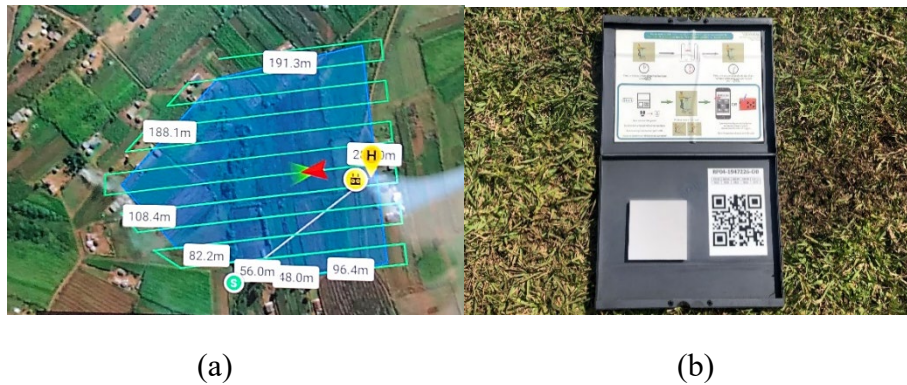


Figure 5: (a) DJI M-300 flight plan, (b) MicaSense Altum calibration reflectance panel

Table 3: UAV flight specifications

Parameters	Specifications
Altitude	100 meters
Ground sampling distance	7 cm
Speed	16 m/s
Flight duration	14 minutes 36 seconds
Composite images	321
Image overlap	80 %

A total of 3576 images were stitched together and radiometrically corrected (Pix4Dfields 1.8.0, Pix4d Inc., San Francisco, CA, USA). Radiometric correction was conducted in Pix4Dfields using all the captured images, including the before and after flight CRP images. The radiometric calibration target (the CRP) is a white balance card that provided the reflectance properties of the card across the

electromagnetic spectrum wavelengths of the camera. This enabled the software to calibrate and correct the reflectance of the images accordingly in line with the prevalent atmospheric conditions during the image acquisition. The CRP also had an absolute reference, which obtained the absolute reflectance values and made it possible to compare data from several flights. Once processed, a final orthomosaic and a digital elevation model (DEM) GeoTIFF image was generated. The orthomosaic was georeferenced in ArcGIS 10.5 with the use of ground reference points from Google Earth Pro. Images were referenced to the Universal Transverse Mercator (UTM zone 36S) projection.

The maize reflectance data was extracted from the multispectral Altum image. This was done by overlaying the ground-truthed maize chlorophyll measurements and their GPS coordinates in the form of a point map with the UAV multispectral image. The reflectance values were extracted for each coordinate, and for each UAV spectral band. The image was then used to compute vegetation indices (VIs) detailed in Table 4. VIs selected included various combinations of the multispectral bands that were specific to vegetation health and chlorophyll, such as the NDVI, the canopy chlorophyll content index (CCCI) and the red-edge chlorophyll index ($CI_{rededge}$). These vegetation indices were derived due to their performance in research literature (Haghighian et al., 2020; Naito et al., 2017; Xue and Su, 2017; Zhang and Zhou, 2015).

Table 4: Spectral UAV-derived vegetation indices used to predict chlorophyll content

Vegetation index	Abbreviation	Equation	Reference
Normalized difference vegetation index	NDVI	$(NIR - RED)/(NIR + RED)$	Xue and Su (2017)
Green normalized difference vegetation index	GNDVI	$\frac{NIR - GREEN}{NIR + GREEN}$	Naito et al. (2017)
Red-green ratio index	RGR	$\frac{RED}{GREEN}$	Qiu et al. (2020)
Normalized difference red-edge index	NDRE	$\frac{NIR - RED\ EDGE}{NIR + RED\ EDGE}$	Fitzgerald et al. (2010)
Corrected transformed vegetation index	CTVI	$\frac{NDVI + 0.5}{NDVI + 0.5} * (\sqrt{NDVI + 0.5})$	Naito et al. (2017)
Infrared percentage vegetation index	IPVI	$\left(\frac{NIR}{\frac{NIR}{2} + RED}\right) * (NDVI + 1)$	Haghighian et al. (2020)

Soil adjusted vegetation index	SAVI	$\left(\frac{\text{NIR} - \text{RED}}{\text{NIR} + \text{RED} + L} \right) * (1 + L)$	Xue and Su (2017)
L is a constant between 0 and 1.			
Optimized soil adjusted vegetation index	OSAVI	$\frac{\text{NIR} - \text{RED}}{\text{NIR} + \text{RED} + 0.16}$	Xue and Su (2017)
Green chlorophyll index	CI _{green}	$(\text{NIR}/\text{GREEN}) - 1$	Zhang and Zhou (2015)
Red-edge chlorophyll index	CI _{rededge}	$(\text{NIR} - \text{RED EDGE}) - 1$	Zhang and Zhou (2015)
Canopy chlorophyll content index	CCCI	$\frac{\text{NIR} - \text{RED EDGE}}{\text{NIR} + \text{RED EDGE}} / \frac{\text{NIR} - \text{RED}}{\text{NIR} + \text{RED}}$	Fitzgerald et al. (2010)
Chlorophyll vegetation index	CVI	$\text{NIR} * \left(\frac{\text{RED}}{\text{GREEN}^2} \right)$	Vincini and Frazzi (2011)
Modified chlorophyll absorption ratio index	MCARI	$\frac{1.5[2.5(\text{NIR} - \text{RED}) - 1.3(\text{NIR} - \text{RED})]}{\sqrt{[(2\text{NIR} + 1)^2 - (6\text{NIR} - 5\sqrt{(\text{RED})})]}}$	Wu et al. (2008)

2.2.6. Statistical analysis

The random forest algorithm was used to predict maize chlorophyll content since it is renowned for its simplicity, robust nature, and ability to perform well regardless of sample size (Dye et al., 2011; Luan et al., 2020). The random forest ensemble is a machine learning algorithm that uses bootstrap aggregation to construct multiple trees on a subset of samples derived from the training data (Abdel-Rahman et al., 2013). Decision trees are grown to their maximum capacity with a randomised subset of predictors (UAV-derived spectral data), and each node is split using random subsets of input variables (Adam et al., 2012). Furthermore, the random forest regression has the ability to identify predictor variables that are influential in the prediction model based on the sum of the reduction in Gini impurity across the nodes of the feature (Sibanda et al., 2021).

Specifically, the RGtk2 and rattle packages in RStudio software version 1.4.1564 were used to develop the random forest regression model through numerical inputs. The outputs of the random forest model were optimised using variable importance as they determine the most influential bands and VIs in prediction. Variables of low importance were removed throughout the analysis and the random forest model was continuously modified for optimal prediction. The process of variable selection reduces issues of variable redundancy and multicollinearity, which affect the performance of the regression

model. The model was user-defined and fine-tuned to an optimal 500 trees and 8 variables. These hyper-parameters were attained after numerous iterations. The map outputs of the random forest regression models are formulated using the linear equations from each of the regression graphs, therefore, accuracies of the graphs are the same as accuracies of the maps.

2.2.7. Accuracy assessment

Accuracy assessments were performed to evaluate the predicted chlorophyll regression models. The accuracy metrics used were the coefficient of determination (R^2), root-mean-squared error (RMSE), and the relative root-mean-squared error (RRMSE). The R^2 measured the variation between the measured and predicted: foliar temperature and stomatal conductance. The RMSE assessed the magnitude of error between the field measurements and modelled outputs of foliar temperature and stomatal conductance. While the RRMSE evaluated the accuracy of the model and was used to compare the performance of regression models across maize phenotyping. The RRMSE is calculated by normalising the mean of each variable RMSE value and expressed as a percentage, where lower percentages are considered more accurate (Taghizadeh-Mehrjardi et al., 2020).

2.3. Results

2.3.1. Descriptive analysis of UAV-derived data and ground-based maize data

2.3.1.1. Maize SRS-NDVI growth cycle data

The automated time series of daily SRS-NDVI data over the phenological cycle was generally a smooth curve with some fluctuations during the various vegetative growth stages, and a significant decline in NDVI values after an unanticipated hailstorm (Figure 6). NDVI values increased rapidly from 0.1 in the early vegetative growth stages (DOY 42) to a peak of approximately 0.7 in the early reproductive development stages (DOY 102). Thereafter, a strong decline in NDVI was observed from the early reproductive growth stage (DOY 102) to the mid-reproductive growth stage (DOY 118), declining from an NDVI of 0.7 to 0.5, respectively. During the transition from the early to mid-reproductive stages, a hailstorm damaged the crop and resulted in a slight NDVI increase the day after the weather occurrence which, was subsequently followed by a rapid decrease in NDVI values for the following days. Subsequently, the NDVI during the late reproductive growth stages fluctuated between 0.5 and 0.6. The SRS-NDVI data shows that there were significant changes throughout the growth

cycle of the maize crop, with increases corresponding to the time when rapid vegetative growth occurred and decreases corresponding to mid- to late maize productivity.

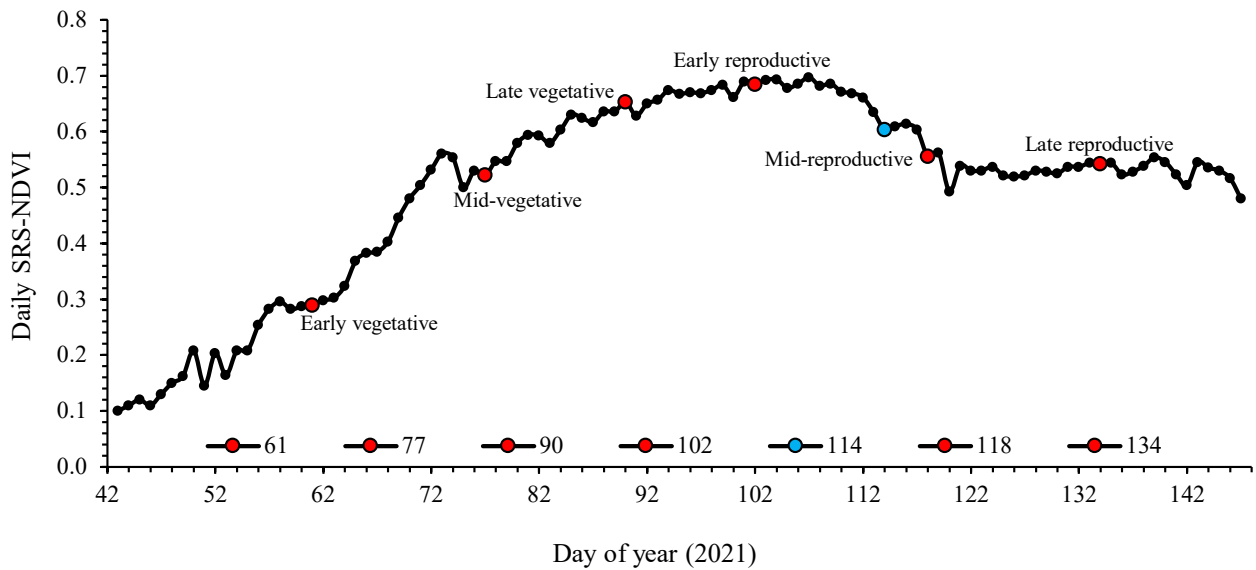


Figure 6: Daily SRS-NDVI values of maize throughout the phenological cycle. Red points indicate the days of field visits to collect field data. Blue point indicates day of crop disturbance due to a hailstorm.

2.3.1.2. Evaluation of UAV-derived data against ground-based NDVI and chlorophyll data

The relationship between the ground-based SRS-NDVI data and the UAV-derived NDVI data for the various maize growth stages was found to be linear (Figure 7a). There was a strong positive correlation between the SRS-NDVI and UAV-derived NDVI ($R^2 = 0.98$; $p = 0.001$). At low NDVI values such as 0.30, the UAV-derived NDVI was higher than the SRS-NDVI. At mid-range NDVI values, i.e., 0.50, the UAV-derived NDVI and SRS-NDVI were almost identical. At higher NDVI values, such as 0.70, the SRS-NDVI was higher than the UAV-derived NDVI. Similarly, the average chlorophyll content measurements for each trip were compared against the UAV-derived NDVI data to better understand the relationship of NDVI with maize chlorophyll concentration. Figure 7b illustrates that SRS-NDVI values correlate well with a chlorophyll content values, attaining an $R^2 = 0.78$. High UAV-derived NDVI values generally corresponded with high chlorophyll concentrations.

Specifically, the early maize growth stages yielded low NDVI values of approximately 0.30 – 0.45 for day of year (DOY) 61. Similarly, the low NDVI value correlated with a low chlorophyll concentration of $74.5 \mu\text{mol m}^{-2}$ on DOY 61. However, as the maize developed, the measured and UAV-derived

NDVI values progressively increased to 0.54 on DOY 77, followed by 0.65 on DOY 90 and 0.67 on DOY 102. Likewise, maize chlorophyll concentrations increased to 461 $\mu\text{mol m}^{-2}$ on DOY 77, followed by 573.6 $\mu\text{mol m}^{-2}$ on DOY 90, and 651.8 $\mu\text{mol m}^{-2}$ on DOY 102. Thereafter, the measured and UAV-derived NDVI values in the mid and late reproductive stages decrease to 0.55 – 0.57 on DOY 118 and 0.49 – 0.54 on DOY 134, respectively. Similarly, the measured chlorophyll concentrations in these stages decreased to 331.4 $\mu\text{mol m}^{-2}$ on DOY 118 and 183.5 $\mu\text{mol m}^{-2}$ on DOY 134.

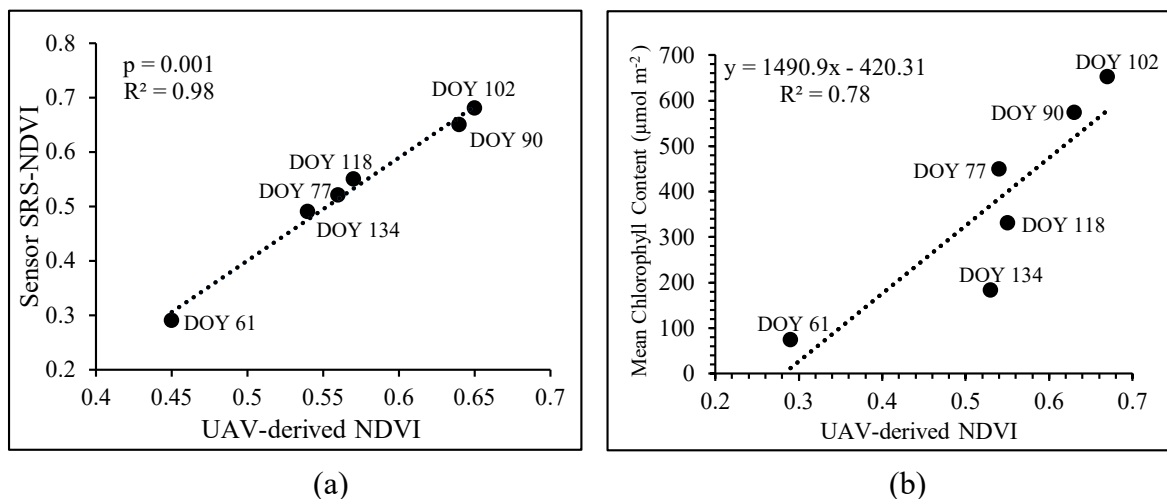


Figure 7: Correlation of (a) in-field sensor SRS-NDVI and UAV-derived NDVI (b) measured maize chlorophyll content and UAV-derived NDVI across the maize growth stages

2.3.2. Descriptive statistics of chlorophyll content from SPAD

The lowest chlorophyll concentration was attained during the early vegetative growth stage (V5 – V10) at 13.5 $\mu\text{mol m}^{-2}$ (Table 5). The highest chlorophyll concentration was recorded during the early reproductive stage (R1 – R3) at 3765.4 $\mu\text{mol m}^{-2}$. On average, the maize chlorophyll ranged from 58.85 $\mu\text{mol m}^{-2}$ to 2043.5 $\mu\text{mol m}^{-2}$. The average and median of maize chlorophyll, across the growth stages were 362.9 $\mu\text{mol m}^{-2}$ and 259 $\mu\text{mol m}^{-2}$, respectively. The average standard deviation of chlorophyll values was 342.6, which indicated a large deviation of the measurements from the mean value of 362.9.

Table 5: Descriptive statistics of maize chlorophyll content throughout the various growth stages

Day of year (DOY)	Chlorophyll content at various growth stages	Minimum ($\mu\text{mol m}^{-2}$)	Maximum ($\mu\text{mol m}^{-2}$)	Mean ($\mu\text{mol m}^{-2}$)	Median ($\mu\text{mol m}^{-2}$)	Standard deviation
61	V5 – V10	13.51	255.5	74.5	60.2	54.2
77	V12	61.7	3242.6	461	331.8	466.7
90	V14 – VT	130.4	2792.4	573.6	390.2	497.7
102	R1 – R2	104.2	3765.4	651.8	476.2	641.8
118	R2 – R4	26.8	1555	331.4	234.1	301.8
134	R4 – R5	16.5	650.2	183.5	61.7	93.6
Average value		58.85	2043.5	362.6	259	342.6

2.3.3. Random forest models of maize chlorophyll content

2.3.3.1. Optimized regression models of maize chlorophyll content over the various growth stages

The relationship of measured (SPAD derived) and modelled (UAV derived) chlorophyll content varied across the various maize growth stages. The model was able to optimally estimate the chlorophyll content throughout the various growth stages; however, the prediction of chlorophyll proved more accurate during the vegetative growth stages. During the early vegetative growth stage (V5 – V10) the highest RMSE accuracy for the growth cycle achieved was $13.9 \mu\text{mol m}^{-2}$, with an $R^2 = 0.80$ and $\text{RRMSE} = 11 \%$ (Figure 8a). The mid-vegetative growth stage (V12) $\text{RMSE} = 78.2 \mu\text{mol m}^{-2}$, $R^2 = 0.79$ and $\text{RRMSE} = 14 \%$ (Figure 8b). Whereas the late vegetative growth stage (V14 – VT) produced the lowest $\text{RMSE} = 96.2 \mu\text{mol m}^{-2}$, $R^2 = 0.85$ but obtained a RRMSE model accuracy of 8% (Figure 8c). Similarly, the early reproductive development stage (R1 – R2) obtained a low $\text{RMSE} = 87.4 \mu\text{mol m}^{-2}$, $R^2 = 0.89$ but produced the highest RRMSE accuracy of 7% (Figure 8d). The RMSE accuracies increased to $76.2 \mu\text{mol m}^{-2}$ and $31.3 \mu\text{mol m}^{-2}$ during the mid-reproductive (R2 – R4) and late reproductive (R4 – R5) growth stages, respectively. However, the model produced the lowest RRMSE and R^2 accuracies during the R2 – R4 and R4 – R5 stages at a RRMSE of 28% , $R^2 = 0.75$ (Figure 8e) and a RRMSE of 25% , $R^2 = 0.78$ (Figure 8f), respectively.

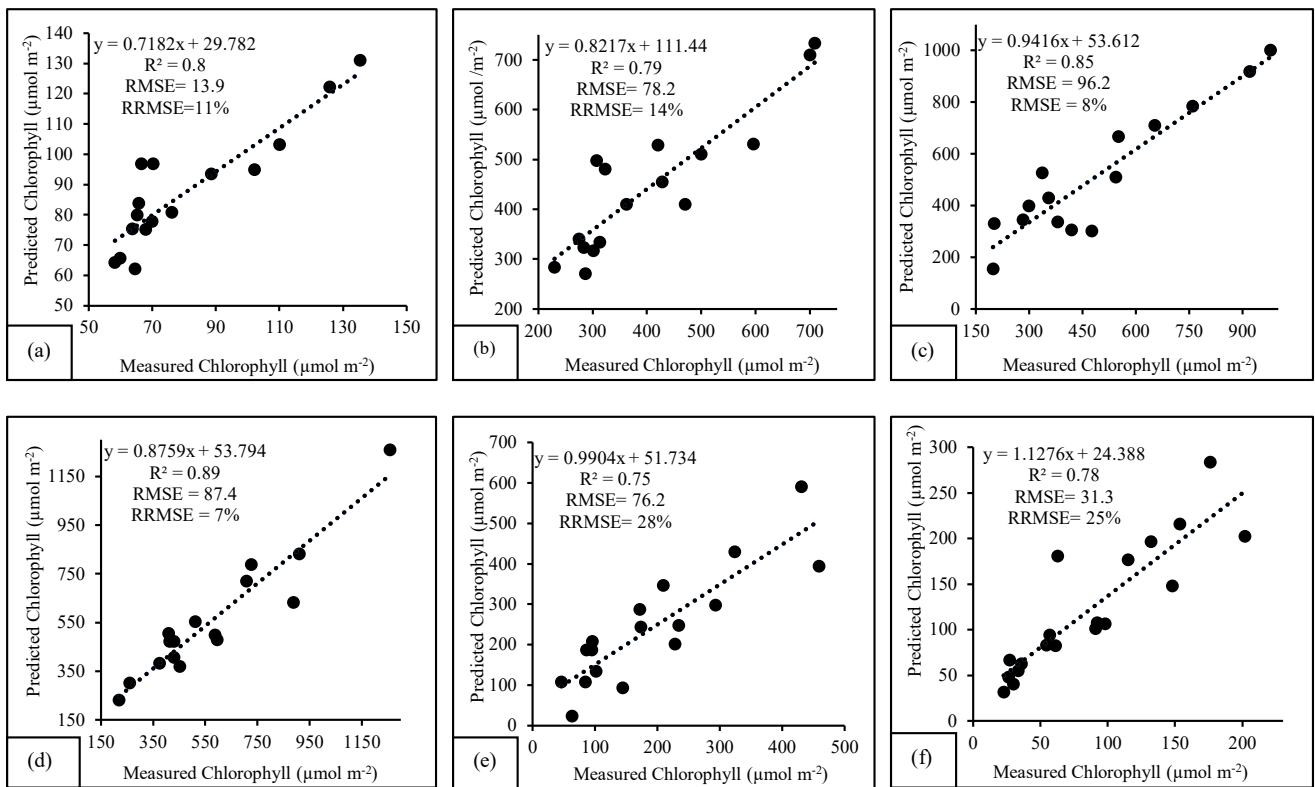


Figure 8: Linear relationships between measured and predicted maize chlorophyll content for vegetative stages (a) V5 – V10, (b) V12, (c) V14 to VT, and reproductive stages (d) R1 – R3, (e) R3 – R4, (f) R5 – R6.

2.3.3.2. Variable importance of maize chlorophyll content models over the various growth stages

The early reproductive (R1 – R3) growth stage produced the most optimal model performance in general, with a RRMSE = 7 % and $R^2 = 0.85$. The top VIs and spectral bands selected by the model for the early reproductive growth stage were the NDRE, NIR band, $CI_{rededge}$ and the NDVI (Figure 9d). The late vegetative (V14 – VT) growth stage also yielded a high model RRMSE = 8 % and $R^2 = 0.89$ based on the NIR band, CCCI, red-edge band and NDVI amongst others, in order of importance (Figure 9c). The aforementioned variables of importance for the R1 – R3 and V14 – VT stages were major contributors in modeling chlorophyll content, as there was a major step down in importance of the other VIs and bands. Similarly, the mid-vegetative (V12) and mid-reproductive (R4 – R5) have major stand out importance variables of CCCI, red-edge, green, NIR and NDVI, NIR, red-edge and $CI_{rededge}$ amongst others, respectively. On the other hand, the early vegetative (V5 – V10) and late reproductive (R5 – R6) stages have a gradual decrease in variable importance scores based on the

CI_{rededge}, NDVI, NDRE, NIR and red-edge, NIR, MCARI, OSAVI amongst others, respectively. In general, the variables obtaining the highest importance scores were derived from the NIR, red-edge and red wavebands.

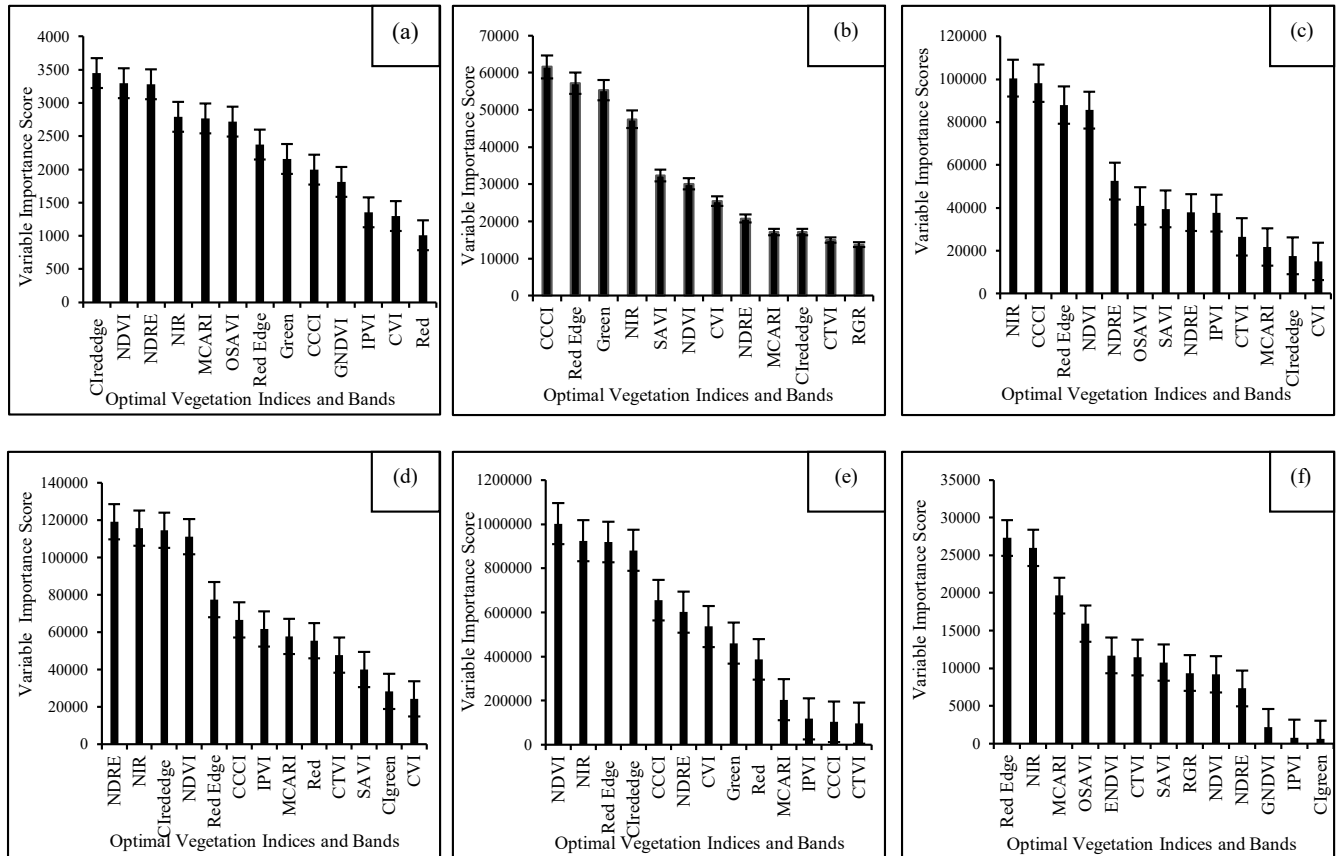


Figure 9: Variable importance scores of optimal chlorophyll content VIs and bands for vegetative stages (a) V5 – V10, (b) V12, (c) V14 to VT, and reproductive stages (d) R1 – R3, (e) R3 – R4, (f) R5 – R6

2.4.3.3. Mapping the spatial distribution of maize chlorophyll content over the various growth stages

The modelled chlorophyll concentrations ranged from 33 $\mu\text{mol m}^{-2}$ to 126 $\mu\text{mol m}^{-2}$ (Figure 10). The chlorophyll content of maize was low during the early vegetative growth stages (V5 – V10), and then progressively increased throughout the various growth stages. In the late vegetative (V14 – VT), early reproductive (R1 – R3), and mid-reproductive (R4 – R5) growth stages the chlorophyll concentrations were the highest. Subsequently, chlorophyll content was depleted during the late reproductive stage (R5 – R6).

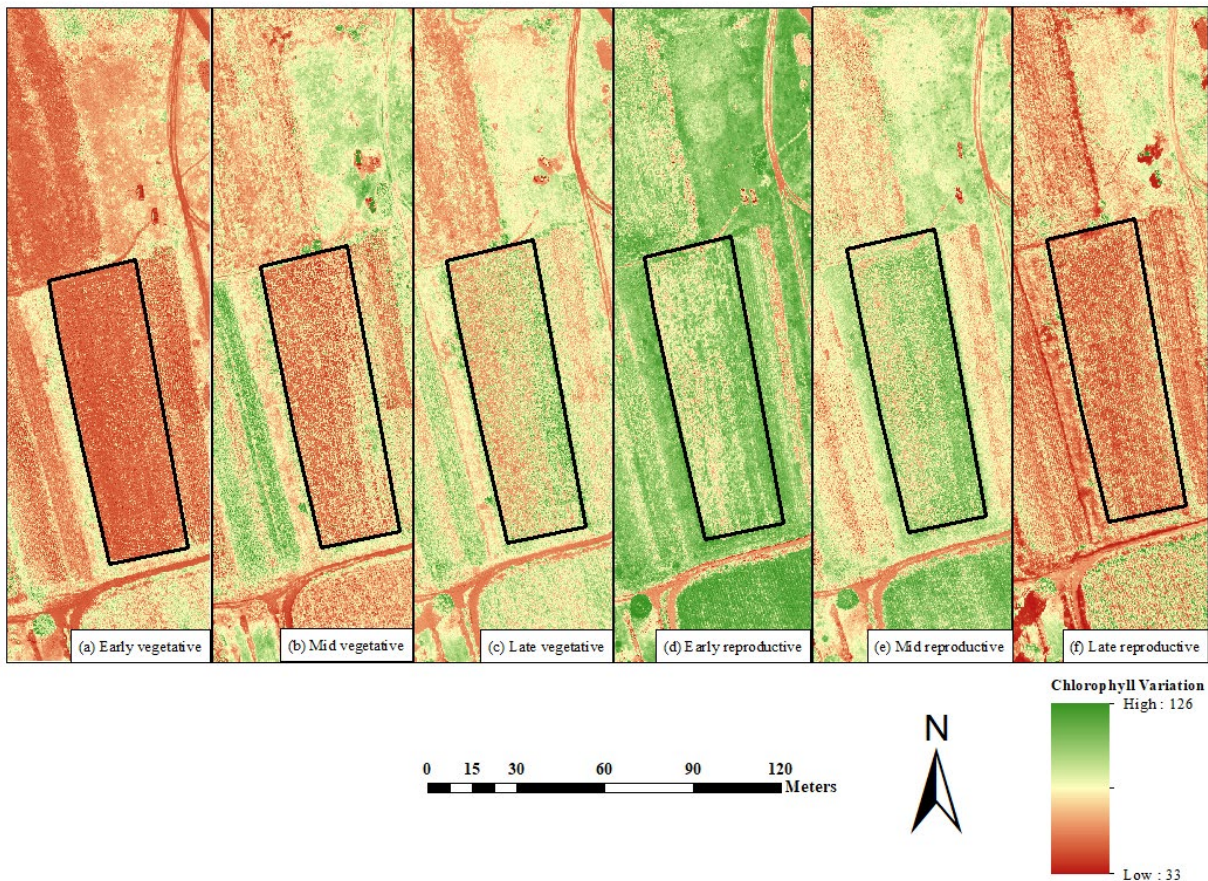


Figure 10: Spatial distribution of chlorophyll content over the maize field for vegetative stages (a) V5 – V10, (b) V12, (c) V14 to VT, and reproductive stages (d) R1 – R3, (e) R3 – R4, (f) R5 – R6.

2.4. Discussion

The aim of this study was to predict chlorophyll content variations across maize phenological stages, using UAV-derived VIs and the random forest algorithm. In doing so, the study attempted to determine the optimal maize growth stage(s) for chlorophyll prediction. It is evident that chlorophyll concentrations varied over the phenological stages, and the model was able to discern the optimal chlorophyll growth stages. The chlorophyll variations of maize over the growing season are useful for the estimation of the health and productivity status of the smallholder field.

2.4.1. Estimating maize chlorophyll content across the growing season

The findings of the study model performed well throughout the vegetative growth stages and showed that the earliest vegetative growth stage yielded the highest RMSE accuracy of $13.9 \mu\text{mol m}^{-2}$, $R^2 =$

0.80 (RRMSE = 11 %) based on the CI_{rededge} , NDVI, NDRE, NIR as the most influential variables (in order of importance). Specifically, the red-edge and NIR regions were detected as crucial wavelengths in the model's prediction of chlorophyll content, due to their association with healthier plants. This is because the red-edge wavelength is sensitive to plants with high chlorophyll content, nitrogen content, and biomass, and thus are better predicted using the red-edge (Clevers and Gitelson, 2013; Delegido et al., 2011; Sibanda et al., 2020). Additionally, the NIR region strongly influences the prediction of chlorophyll content, as it is sensitive to the high foliar reflectance induced by the pigment concentrations of plant canopy structures (Broge and Leblanc, 2001; Sankaran et al., 2013). The studies of Sibanda et al. (2020) and Singhal et al. (2019) demonstrated a similar association between the red-edge and NIR regions with chlorophyll content by achieving an R^2 of 0.91 and 0.90, respectively. In this study, accurate chlorophyll concentrations were associated with crop emergence and development, as the leaf area index was low, resulting in more dynamic photosynthetic rates of the crop, which facilitates high reflectance in the red-edge and NIR sections. Nevertheless, during the early vegetative growth stage the chlorophyll content is measured low due to the high soil reflectance when there is a minimal maize canopy structure. Furthermore, red-edge and NIR derived VIs are notable regions that surpass the effects of atmospheric interferences, visible irradiance, variable background effects, and geometrical arrangement of a scene when compared to conventional bands (Curran et al., 1990; Goodbody et al., 2020). Thus, the red-edge and NIR wavelengths facilitated optimal maize chlorophyll prediction, as the low foliage density of the early vegetative growth stage did not saturate and cause spectral confusion of the sensor during image acquisition.

Meanwhile, high chlorophyll concentrations are also associated with the late vegetative and early reproductive growth stages, as maize reaches photosynthetic maturity and requires high productivity to begin fruit production (Rostami et al., 2008). Results from this study showed a similar trend, and the model prediction accuracies were most optimal during the late vegetative and early reproductive with a RRMSE accuracy of 8 % and 7 % and R^2 values of 0.85 and 0.89, respectively. Such results are attributed to the fact that the reflectance of maize leaf chlorophyll content during the late vegetative and early reproductive stages is stronger than at other stages of phenotyping, due to the high leaf area index and full canopy closure characterized by these stages (Walker et al., 2018; Walker and Schulze, 2006). It has been documented in studies by Walker et al. (2018), Dahms et al. (2016) and Costa et al. (2001) that during the stages of tasseling, silking and pollination, maize is characterised by a fully developed leaf canopy structure with a high leaf area index that promotes the detection of higher chlorophyll content. Hence, the dense canopy architecture and absence of soil background effect

created a homogenous scene of green pigment reflectance, which was optimal in the prediction of chlorophyll content over the smallholder field.

Similarly, to the early vegetative stages, the NIR and red-edge bands were significant variables in maize chlorophyll prediction, due to the favourable detection in high chlorophyll reflectance by these regions. The biochemical properties of a dense foliar canopy such as the thick waxy cuticle, air cavities, chloroplasts and mesophyll cell thickness all contribute to the high NIR and red-edge reflectance, which is directly correlated with chlorophyll content (Mutanga et al., 2012; Sibanda et al., 2021). Thus, the high chlorophyll concentrations associated with these stages in the study are also associated with a healthier crop, and further coincided with the SRS-NDVI values of approximately 0.65. In this regard, the high levels of chlorophyll content were favourable in model prediction, hence these stages being the most accurate in estimation.

During the mid-reproductive and late reproductive stages, the model prediction accuracies were lowest with an RRMSE of 28 % and 25 % and R^2 values of 0.75 and 0.78, respectively. The low model prediction accuracies could be attributed to the adverse effects of a hailstorm that damaged the maize canopy structure (see Appendix A, Figures 24 and 25 for images of maize crop hail damage), resulting in a lower crop chlorophyll content. The physical damage to the maize canopy exposed the underlying soil surface that consisted of damaged and decayed maize leaves. This resulted in spectral confusion due to the hybrid of soil and senescing leaf reflectance imaged by the MicaSense Altum camera, resulting in the failure of the model to discern the apparent chlorophyll variations. This is because the predominant brown tone of the senescing leaves and soil resulted in most bands and VIs being absorbed due to the low chlorophyll concentrations, whereas wavelengths such as the red band reflected much higher. Nevertheless, an apparent decline in NDVI values prior to the hailstorm was evident and associated with a decline in chlorophyll. This may be due to the fact that at this point in phenotyping, the crop channels its nutritional resources and energy towards fruit production (Walker et al., 2018), resulting in a reduction of chlorophyll concentration, which is also apparent in the results.

2.4.2. Implications of the study

Smallholder farmers are constantly striving to maximise their small-scale crop production and produce healthy and productive yields. However, they are seldom the focus of innovation and lack resources, as it is always assumed that their scale of operations does not necessitate such. Thus, such findings

demonstrate the use of precision agricultural technologies (i.e., UAVs), which can facilitate improved smallholder agricultural management. Specifically, UAV-derived data is captured in almost near real-time, which enables for quick and effective management that may improve crop health and productivity. Moreover, the quick turnaround time data is particularly useful when there are erratic weather conditions, such as the hailstorm occurrence. Such agrometeorological effects prove how South African smallholder farmers are subjected to the variability of weather and climate, which has consequences on crop growth, health, and the overall productivity of their farms. In such instances, UAV-derived data could be used to perform a rapid assessment of likely hail damage with a quick turnaround time, allowing farmers to make informed and effective decisions on agricultural management and provide advance warning for food insecurity. Therefore, the quick turnaround time of UAV technology is beneficial in smallholder agricultural systems as it allows for rapid and informed decisions to limit further crop health issues.

2.5. Conclusion

Smallholder farming systems tend to lack the required resources to maximise their productivity and monitor croplands for healthy growth and development. In recent years, the synergistic use of UAV remotely sensed technology and crop health proxies such as chlorophyll content have been used to facilitate a deeper understanding of crop dynamics. In this regard, the study tested the use of UAV-derived multispectral data through the estimation of maize chlorophyll content over the various stages of phenotyping. This was done through the use of a random forest prediction model, which estimated the chlorophyll concentrations of maize in smallholder farms in Swayimane. Therefore, premised on the findings of the study, it is concluded that:

- Optimal chlorophyll content prediction accuracies were produced during early vegetative growth stages (V5 – V10 and V12), late vegetative growth stages (V14 – VT) and early reproductive growth stages (R1 – R3),
- Maize chlorophyll content was optimally estimated through UAV derived NIR and red-edge wavelengths.

Since, chlorophyll content has been widely illustrated to be a proxy of crop health, the findings of the study imply that UAV-derived data could be optimally utilised to characterise the general state of maize health in smallholder cropping lands, with significantly improved spatial accuracies. Such precision technology advancements are a low-cost, objective, and accurate technique that smallholder

farmers can adapt to inform decision-making and agricultural management. Specifically, multispectral UAV technology is spatially explicit and provides almost near real-time data for understanding crop health through the biochemical indicator of chlorophyll. This technology potentially overcomes some of the limitations associated with satellite imagery, however the study could have benefited from higher spectral resolution data and additional testing data to improve the model performance. Nevertheless, the random forest model performed relatively well at predicting the chlorophyll content in the smallholder farms. Therefore, multispectral UAV technology is a beneficial solution to smallholder agriculture as it provides farmers with information on crop dynamics at user-defined spatial and temporal scales for improved management and overall productivity.

Lead into Chapter 3

While previous studies on the assessment of maize in commercial farms of South Africa have displayed significant progress in terms of technological advances, rural smallholder farms lack such innovative and objective tools, and thus are subjected to crop issues. Such issues include unproductive crop growth and water stress throughout phenotyping. Chapter 2 provided an analysis on the maize health of a smallholder farm using the indicator of chlorophyll content, where a random forest regression model predicted the chlorophyll concentrations through the various phenological stages. Conclusions on the maize crop health of the smallholder farm were drawn using the prediction models and in-situ NDVI measurements, which illustrated how UAV-derived data can be a useful tool to inform smallholder farmers on improving management practices throughout phenology. Chapter 3 takes this further by assessing a frequent issue South African smallholder farmers face, being crop water stress. Specifically, maize crop water stress is determined using the indicators of foliar temperature and stomatal conductance, where random forest prediction models are run for each indicator throughout maize phenotyping. Additional in-situ measurements of temperature enhance the conclusions on maize crop water stress over the maize phenological cycle. This chapter also identifies the most optimal growth stages for the prediction of foliar temperature and stomatal conductance.

CHAPTER 3: ESTIMATION OF FOLIAR TEMPERATURE AND STOMATAL CONDUCTANCE VARIABILITY AS A PROXY FOR MAIZE WATER STRESS USING UNMANNED AERIAL VEHICLE BASED PHENOTYPING IN SMALLHOLDER FARMS (PAPER 2)

Abstract

Climatic variability and extreme weather phenomena impact agricultural production, especially in sub-Saharan smallholder cropping systems that are commonly rainfed. Hence, the development of early warning systems on moisture content can facilitate planning, mitigation of losses and optimization of yields through moisture augmentation. Precision agricultural practices facilitated by unmanned aerial vehicles (UAVs) with very high-resolution cameras are useful for monitoring farm scale dynamics at near real-time and have become an important agricultural management tool. Considering these developments, the utility of multispectral and thermal infrared UAV imagery was evaluated in combination with a random forest machine learning algorithm to estimate the maize foliar temperature and stomatal conductance as indicators of potential crop water stress and moisture content over the entire phenological cycle. The results illustrated that the thermal infrared waveband was the most influential variable during the vegetative growth stages, whereas the red-edge and near-infrared derived vegetation indices, were fundamental during the reproductive growth stages, for both temperature and stomatal conductance. The results also suggested mild water stress during vegetative growth stages and after a hailstorm that occurred during the mid-reproductive stage. Furthermore, the random forest model optimally estimated the maize crop temperature and stomatal conductance over the various phenological stages. Specifically, maize foliar temperature was best predicted during the mid-vegetative growth stage and stomatal conductance during the early reproductive growth stage. Resultant maps of the modelled maize growth stages captured the spatial heterogeneity of maize foliar temperature and stomatal conductance within the maize field. Overall, the findings of the study demonstrated that the use of UAV multispectral and thermal imagery in concert with prediction-based machine learning is a useful tool available to smallholder farmers for informed management decisions that include optimal implementation of irrigation schedules.

Keywords: drones, machine learning, maize monitoring, precision agriculture

3.1. Introduction

In recent decades, agricultural production in sub-Saharan Africa has been threatened by water scarcity, unpredictable weather, and arid conditions (Lickley and Solomon, 2018; Nhamo et al., 2019). In South Africa, smallholder agriculture (less than two hectares in size) is predominantly rainfed, which often results in crops experiencing water stress and moisture shortages due to inadequate rainfall (Adisa et al., 2018; Rockstrom, 2000; Ubisi et al., 2017). However, there are limited spatially explicit evidence-based frameworks and instruments for monitoring crop water stress in smallholder croplands, especially in those cultivating maize (*Zea mays L.*) predominantly for subsistence (Andersson et al., 2009; Lu et al., 2017). Since maize is a staple grain crop and one of the most widely cultivated crops on South African smallholder farms (Walker and Schulze, 2006), there is a need for spatially explicit methods to characterise maize water stress to prevent yield losses and optimise the productivity of smallholder farmers.

Maize requires between 450 to 600 mm of water per season as it is sensitive to water stress, especially during the tasseling, silking, and pollination stages (Taghvaeian et al., 2014). At physiological maturity, a single maize crop requires approximately 250 litres of water to produce approximately 15 kilograms of grain for each millimeter of water consumed (Du Plessis, 2003). Although, additional factors like soil nutrients, light and humidity may affect growth, water stress is often the major limiting factor. The high variability of rainfall in South Africa often results in less water available to sustain optimal crop growth and productivity (Carroll et al., 2017; Haarhoff et al., 2020). These water deficits result in stomatal closure to reduce moisture loss through transpiration, resulting in increased leaf temperatures due to limited moisture conductance to cool the leaf surface (Saseendran et al., 2015; Zhang and Zhou, 2019). Hence, the determination of foliar temperature and stomatal conductance are often used as proxies for an almost near real-time detection of crop water stress (Dai et al., 2004; Gerhards et al., 2019; González-Dugo et al., 2006; Jackson et al., 1981; Yun et al., 2020). Accurate quantification of maize foliar temperature and stomatal conductance across the growing season can therefore assist smallholder farmers in adopting measures to mitigate losses and optimise yield.

Traditionally, crop water stress has been determined using in-situ plant measurements, soil moisture content, or meteorological variables (González-Dugo et al., 2006). However, these approaches are time-consuming, costly, laborious, (Jackson et al., 1981), and in South Africa, prone to vandalism and theft, and thus not suitable for continuous and real-time monitoring of crop water stress. Recently,

studies have demonstrated that remote sensing techniques using multispectral or thermal imagery can be used to monitor crop water stress (Jamshidi et al., 2021; Sepulcre-Cantó et al., 2005; Veysi et al., 2017; Zhang et al., 2019a; Zhang et al., 2019b). According to El-Hendawy et al. (2019), several multispectral sections of the electromagnetic spectrum are indirect water stress indicators and are useful for quantifying crop water content through the leaf biochemical attributes (El-Hendawy et al., 2019). Specifically, the visible (blue, green, and red) and the near-infrared (NIR) wavelengths hold great potential for the prediction of water due to their absorption of water through leaf pigments such as chlorophyll (Pasqualotto et al., 2018). Moreover, the thermal infrared portion of the spectrum is directly correlated to water content proxies, such as temperature and stomatal activity, and is thus proficient in the analysis of temperature attributes. The thermal infrared radiation ranges from 8 μm to 14 μm on the electromagnetic spectrum, and its utility in remote sensing enables the detection of water stress due to its non-destructive and low labour inputs (Gerhards et al., 2019).

While traditional satellite-based remote sensing techniques have proven useful in quantifying water stress, several constraints limit their suitability for monitoring temperature and stomatal conductance at a farm-scale. The spatial resolution of satellite earth observation data is generally too coarse to capture the spatial heterogeneity within smallholder farms. Moreover, broad-band thermal satellite imagery results in geometrical inaccuracies when co-registering to other portions of the electromagnetic spectrum that have higher spatial resolutions (Prakash, 2000). Thus, alternate approaches that can adequately capture the spatial heterogeneity at localized levels are required to facilitate precision agricultural applications within smallholder farms.

In recent years, unmanned aerial vehicles (UAVs) have become a popular farm phenotyping platform for precision agricultural applications (Hoffmann et al., 2016; Hu et al., 2021; Messina and Modica, 2020). Very high resolution (VHR) cameras attached to UAV platforms offer advanced crop image throughput analytics and are effective in overcoming the limitations of satellite imagery (Maes and Steppe, 2019; Nhamo et al., 2020). The spatially explicit UAV images acquired by VHR cameras offer a quick turnaround of spectral information that is useful for detecting changes in crop phenology, foliar temperature, and moisture content (Park et al., 2017; Zhang et al., 2019a). UAV images can be continuously acquired under user-defined ground sampling distances and temporal intervals, which limit atmospheric perturbations such as cloud cover (Cucho-Padin et al., 2020; Nhamo et al., 2020). Therefore, accurate mapping and analysis of agricultural maize fields using a multispectral and thermal

infrared UAV holds significant potential for providing data that informs smallholder farmers on potential crop water stress.

Foliar temperature and stomatal conductance can be optimally assessed using a robust machine learning algorithm that can derive a relationship using spectral bands and vegetation indices (VIs) to predict temperature and conductance (Houshmandfar et al., 2021). VIs are mathematical combinations of image bands that are ratioed for the extraction of spectral properties such as canopy cover, plant vigour and phenology dynamics (Kayet et al., 2016; Xue and Su, 2017). VIs, such as the normalized difference water index (NDWI) and the normalized difference vegetation index (NDVI) have been identified as particularly useful in directly or indirectly quantifying water stress within vegetation (El-Hendawy et al., 2019; Liang et al., 2018; Zarco-Tejada et al., 2012; Zhang and Zhou, 2019). Furthermore, the use of these VIs in combination with machine learning algorithms have proven to be useful in characterizing crop temperature and water stress (Liang et al., 2018; Noi et al., 2017). Considering the potential of utilizing UAV-derived data with machine learning, this study aimed to analyze the utility of the UAV-derived data to predict foliar temperature and stomatal conductance. Specifically, the study sought to predict maize foliar temperature and stomatal conductance using UAV-derived spectral variables (bands and VIs) to quantify potential water stress throughout the growing season on a smallholder farm.

3.2. Materials and Methods

3.2.1. Study site description

Data for this study was collected over a four-month period from February 2021 to May 2021 in the rural area of Swayimane, KwaZulu-Natal, South Africa (29°31'24''S; 30°41'37'' E) (Figure 1). Swayimane is situated in the uMshwathi Local Municipality and is located approximately 55 km north-east of Pietermaritzburg. The small, communal area covers a geographical extent of approximately 36 km². Common crops cultivated in the area include white and yellow maize, sugarcane, amadumbe (*taro*), and sweet potato. The smallholder farmers follow traditional farming methods of planting, maintaining, and manual harvesting of crops. Farm plots are rainfed, fertilized using livestock manure, and hand weeded. Weeds and grass are also controlled using backpack herbicide sprayers. This study examined a 30 × 96 (2850 m²) smallholder maize field that was located on a slope, with a field elevation ranging from 850 m to 839 m.

The area is predominantly characterised by semi-subsistence farming which is regarded as a form of food security and livelihood sustenance. Agriculture and crop production in Swayimane is supported by the favourable environmental conditions of the region. The climate is characterized by warm wet summers and cool dry winters, with an average temperature ranging between 12 °C and 24 °C. Mean annual rainfall ranges between 600 and 1200 mm, with the majority of rain occurring during the summer occasioned by thunderstorms. During data collection, Swayimane had a maximum daily average air temperature of 24 °C and total rainfall of 242.80 mm, amongst other weather data (Figure 2). Weather conditions were monitored continuously by the automatic weather station installed at a Swayimane high school. Weather data was downloaded from the Swayimane weather website. The weather station was situated approximately 2 km from the smallholder maize farm, it was considered proximally adequate in capturing the weather conditions of the study site.

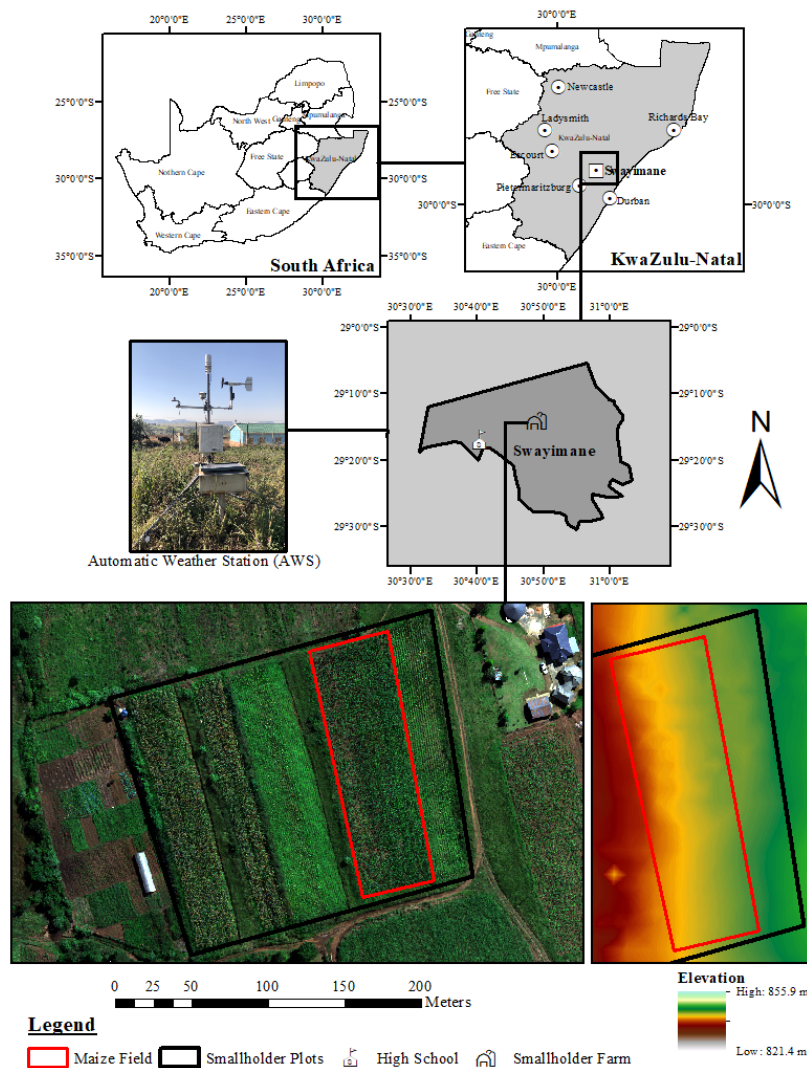


Figure 11: Location of the Swayimane study area, study site, and smallholder maize field.

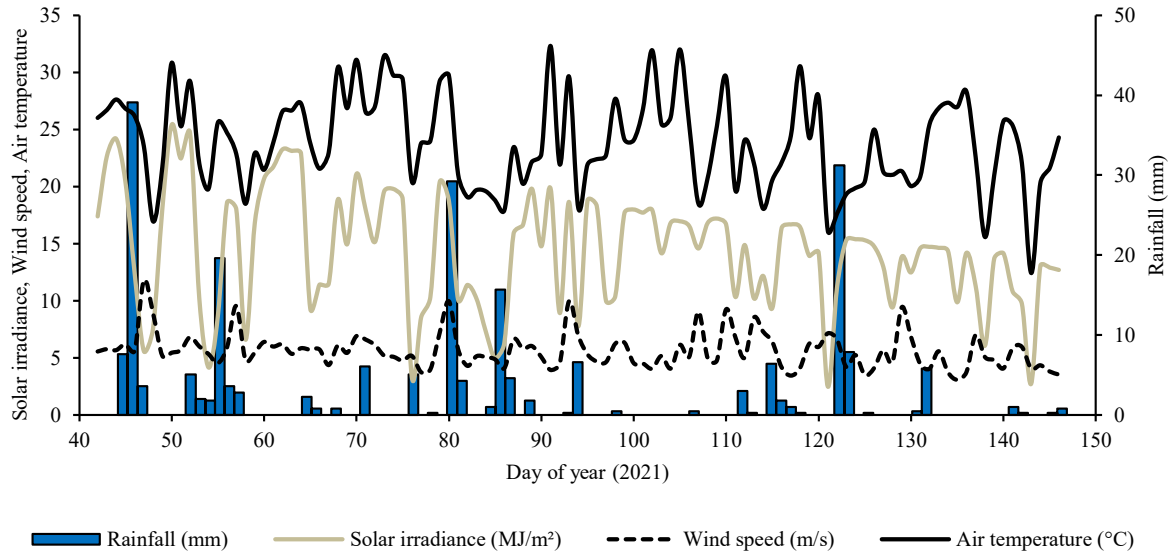









Figure 12: Daily weather conditions in Swayimane over the period of maize phenotyping

3.2.2. *The maize growth cycle and characteristics*

Maize seedlings were sown on the 8th of February 2021 and harvested on the 26th of May 2021 (Table 1), having a total growth cycle of 108 days and temperature and stomatal conductance examined at the various stages of phenotyping. The maize growth cycle is split into vegetative stages (emergence to tasseling based on the number of fully developed leaves) and reproductive stages (silking to physiological maturity based on the degree of kernel growth) (Cakir, 2004; Zhao et al., 2012). Within the various stages, certain transitions are significant for monitoring the potential occurrence of water stress. These being the emergence of crop growth (first day of photosynthetic activity, termed VE), tasseling (day when maximum leaf area is recorded and tassels appear, termed VT) and, commencement of senescence (day when green leaf visibly loses colour) (Du Plessis, 2003).

It is worth mentioning that during the mid-vegetative stage, the western portion (lower elevation) of the field appeared unhealthy. This may have been due to the fact that this portion of the field was not weeded during the early vegetative growth stage with the rest of the field. However, the farmer applied herbicide during the mid-vegetative growth stage to remove grasses and weeds that were found between maize rows. Consequently, the herbicide impacted the health status of these crops and the maize suffered herbicide burn (see Appendix A, Figure 23 for images of this portion of the field).

Table 6: Maize growth stages

Days after emergence	Growth stage	Description	Pictures
0	VE	Germination and emergence. Planting depth 5-8 cm.	
7	V2		
21	V5	Plant population established. Growth point 20-25 mm below surface. Leaf sheath and blades. Tassel initiation.	
32	V8	Ear initiation and early cob development.	
38	V10		
44	V12	Tassel at growth point begins to develop rapidly. Active growth of lateral shoots and cob development from the sixth to eighth node above surface. Brace root development.	
49	V14		
56	VT	Tasseling stage. Silks are developing. The demand for water and nutrients is high. All leaves present. Pollination 5-10 days.	
63	R1		
70	R2 - R3	Kernel development. Silking stage.	
77			
84			
91	R3 - R4	Grain filling. Nutrients are transported to cob. Sugars converted into starch.	
98			
105			
112	R5 - R6	Physiological maturity and drying of kernels. Starch in kernels. End of mass gain.	
119			
160	R+	Ready for harvest. Optimal moisture and nutrients.	

Vegetative Growth Stages

Reproductive Growth Stages

3.2.3. Field data collection, temperature, and stomatal conductance measurements

Field data was collected throughout the maize phenological cycle. A 4-meter meteorological tower was installed at the center of the maize field with two infrared radiometers (IRR) (Apogee SI-111, Apogee Instruments Inc., Logan, UT, USA) (Figure 3). The SI-111 IRR measures surface temperature

by converting the thermal energy radiated from the surface. The SI-111 IRR obtains a spectral range from 8 μm to 14 μm , with measurement ranges from $-60\text{ }^{\circ}\text{C}$ to $110\text{ }^{\circ}\text{C}$, and a manufacturer accuracy of $\pm 0.5\text{ }^{\circ}\text{C}$ (Aragon et al., 2020). The two IRR sensors were attached at a 23 and 45° half-angle field of view (FOV), with one cantered on maize and the other obtaining an azimuth view that was perpendicular to the row direction. The datalogger was programmed (CR1000, Campbell Scientific, Logan Utah, USA) to output average foliar canopy temperature, from 10 second measurements at the following intervals: 5-minutes, 10-minutes, 30-minutes, 60-minutes. IRR measurements were also aggregated to acquire a daily average temperature using the 10-minute data.

The SI-111 radiometers were calibrated in a temperature-controlled chamber with a blackbody cone for the radiation source. This was conducted by holding the SI-111 IRRs in a fixture at the opening of the blackbody cone. The IRR sensors were thermally insulated from the cone and the temperature of each was independently controlled. The IRRs are held at a constant temperature while the cone was controlled at temperatures below $12\text{ }^{\circ}\text{C}$, above $18\text{ }^{\circ}\text{C}$ and equal to the IRR temperature. IRR temperature data was collected at every $10\text{ }^{\circ}\text{C}$, until the IRRs and blackbody cone reach constant temperatures. Every $10\text{ }^{\circ}\text{C}$ IRR temperature data was collected until the IRRs and blackbody cone reached a constant temperature. Moreover, the IRR measurements were used to assess the thermal infrared UAV-derived temperature.

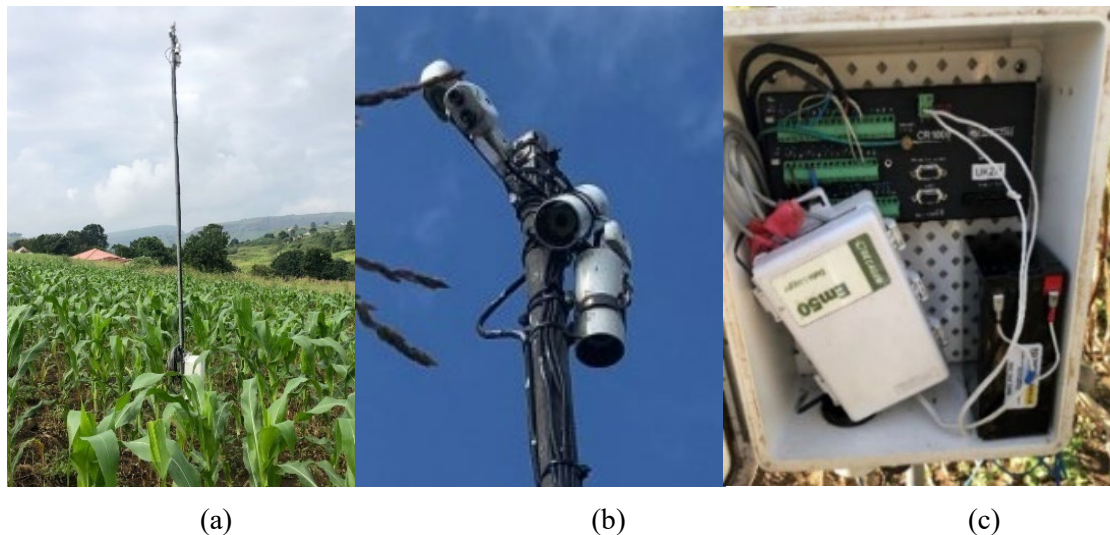


Figure 13: (a) Automated in-field meteorological tower in the maize field, (b) meteorological tower mounted with SI-111 Apogee IRR sensors held 4-meters above the ground, (c) CR1000 data logger, Em50 datalogger and 12 V battery

In-field maize temperature and stomatal conductance measurements were collected from the early vegetative (V5) growth stage to the late reproductive growth stages (R6), at two-week intervals. Pre-sampling of the maize smallholder field was conducted in Google Earth Pro where a polygon of the experimental field was digitized. The digitised polygon was then imported into ArcGIS 10.5 and used to generate sampling points. A total of 63 sample points were generated based on stratified random sampling within the digitized field boundary. These points were then uploaded onto a handheld Trimble Global Positioning System (GPS) with sub-meter accuracy. These locations were used to navigate the field to each sample point during data collection. The maize plants at each sampling point were marked for consistent bi-weekly measurement. The 63 maize points were sampled on six occasions over phenotyping.

A digital laser infrared GM320 handheld thermometer (IRT) was used to measure selected maize foliar temperature. IRT measurements can range from approximately -50 °C to 330 °C. During the vegetative growth stages (where a sixth leaf was present) and during the tasseling stage, the IRT temperature readings were measured on the newest fully expanded leaf with an exposed collar. After the tasseling stage, the ear leaf (i.e., the leaf attached at the same node as the primary ear shank) was measured (Costa et al., 2003). Three foliar temperature measurements were taken and subsequently averaged per sampling point.

Stomatal conductance was measured using a SC-1 leaf porometer (Decagon Devices, Inc., Pullman, WA, USA). Stomatal conductance is the measure of gaseous exchange (i.e., carbon dioxide intake) and transpiration (i.e., water vapour loss) through the leaf stomata, and is a function of the size, density and opening of the leaf stomata (Handiganoor et al., 2018). Leaves with open stomata allow for higher levels of conductance and indicate productive photosynthetic and transpiration rates. While closed leaf stomata indicate potential plant stress.

The SC-1 leaf porometer calibration was done prior to measurements under field conditions. as the leaf clip must be in thermal equilibrium with the environment. This included wetting the filter paper with the distilled water provided in the sensor kit, and then placing the filter paper over the hole of the calibration plate. The sensor head was then attached to the calibration plate where a 30-second measurement started. After the measurement, the sensor was equilibrated, and the sensor head was re-attached for another measurement.

Calibration measurements were repeated up to 10 times until a stable measurement was achieved. Leaf porometer readings were carried out on the same leaf as the IRT temperature readings. During the mid and late reproductive stages, a fully matured maize leaf in full exposure to the sunlight was selected, and the sensor was placed in the middle of the leaf blade perpendicular to the midrib when conducting measurements. The SC-1 leaf porometer automatically measured the leaf stomatal conductance (in $\text{mmol m}^{-2} \text{s}^{-1}$) for a measurement period of 30 seconds, whilst also providing measurements of air temperature and relative humidity. Stomatal measurements approaching $0 \text{ mmol m}^{-2} \text{s}^{-1}$ indicate stress, whereas values close to $500 \text{ mmol m}^{-2} \text{s}^{-1}$ indicate no stress.

At each stage of the maize phenological cycle, IRT (temperature) and SC-1 leaf porometer (stomatal conductance) measurements were consistently taken between 10:00 am and 2:00 pm. The temperature and stomatal conductance data were then added to the 63 sampling points map in a geographical information system (GIS). The point map was then overlaid with the multispectral and thermal UAV imagery of the derived spectral reflectance values from each sampling point.

3.2.4. UAV: DJI Matrice 300 and MicaSense Altum

The DJI Matrice 300 (DJI M-300) platform mounted with a MicaSense Altum camera and Downwelling Light Sensor 2 (DLS-2) was used for aerial-based flights over the smallholder farms. The rotary-wing DJI M-300 series has vertical take-off and landing (VTOL) technology, making it well suited for small-scale agricultural crop imaging (Figure 5a).

The DJI M-300 platform novelties include its 15 km transmission range, 7000 m maximum altitude, obstacle avoidance, flightpath planning and locational position tracker. The maximum flight time of the M-300 is 55 minutes (without payload) and it can reach a maximum speed of 27 m/s, which surpasses most drone platforms on the market. Moreover, the MicaSense Altum camera is a multispectral and thermal imaging sensor that integrates five spectral high-resolution narrow bands (blue, green, red, red-edge, and near-infrared) with a radiometric longwave infrared thermal camera (Figure 5b). The high-performance camera offers synchronised multispectral and thermal image capture and uses a global shutter of up to a one-second capture rate for precise and aligned imagery (Hutton et al., 2020). The multispectral bands have a 2064×1544 at 120 m (3.2 megapixels per multispectral band) sensor resolution and a ground sample distance (GSD) of 5.2 cm per pixel at a height of 120 m. The thermal infrared camera has a 160×120 sensor resolution and a GSD of 81 cm

per pixel at 120 m (Table 2). The multispectral camera has a $48^\circ \times 37^\circ$ FOV, with an 8 mm focal length. While the thermal camera has a $57^\circ \times 44^\circ$ FOV, with a 1.7 mm focal length.



Figure 14: (a) DJI Matrice 300 UAV platform and, (b) MicaSense Altum multispectral-thermal camera

Table 7: MicaSense Altum camera specifications.

Band	Spectral colour	Band center/range	Ground sampling distance at flying height of 120 m
1	Blue	475 nm	5.2 cm per pixel
2	Green	560 nm	5.2 cm per pixel
3	Red	668 nm	5.2 cm per pixel
4	Red-edge	717 nm	5.2 cm per pixel
5	Near-infrared	842 nm	5.2 cm per pixel
6	LWIR thermal infrared	8000 nm – 14000 nm	81 cm per pixel

3.2.5. Image acquisition and processing

A shapefile of the maize field was created in Google Earth Pro and imported into the DJI M-300 smart console, where it was used to design a flight plan covering the study area (Figure 6a; Table 3). The flight plan enabled a hands-free drone flight mission over the study field and adjacent areas. Before and after the flight, the UAV was calibrated using the MicaSense Altum calibrated reflectance panel (CRP). This included the user manually taking an unshaded image directly over the CRP to discern the lighting conditions of the specific flight date, time, and location (Figure 6b). UAV flights were conducted every 2-weeks on days with clear sky conditions. UAV flights were conducted between

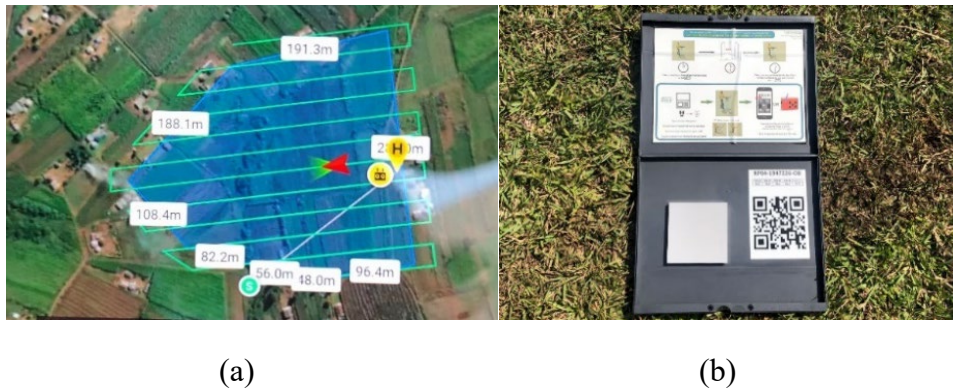


Figure 15: (a) DJI M-300 flight plan, (b) MicaSense Altum calibration reflectance panel

Table 8: UAV flight specifications

Parameters	Specifications
Altitude	100 meters
Ground sampling distance (multispectral)	7 cm
Ground sampling distance (thermal infrared)	109 cm
Speed	16 m/s
Flight duration	14 minutes 36 seconds
Composite images	321
Image overlap	80 %

A total of 3576 images (per flight) were collected, mosaicked and radiometrically corrected (Pix4Dfields 1.8.0, Pix4d Inc., San Francisco, CA, USA). Radiometric correction was conducted in Pix4Dfields using all the captured images, including the before and after flight CRP images. The radiometric calibration target (the CRP) is a white balance card that provided the reflectance properties of the card across the electromagnetic spectrum wavelengths captured by the camera. This enabled the software to calibrate and correct the reflectance of the images accordingly in line with the prevalent atmospheric conditions during the image acquisition. The CRP also obtained an absolute reflectance, which made it possible to compare data from several flights. Once processed, a final orthomosaic and a digital elevation model (DEM) GeoTIFF image was generated. The orthomosaic was georeferenced in ArcGIS 10.5 with the use of ground reference points from Google Earth Pro and referenced to the Universal Transverse Mercator (UTM zone 36S) projection.

The LWIR thermal infrared band was converted to absolute temperature values in Pix4Dfields, using the following equation:

$$\text{Temperature} = \frac{\text{LWIR Thermal Infrared (B6)}}{100} - 273.15 \quad (1)$$

The maize reflectance data was extracted from the multispectral and thermal infrared Altum image. This was done by overlaying the ground-truthed maize IRT temperature and stomatal conductance measurements and their GPS coordinates in the form of a point map with the UAV multispectral-thermal image. The reflectance values were extracted for each coordinate, and for each UAV band. The image was then used to compute vegetation indices (VIs) detailed in Table 4. VIs selected included direct and indirect water-related indices. These VIs were chosen based on their performance in research literature (Panigrahi and Das, 2018; Yang and Du, 2017; Zhang and Zhou, 2019).

3.2.6. Statistical Analysis

The sampled data was randomly partitioned into training (70 %) and testing (30 %) datasets that were used to develop the predictive regression models. A random forest regression algorithm was used to predict maize foliar temperature and stomatal conductance (from spectral bands and VIs), since it is renowned for its simplicity, robust nature, and ability to perform well regardless of sample size (Dye et al., 2011; Luan et al., 2020). The random forest ensemble is a machine learning algorithm that uses bootstrap aggregation to construct multiple trees on a subset of samples derived from the training data (Abdel-Rahman et al., 2013). Decision trees are grown to their maximum capacity with a randomized subset of predictors (UAV-derived spectral data), and each node is split using random subsets of input variables (Adam et al., 2012). Furthermore, the random forest regression has the ability to identify predictor variables that are influential in the prediction model based on the sum of the reduction in Gini impurity across the nodes of the feature (Sibanda et al., 2021).

Specifically, the RGtk2 and rattle packages in RStudio software version 1.4.1564 were used to develop the random forest regression model through numerical inputs. The outputs of the random forest model were optimized using the variable importance scores as they determine the most influential bands and VIs in prediction. Variables of low importance were removed throughout the analysis and the random forest model was continuously modified for optimal prediction. The process of variable selection

reduces issues of variable redundancy and multicollinearity, which affect the performance of the regression model. The model was optimized and fine-tuned by the user to hyper-parameters of 500 trees and 6 variables for temperature and 500 trees and 10 variables for stomatal conductance. These hyper-parameters were attained after numerous iterations.

Table 9: Spectral vegetation indices utilized to predict foliar temperature and stomatal conductance

Vegetation index	Abbreviation	Equation	Reference
Direct water-related indices			
Normalized difference water index	NDWI	$\frac{GREEN - NIR}{GREEN + NIR}$	Yang and Du (2017) and Gao (1996)
Indirect water-related indices			
Normalized difference vegetation index	NDVI	$\frac{NIR - RED}{NIR + RED}$	Panigrahi and Das (2018)
Transformed normalized difference vegetation index	TDVI	$\sqrt{\frac{NIR - RED}{NIR + RED}} + 0.5$	Castellanos-Quiroz et al. (2017)
Normalized difference red-edge index	NDRE	$\frac{NIR - RED\ EDGE}{NIR + RED\ EDGE}$	Song et al. (2010)
Normalized green-red difference index	NGRDI	$\frac{GREEN - RED}{GREEN + RED}$	Song et al. (2010)
Green chlorophyll index	CIgreen	$\left(\frac{NIR}{GREEN}\right) - 1$	Zhang and Zhou (2019)
Red-edge chlorophyll index	CIrededge	$\left(\frac{NIR}{RED\ EDGE}\right) - 1$	Zhang and Zhou (2019)
Green NDVI	GNDVI	$\frac{NIR - GREEN}{NIR + GREEN}$	Song et al. (2010)
Canopy chlorophyll content index	CCCI	$\frac{NIR - RED\ EDGE}{NIR + RED\ EDGE} \frac{NIR - RED}{NIR + RED}$	Fitzgerald et al. (2010)
Chlorophyll vegetation index	CVI	$NIR * \left(\frac{RED}{GREEN^2}\right)$	Vincini and Frazzi (2011)
Enhanced vegetation index	EVI	$\frac{2.5(NIR - RED)}{NIR + 6RED - 7.5BLUE + 1}$	Wiratmoko et al. (2018)

Soil adjusted vegetation index	SAVI	$\frac{(NIR - RED)(1 + L)}{NIR + RED + L}$	Sishodia et al. (2020)
Optimized soil-adjusted vegetation index	OSAVI	$\frac{1.16 (NIR - RED)}{NIR + RED + 0.16}$	Sishodia et al. (2020)

3.2.7. Accuracy assessment

Accuracy assessments were conducted to assess the regression models performance of the predicted foliar temperature and stomatal conductance. The accuracy metrics used were the coefficient of determination (R^2), root-mean-squared error (RMSE), and the relative root-mean-squared error (RRMSE). The R^2 measured the variation between the measured and predicted: foliar temperature and stomatal conductance. The RMSE assessed the magnitude of error between the field measurements and modelled outputs of foliar temperature and stomatal conductance. While the RRMSE evaluated the accuracy of the model and was used to compare the performance of regression models across maize phenotyping. The RRMSE was calculated by normalizing the mean of each variable RMSE value and expressed as a percentage, where lower percentages are considered more accurate (Taghizadeh-Mehrjardi et al., 2020).

3.3. Results

3.3.1. Descriptive analysis of UAV-derived data and SI-111 IRR maize temperature data

3.3.1.1. Maize temperature data over phenotyping

The IRR time-series data was used to plot the difference between IRR foliar canopy temperature (T_c) and air temperature (T_a) (Figure 7). The foliar canopy to air temperature difference ($T_c - T_a$) fluctuated throughout maize phenotyping, as foliar canopy temperatures were influenced by ambient conditions of air temperature, solar radiation, and rainfall. Hence, a similar fluctuation trend was observed for solar radiation and $T_c - T_a$. Days of low solar radiation or rainfall were associated with a lower $T_c - T_a$, and days of high solar radiation were generally associated with a higher $T_c - T_a$.

The trendline through $T_c - T_a$ over the maize growth season shows that a higher $T_c - T_a$ was associated with the early vegetative stages, such as DOY 43 at 3.1 °C, as well as mid-reproductive and late reproductive growth stages, such as DOY 115 at 3 °C and DOY 130 at 2.7 °C, respectively. The maximum $T_c - T_a$ was measured at 3.4 °C during the mid-reproductive stage of DOY 116. This was subsequent to a hailstorm that occurred on DOY 113, which increased the $T_c - T_a$, and also resulted in $T_c - T_a$ to remaining relatively high for the duration of phenotyping at approximately 1.9 °C. A lower $T_c - T_a$ was associated with the mid-vegetative and late vegetative growth stages, such as DOY 85 at -0.8 °C and DOY 90 at -7.3 °C, respectively. DOY 92 had the lowest $T_c - T_a$ at -8.6 °C was recorded during the late vegetative stage on DOY 92 at -8.6 °C.

Generally, the solar radiation and air temperature decreased as the winter season approached. However, the $T_c - T_a$ increased as the winter season approached, suggesting reduced transpiration as a result of water stress during the mid-reproductive and senescence stages of the late reproductive growth stages.

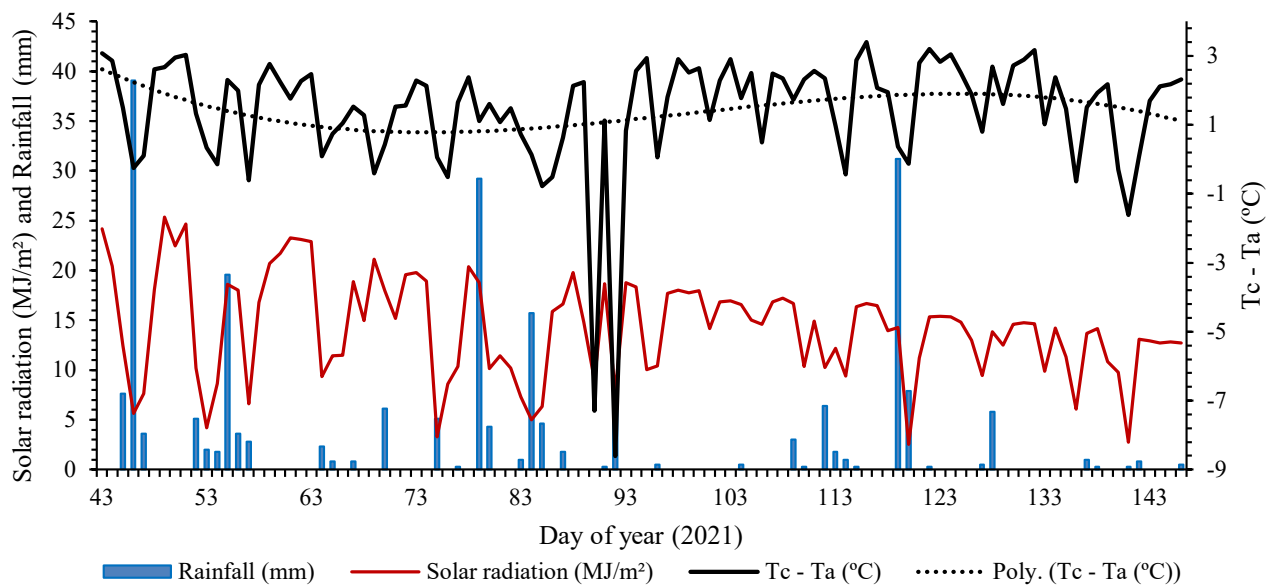


Figure 16: Daily average $T_c - T_a$, solar radiation, and rainfall throughout the maize phenological cycle.

3.3.1.2. Evaluation of UAV thermal imagery against in-field SI-111 IRR temperature sensors

The thermal UAV-derived temperature had a strong positive linear relationship ($R^2 = 0.94$; $p = 0.001$) with the in-field IRR temperature sensors over the various maize growth stages (Figure 8), for the days

UAV imagery was collected. During the early vegetative growth stage, DOY 61, the IRR and UAV temperatures recorded a satisfactory correlation of approximately 29.7 °C to 30.8 °C, respectively. DOY 77, the mid-vegetative stage, had a significant correlation of 22.2 °C and 21.2 °C between IRR and UAV temperatures.”

Furthermore, maize IRR and UAV temperatures correlated significantly during the late vegetative stage (DOY 90) and the early reproductive stage (DOY 102), with temperatures recorded at approximately 27 °C and 24 °C, respectively. However, correlation during the mid-reproductive and late reproductive stages, DOY 118 and DOY 134, deviated from the trendline, due to the maize canopy disturbance by the hailstorm on DOY 113. Hence, IRR and UAV temperatures were recorded at 24 °C and 26 °C for the mid-reproductive stage and 24 °C and 23 °C for late reproductive stage.

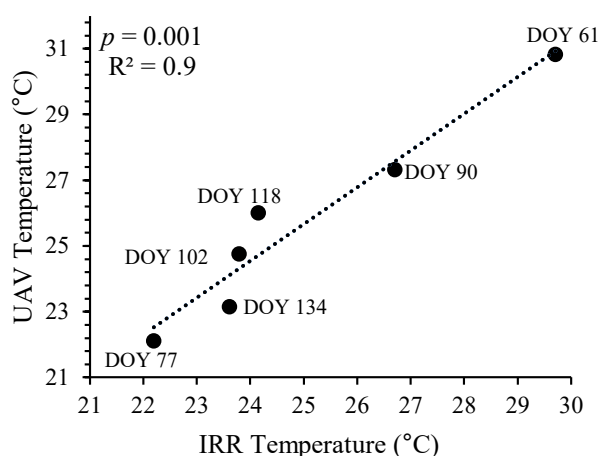


Figure 17: Correlation of in-field IRR sensors and UAV-derived temperature throughout the maize phenological cycle

3.3.2. Descriptive statistics of in-situ maize temperature and stomatal conductance measurements

The IRR and IRT minimum and maximum temperatures of the 63-sampling points were used to illustrate the descriptive temperature statistics (Table 5). The average maximum IRR temperature for the entire phenological cycle was 32.2 °C, and the average IRT temperature for the maize growth cycle was 32.6 °C. This suggested an average temperature offset of 0.4 °C between the IRR and IRT temperature measurements. The highest recorded IRR temperature was 35 °C during the late vegetative growth stage of V14–VT, and the highest recorded IRT temperature was 39.1 °C during the V14–VT growth stage.

The average minimum IRR temperature for the entire phenological cycle was 18.3 °C, and the average IRT temperature for the maize growth cycle was 20.9 °C” This suggested an average temperature offset of 2.6 °C between the IRR and IRT temperature measurements.

The lowest IRR temperature value occurred during the R3 – R4 growth stage at 16 °C, whereas the lowest IRT temperature value occurred during the V12 growth stage at 15.5 °C. The IRR maximum values were within 1.7 standard deviations of the mean, whereas the IRT maximum values were within 5.1 standard deviations of the mean. Similarly, with the minimum values, the standard deviation of the IRR and IRT temperatures were 1.9 and 3.2, respectively. The total mean co-efficients of variation for the maximum IRR was 5.2 %, whereas the maximum co-efficients of variation for the IRT was 15.7 %. Moreover, the minimum IRR and IRT temperatures, had co-efficient of variations of 10.4 % and 15.5 % respectively. The IRR values suggest precise temperature estimates that are close to the mean value.

Table 10: Descriptive statistics of IRR and IRT foliar temperature throughout the maize growth stages

Maize foliar temperature at the various growth stages		Maximum (°C)		Minimum (°C)	
		IRR	IRT	IRR	IRT
DOY 61	V5 – V10	34	32.7	17	21.5
DOY 77	V12	33	23.4	20.5	15.5
DOY 90	V14 – VT	35	39.1	17.1	23.1
DOY 102	R1 – R3	34	33.7	18.9	21.4
DOY 118	R3 – R4	33	34.3	16	19.3
DOY 134	R5 – R6	30	32.3	20.4	24.8
Mean		33.2	32.6	18.3	20.9
Median		33.5	33.2	18	21.5
Standard deviation		1.7	5.1	1.9	3.2
Co-efficient of variation		5.2	15.7	10.4	15.5

The measured maize stomatal conductance varied at the different stages of maize phenotyping (Table 6). The average stomatal conductance over the maize phenotyping was 206.9 mmol m⁻² s⁻¹. The lowest conductance value occurred during the early vegetative growth stage (V5 – V10) at 42 mmol m⁻² s⁻¹, and the highest stomatal conductance occurred during the early reproductive development stage (R1 – R3) at 556.5 mmol m⁻² s⁻¹. Reproductive stages were characterised by higher stomatal conductance values compared to the vegetative stages. However, the average stomatal conductance for the mid-reproductive stage (R2 – R4) decreased to 172.6 mmol m⁻² s⁻¹ due to the crop stress from the hailstorm that occurred on DOY 113. Furthermore, the median value of maize stomatal conductance across the

growing season was $194.6 \text{ mmol m}^{-2} \text{ s}^{-1}$ and the average stomatal conductance values were within 79.3 standard deviations of the mean value.

Table 11: Descriptive statistics of stomatal conductance throughout the maize phenological cycle

Maize stomatal conductance at the various growth stages	Minimum ($\text{mmol m}^{-2} \text{ s}^{-1}$)	Maximum ($\text{mmol m}^{-2} \text{ s}^{-1}$)	Mean ($\text{mmol m}^{-2} \text{ s}^{-1}$)	Median ($\text{mmol m}^{-2} \text{ s}^{-1}$)	Standard deviation
DOY 61 V5 – V10	42	245.1	121.8	112.9	49.25
DOY 77 V12	86.6	556.5	248.5	238.1	113.3
DOY 90 V14 – VT	44.2	404.8	166.5	157.6	73.7
DOY 102 R1 – R2	182.7	480.1	298.9	290.1	79.3
DOY 118 R2 – R4	100.2	373.6	172.6	160.3	55.6
DOY 134 R4 – R5	74.3	483.1	233.3	208.5	104.8
Average value	88.3	423.9	206.9	194.6	79.3

Importantly, foliar temperature and stomatal conductance had a significant inverse relationship, producing an $R^2 = 0.72$ (Figure 9). The negative relationship of stomatal conductance and temperature further enhanced the identification between potential crop water stress. Such a relationship illustrated that when stomatal conductance was low, foliar temperatures were high, i.e., hot canopy. Furthermore, high stomatal conductance was associated with low foliar temperatures i.e., a cool canopy, suggesting optimal maize water productivity.

For example, on DOY 77, the maize temperature was low at $20 \text{ }^\circ\text{C}$ and the stomatal conductance was high at $396 \text{ mmol m}^{-2} \text{ s}^{-1}$, illustrating potentially optimal crop conditions. DOY 61 had a higher maize temperature of $28 \text{ }^\circ\text{C}$ and a lower stomatal conductance of $122 \text{ mmol m}^{-2} \text{ s}^{-1}$, indicating potential water stress.”. Thus, the inverse relationship between foliar temperature and stomatal conductance was useful in estimating crop water stress.

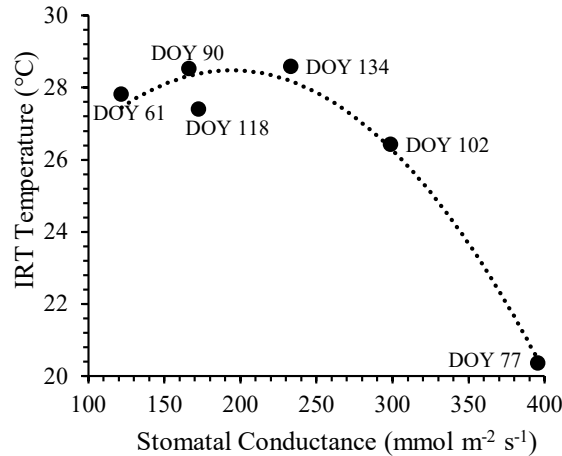


Figure 18: Correlation of foliar temperature and stomatal conductance throughout the maize phenological cycle

3.3.3. UAV-derived data: estimation of maize temperature and stomatal conductance

3.3.3.1. Optimized regression models of maize foliar temperature and stomatal conductance over the phenological stages

For the prediction of maize temperature, the mid-vegetative stage (DOY 77 (V12)) yielded the most optimal modelled RMSE = 0.59 °C and $R^2 = 0.81$ (RRMSE = 2.9 %) (Figure 10 b). The optimal variables for this model were the thermal infrared, followed by red, NGRDI, CVI and NDVI, in order of importance (Figure 11 b). The mid-reproductive stages had a RMSE of 1.24 °C, an R^2 of 0.76, and the worst maize phenology had a RRMSE of 6.20%. Model prediction accuracy improved moderately in the late vegetative stages (DOY 90 (V14–VT)) and early reproductive stages (DOY 102 (R1–R3)), with RMSEs of 1.14 °C, $R^2 = 0.79$ (RRMSE = 4%), respectively. The model from the late reproductive stage (DOY 134 (R5 – R6)) obtained a RMSE = 0.7 °C and $R^2 = 0.78$ (RRMSE = 2.6 %) based on NDRE, OSAVI, CCCI, thermal infrared, and EVI, in order of importance (Figure 10e). The early vegetative stage (DOY 61(V5 – V10)) exhibited a RMSE = 1.29 and $R^2 = 0.69$ (RRMSE = 4.7 %).

In estimating stomatal conductance, the early reproductive stage (DOY 102 (R1 – R3)) produced the most accurate model with a RMSE = 25.9 mmol m⁻² s⁻¹, the highest $R^2 = 0.85$ (and the best RRMSE = 11.5 %) based on NIR, NDRE, Thermal, $CI_{rededge}$, and red-edge, in order of importance (Figure 11 d). Poor stomatal conductance accuracies were attained during the late reproductive stage (DOY 134 (R5 – R6)) with a RMSE = 52.6 mmol m⁻² s⁻¹ and $R^2 = 0.78$ (RRMSE = 23.8 %) using the thermal infrared,

CCCI, blue, $CI_{rededge}$, and CVI in order of importance (Figure 11f). In addition, the late vegetative stages (DOY 90 (V14 – VT)) also yielded a poor model with a RMSE = 51.2 mmol m⁻² s⁻¹ and R² = 0.64 (poorest RRMSE = 28.7 %). The mid-reproductive stage (DOY 118 (R3 – R4)) model produced a RMSE = 44.6 mmol m⁻² s⁻¹ and R² = 0.7 (RRMSE = 25.6 %). The mid-vegetative stage (DOY 77 (V12)) produced the best model accuracies with a RMSE = 34.8 mmol m⁻² s⁻¹ and the worst R² = 0.58 (RRMSE = 20.1%), while the early vegetative stage (DOY 61 (V5 – V10)) produced the best RMSE of 26.5 mmol m⁻² s⁻¹ and R² = 0.73 (RRMSE = 22.9%). The early and mid-reproductive stages were characterised by the red-edge band and the $CI_{rededge}$, respectively, where the red-edge and NIR bands were a clear stand out and optimal model contributors. However, the model achieved higher R² values during the reproductive stages and the more optimal RMSE values during the vegetative stages.

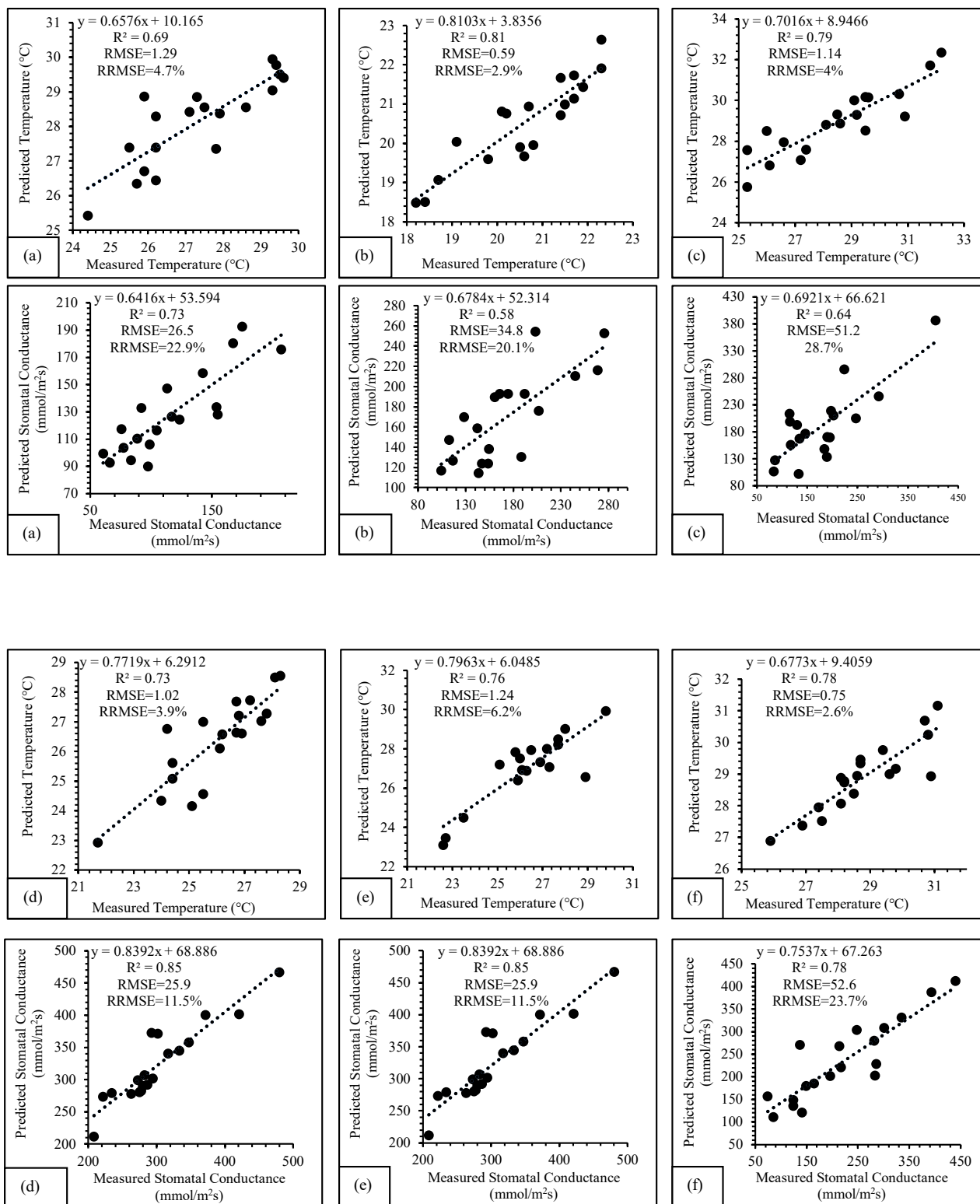


Figure 19: Regression models displaying the relationships between measured and predicted IRT foliar temperature and stomatal conductance throughout the maize phenological cycle: (a) V5 – V10, (b) V12, (c) V14 to VT, (d) R1 – R3, (e) R3 – R4, (f) R5 – R6

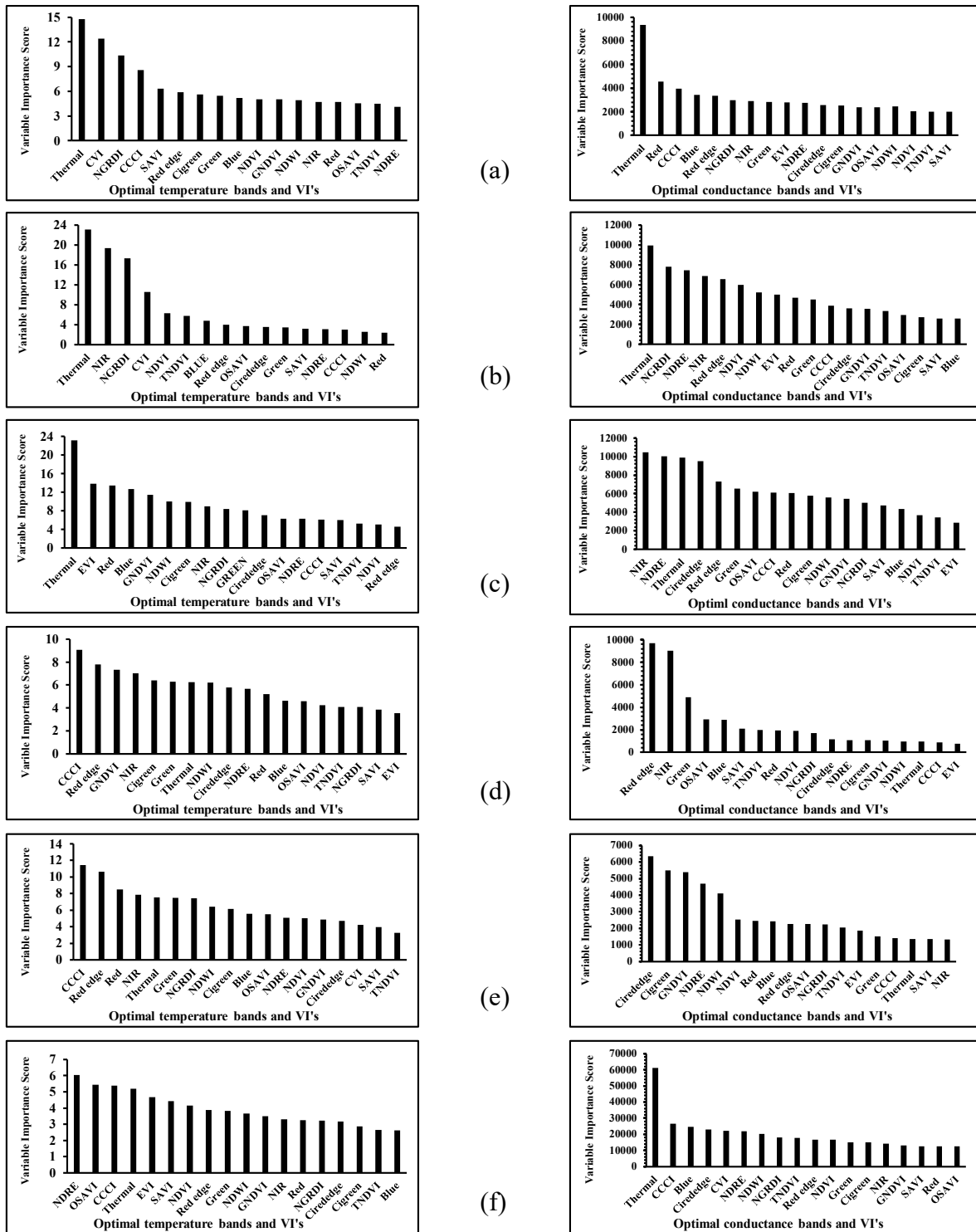


Figure 20: Variable importance scores of optimal foliar temperature and stomatal conductance bands and VIs throughout the phenological cycle: (a) V5 – V10, (b) V12, (c) V14 to VT, (d) R1 – R3, (e) R3 – R4, (f) R5 – R6

3.3.3.2. Mapping the spatial distribution of maize temperature and stomatal conductance over the various phenological stages.

The modelled maize temperature ranged from 8 to 57 °C (Figure 12). It is evident that the maize field temperatures were high during the early vegetative growth stage. Subsequently, during the mid-vegetative growth stage, the field temperature moderately decreased, and further decreased during the late vegetative stage to have the lowest field foliar temperatures. Likewise, in the early reproductive stage, the field was characterised by a generally low temperature, with the exception of the eastern edge (high elevation) of the field. The maize temperature during the mid-reproductive stage increased as a result of the hailstorm damage. During the late reproductive stage, the hailstorm effects increased, which resulted in a further escalation of field temperatures.

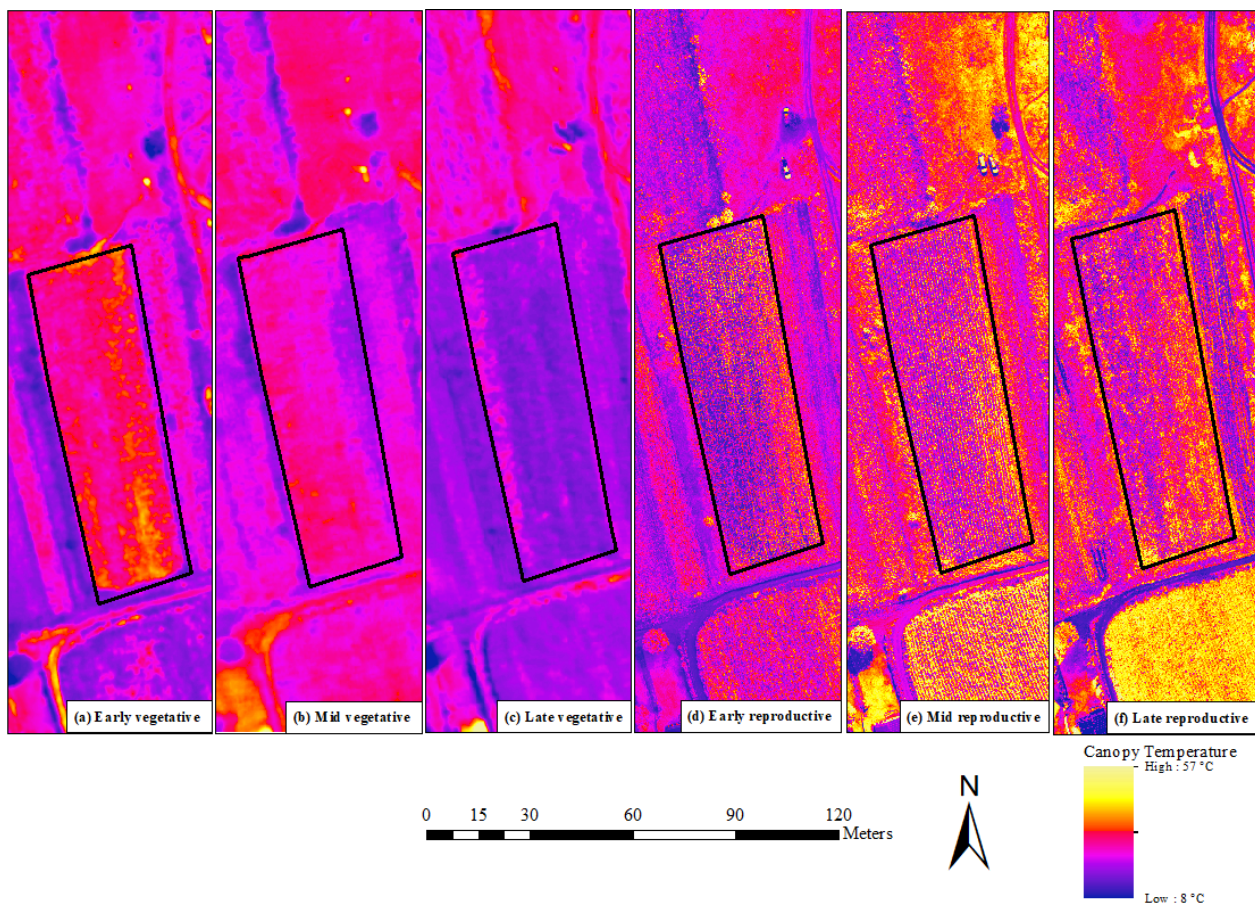


Figure 21: Foliar temperature of maize over the smallholder field for vegetative stages (a) V5 – V10, (b) V12, (c) V14 to VT, and reproductive stages (d) R1 – R3, (e) R3 – R4, (f) R5 – R6.

The spatial distribution of stomatal conductance was estimated based on the optimal models for each maize phenological stage. The stomatal conductance values ranged from 82.2 $\text{mmol m}^{-2} \text{s}^{-1}$ to 683.4 $\text{mmol m}^{-2} \text{s}^{-1}$ (Figure 13). It can be observed that the stomatal conductance of maize was relatively low throughout the maize fields. However, high levels of stomatal conductance were identified during the early vegetative stage towards the southern portion of the field, the eastern part of the field during the late vegetative stage, and the eastern section during the mid-reproductive stage. The remainder of the stages, being the mid-vegetative, early reproductive, and late reproductive, were characterised by lower levels of stomatal conductance. Due to the hailstorm stress and crop senescence, the late reproductive stage had the lowest conductance

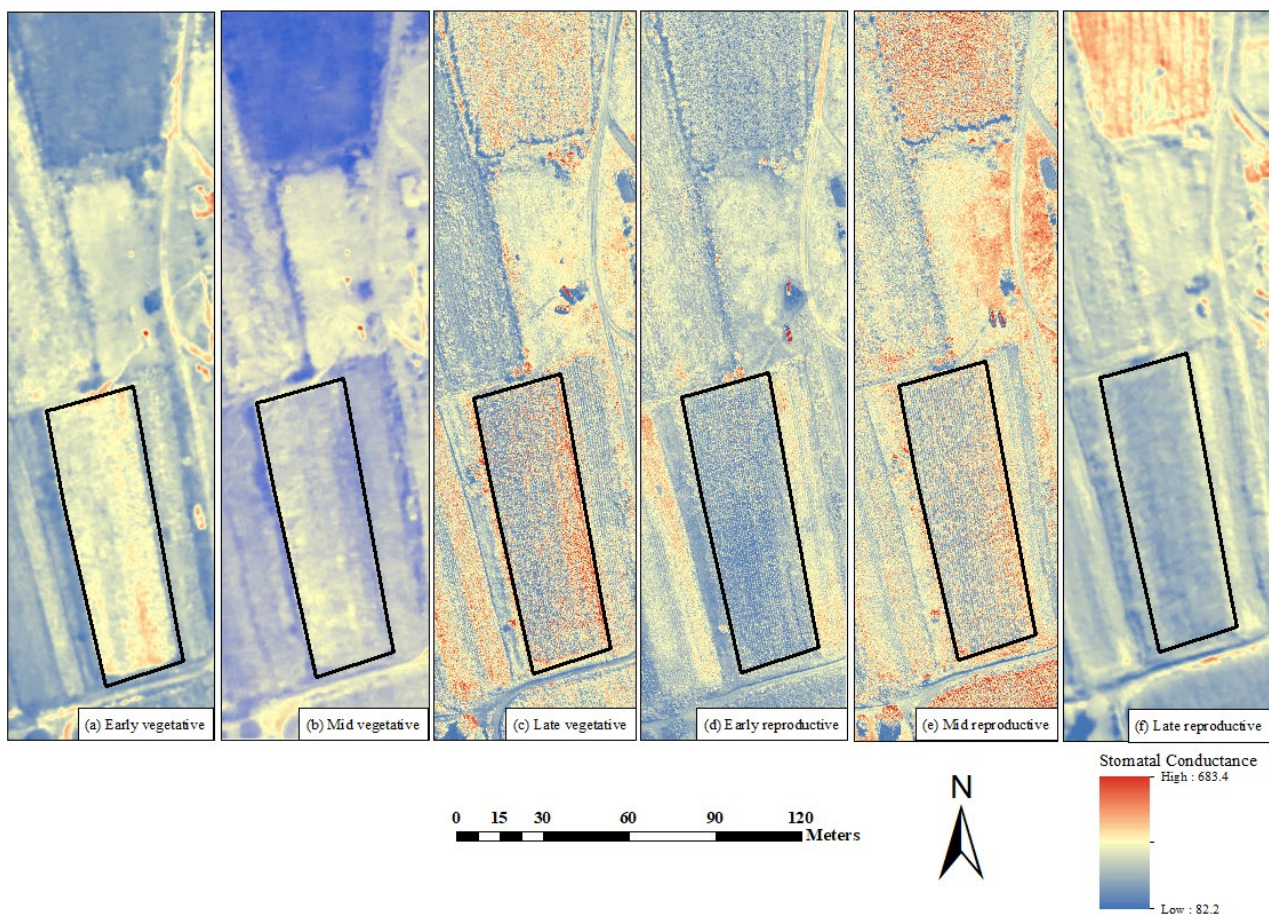


Figure 22: Maize stomatal conductance over the smallholder field for vegetative stages (a) V5 – V10, (b) V12, (c) V14 to VT, and reproductive stages (d) R1 – R3, (e) R3 – R4, (f) R5 – R6.

3.4. Discussion

The objective of this study was to predict maize temperature and stomatal conductance over the various maize growth stages using UAV-derived data in combination with the random forest algorithm. In this regard, the study aimed to determine the most optimal maize growth stage(s) for temperature and stomatal conductance model estimation. It was evident that maize foliar temperatures and stomatal conductance differed throughout phenotyping, and the UAV-derived data could discern the optimal growth stages for the characterization of temperature and stomatal conductance as proxies for crop water stress. For this purpose, the foliar temperature and stomatal conductance data were used to understand the potential crop water stress and moisture status of the smallholder field throughout the growing stages.

3.4.1. Prediction of maize water stress using foliar temperature and stomatal conductance

The regression models were set to predict maize foliar temperature and stomatal conductance using the thermal infrared and multispectral UAV data. Generally, the random forest model performed relatively well in predicting both maize foliar temperature and stomatal conductance over the various growing stages. Specifically, the random forest model achieved stronger prediction accuracies for foliar temperature in comparison to stomatal conductance over maize phenotyping.

The maize foliar temperature was optimally predicted during the mid-vegetative growth stage (RMSE = 0.59 °C, $R^2 = 0.81$ and RRMSE = 2.9%) based on the thermal infrared, followed by the NIR, NGRBI, EVI and NDVI, in order of importance. It has been illustrated in literature that the water content of crop leaves is directly associated with the foliar reflectance across the electromagnetic spectrum (Gerhards et al., 2019; Mangus et al., 2016). Specifically, foliar temperature was strongly detected by the thermal infrared as it can sense emitted radiant energy; hence, it is commonly used for evaluating crop water stress (Brenner et al., 2017; Prakash, 2000; Zarco-Tejada et al., 2012). Moreover, the NIR region was valuable in quantifying crop water status due to its strong water absorption ability that can detect crop water stress based on reflectance variation (Das et al., 2021). Thus, the crop surface temperatures were strongly detected by the thermal infrared and NIR wavebands, hence their crucial role in predicting the maize temperature variability during vegetative growth stages.

Specifically, during the vegetative stages, the maize canopy structure is in development, thus exposing the underlying soil surface, which absorbs and retains thermal radiation (Zhang et al., 2019a). As a result, the high ambient soil temperatures influence the maize temperature, especially during early vegetative growth when there is maximum soil exposure. However, as the canopy structure develops, soil influence is reduced, and crops generally experience lower leaf temperatures. Since, stomata are generally more numerous on the underside of the leaf, they are influenced by the heat of the soil which reaches the underside due to convection (Göbel et al., 2019; Nejad, 2011). This reduces the stomatal conductance levels, as the crop closes the stomata to retain moisture and subsequently experiences higher foliar temperatures (van der Vyver and Peters, 2017). Hence, the thermal infrared section was a strong predictor variable of foliar temperature due to its ability to overcome the influence of soil temperature during the stages of minimal canopy closure.

Nevertheless, the temperature of a leaf, relative to the surrounding air temperature, is primarily influenced by the plant's photosynthetic capacity, as well as the productivity of the internal structural leaf components such as the air cavities, chloroplasts, and mesophyll cell thickness (Peñuelas et al., 1993; Ustin and Jacquemoud, 2020). Thus, when a crop is water-stressed, the molecular leaf networks transmit a signal to initiate physiological and biochemical changes that regularly result in increased foliar temperatures relative to the air temperatures (Bonada et al., 2013; Hasanuzzaman et al., 2013; Osakabe et al., 2014). However, when there is optimal water present, the $T_c - T_a$ remains low as there are productive rates of transpiration and photosynthesis. Therefore, the sustained influence of the thermal infrared and chlorophyll-based VIs during vegetative growth stages, suggested that the crop was optimally transpiring, with no water stress. However, the relatively high maize leaf temperatures measured in combination with the high $T_c - T_a$ during the early vegetative stage suggested slight water stress at crop emergence.

During the reproductive stages, the importance of the thermal infrared waveband decreased and spectral wavelengths such as the red-edge and NIR, as well as VIs derived from these sections, were found to be more important in facilitating the prediction of foliar temperature. This could be attributed to the fact that there was minimal soil exposure due to the fully developed canopy structure. More specifically, the red-edge borders the absorption of photosynthetic pigments such as chlorophyll, which tend to be more vigorous in fully developed canopies (Bano et al., 2015; Ciganda et al., 2012). Generally, the change in chlorophyll affects the photosynthetic rates which indirectly alters the

temperature tolerance and further the stomatal conductance of the crop, inherently indicating crop water productivity (Yordanov et al., 1997). Additionally, during these stages, there is a higher leaf area index, facilitating multiple leaf scattering and reduced transmittance through the leaf due to stronger chlorophyll concentrations optimally identified by the NIR region (Sibanda et al., 2021; Ustin and Jacquemoud, 2020). Hence, the significant contribution of chlorophyll-based indices from the red-edge and NIR sections, such as the CCCI, NDRE, and GNDVI, during the reproductive stages of temperature prediction. However, the hailstorm occurrence during the mid-reproductive stage damaged the maize canopy structure and exposed underlying soil, causing poorer model prediction due to the spectral confusion between soil and foliar temperatures (see Appendix A, Figures 24 and 25 for images of crop hail damage). Subsequent to the hailstorm, the $T_c - T_a$ increased due to the canopy damage that caused increased crop temperatures. This increase indicated potential crop water stress during the mid-reproductive and late reproductive stages.

Meanwhile, maize stomatal conductance was optimally predicted during the early reproductive stage (RMSE = 25.9 mmol m⁻² s⁻¹, R² = 0.85 and RRMSE = 11.5%) based on the red-edge, followed by the NIR, green, OSAVI and blue band, in order of importance. Literature has confirmed that the red-edge region is renowned for its relation to plant water stress and evapotranspiration (Ballester et al., 2019; Niu et al., 2019; Vitrack-Tamam et al., 2020). This is because the red-edge is layered with physiological and chemical processes that reflect the photosynthetic activity of the crop, which indicate stomatal conductance and the potential for crop water stress (Dobrowski et al., 2005; Zarco-Tejada et al., 2003). Specifically, during photosynthesis, the red-edge overlaps the fluorescence emission, which affects the degree of reflection and corroborates the dependence of stomatal conductance on photosynthetic activity (Vitrack-Tamam et al., 2020). Moreover, denser canopies are known to provide increased accuracy in estimates of photosynthetic capacity and stomatal conductance through the NIR region (Carter, 1998; Waring and Landsberg, 2011). Optimal stomatal activities are also associated with rapid chlorophyll development, which reflects highly in the red-edge and NIR (Ballester et al., 2019). Hence, the optimal influence of the red-edge and NIR wavebands, as well as indices derived from these sections in estimating the stomatal conductance of maize in smallholder farms, especially during the reproductive stages.

During the early reproductive stage, the crop was almost at peak biomass and obtained a high leaf surface area that promoted faster rates of photosynthesis and conductance to support fruit development

(Dai et al., 2004; Yordanov et al., 1997). The measured stomatal activities were most prominent during this stage as a high foliar surface area was generally associated with the presence of more stomata on the leaf (Li et al., 2004). Hence, transpiration rates are more dynamic, and the leaf stomata open, facilitating high levels of productivity through optimal foliar conductance and cooling of crop temperatures (Gerhards et al., 2019). Such processes, during the early reproductive stage, indicate crop productivity and optimal moisture content, which influence the strong reflectance of the leaf tissue in the red-edge and NIR regions. Even though during these stages the crop was undergoing developmental processes that required high amounts of water (tasseling, silking, and kernel development), the maize measured an optimal foliar temperature and high stomatal conductance, suggesting crop water productivity and minimal crop water stress for the smallholder farm. However, the hailstorm, during the mid-reproductive stage disturbed the maize canopy structure and resulted in low measured stomatal conductance. Subsequently, this resulted in the thermal infrared being an important predictor due to damage for the canopy and exposure of soil. Furthermore, the high $T_c - T_a$ indicated that the hailstorm damage initiated crop water stress, as foliar temperatures increased and stomatal conductance was reduced in the mid-reproductive and later reproductive stages. Similarly, this was also the case during the early vegetative stage, as stomatal conductance was fairly low and $T_c - T_a$ measured high.

Finally, the prediction model proved that a combination of UAV multispectral and thermal wavebands, as well as UAV-derived VIs, can accurately predict maize foliar temperature and stomatal conductance. The variables of importance for both foliar temperature and stomatal conductance were fairly similar in their contributions towards the model development throughout maize phenotyping. Thus, this indicates that foliar temperature and stomatal conductance are independent, yet interrelated functions, which holistically can be used to understand the potential of crop water stress. Therefore, timeously predicting maize foliar temperature and stomatal conductance allows for smallholder farmers to make decisions at almost near real time that aids in water related crop productivity.

3.4.2. Implications of the study

Smallholder farming systems often lack the resources to initiate successful farming practices, as commercial agriculture tends to be the focus of contemporary innovation and development. Thus, the findings of this study imply that the incorporation of multispectral and thermal infrared UAV

technology could facilitate in-depth analysis of crop water stress, through temperature and stomatal conductance as proxies. In this regard, the findings of the study are useful to inform smallholder agriculture management by suggesting the potential implementation of irrigation schedules at crucial water stages (i.e., tasseling, silking, and pollination). Moreover, the UAV-derived data identified stages of high temperatures and low stomatal conductance (i.e., early vegetative stage), suggesting a potential moisture deficit and, thus, the need for necessary interventional irrigation schedules to ensure optimal crop productivity and development. Specifically, irrigation during vegetative stages may aid optimal productivity and the prevention of early crop water stress.

The hailstorm during the mid-reproductive stages caused damage to the maize canopy structure and led to adverse effects on crop growth as well as premature senescence. Subsequent in-field measurements of stomatal conductance reflected potential stress, as stomatal conductance values were much lower than typical values expected during this growth stage. Additionally, foliar temperature measurements were also relatively high and indicated mild stress, especially during the late reproductive stage. Such agrometeorological effects prove how South African smallholder farmers are susceptible to weather events that have major consequences on crop water productivity. Thus, the use of UAV-derived data enables the identification of such occurrences in almost near real-time, allowing farmers to make rapid, informed, and effective decisions on the subsequent management of the crop. This is crucial as it affects the food security and socio-economic growth of smallholder farmers who rely on healthy and moisture-filled crop yields. Therefore, smallholder farmers benefit from the quick turnaround analysis of the UAV data and can ensure prompt remedial measures to prevent further crop stress.

3.5. Conclusion

Premised on the findings of the study, it can be concluded that foliar temperature and stomatal conductance are adequate indicators to quantify proxies of water stress throughout the growing period. Foliar temperature yielded higher prediction accuracies as compared to stomatal conductance. Nevertheless, the random forest regression model optimally predicted both indicators throughout maize phenotyping. Specifically:

- The UAV-derived multispectral data and thermal infrared waveband optimally estimated maize temperature during the mid-vegetative stage to a $RMSE = 0.59\text{ }^{\circ}C$ and $R^2 = 0.81$ ($RRMSE =$

2.9%) based on the thermal infrared, followed by the NIR, NGRBI, EVI and NDVI, in order of importance,

- The multispectral and thermal infrared data optimally predicted stomatal conductance during the early reproductive stage to a RMSE = 25.9 mmol m⁻² s⁻¹ and R² = 0.85 (RRMSE = 11.5%) based on the red-edge band, followed by the NIR, green, OSAVI and blue band, in order of importance.

Considering the results of the study, UAV technology is a plausible, flexible, and accurate earth observation technique useful for small-scale farming applications. This is because UAV-derived data provides information at improved spatial resolutions to help smallholder farmers understand their crop dynamics and further make informed, farm management decisions. Specifically, the use of multispectral and thermal infrared UAV-data is a step towards the attainment of an agroclimatic smart, near real-time and high spatial resolution technology for assessing crop water stress through foliar temperature and stomatal conductance. However, the study could have benefitted from higher spectral resolution data and additional measured testing data for an improved model performance. Nevertheless, the random forest model performed relatively well at estimating maize leaf temperature and stomatal conductance in the Swayimane area. Therefore, the implementation of low-cost, evidence-based and almost near real-time solutions to smallholder agriculture is beneficial in facilitating improved interventions in these agricultural systems.

CHAPTER 4: SYNTHESIS AND CONCLUSIONS

4.1. A reflection of using UAV-derived data for crop health and water stress

Smallholder agricultural systems are major contributors to agricultural production, food security and socio-economic growth in South Africa. However, smallholder farmers often face challenges related to crop water stress due to climatic variability, crop damage due to erratic weather events, and a lack of resources that are generally found in commercial agriculture. Consequently, their productivity potential is often not realized, and they tend to face issues of unhealthy and water-stressed crops with reduced yields. Recently, precision technologies in the form of UAVs have become an effective, low-cost, and almost near real-time solution in smallholder farming systems, as such technology assists in the optimisation of crop productivity. Specifically, in rural smallholder agricultural systems, farmers rely on healthy and productive maize crop yields, as productive yields generate more revenue. Thus, high resolution UAV-derived data paired with a robust machine learning algorithm provides an in-depth analysis of crop dynamics of chlorophyll content, foliar temperature, and stomatal conductance. Such insights on crop health and water-related indicators, across the maize phenological cycle facilitate improved agricultural management within smallholder farms.

This study aimed to demonstrate the utility of multispectral and thermal infrared UAV-derived data to estimate maize crop health and potential water stress on smallholder farms. The results of these investigations demonstrated that UAV-derived data can predict maize health and water stress, specifically through indicators of chlorophyll content, foliar temperature, and stomatal conductance. These indicators were optimally predicted across maize phenotyping and can be utilized to inform smallholder farmers on the health status of their crops. The model was most accurate in the prediction of foliar temperature stage (RRMSE = 2.6 %, $R^2 = 0.81$, RMSE = 0.59 °C), followed by chlorophyll content reproductive (RRMSE = 7 %, $R^2 = 0.89$, RMSE = 87.4 $\mu\text{mol m}^{-2}$) and the stomatal conductance (RRMSE = 11.5 %, $R^2 = 0.85$, RMSE = 25.9 $\text{mmol m}^{-2} \text{s}^{-1}$), respectively. Specifically, the optimal growth stages for prediction were the early reproductive stage (chlorophyll), the mid-vegetative stage (foliar temperature), and the early reproductive stage (stomatal conductance). Predicted chlorophyll, foliar temperature, and stomatal conductance results were mapped over the maize growth cycle. Such findings could be optimally utilised to characterise the general state of maize health and water stress on smallholder farms. Finally, continuous time-series NDVI and canopy foliar temperature data, as well as metrological data were recorded to observe seasonal fluctuations in NDVI and canopy foliar

temperatures in contrast to the snapshots of the UAV data. The overall results demonstrated that such technology provides smallholder farmers with important in-field information on crop biophysical factors, allowing them to make informed, tactical decisions for improved interventions on crop management through various stages of phenotyping.

4.2. Limitations and recommendations for future research

Although the UAV on-board sensor provided a high spatial resolution, the spectral resolution of the sensor limited the multispectral bands and derived vegetation indices choices. Specifically, a spectral sensor attaining the shortwave infrared section would have been particularly useful to this study, as these wavelengths are instrumental in identifying plant water stress and deriving direct water-related indices. The use of higher spectral resolution data may allow for more precise spectral extraction, especially during the early growth stages when the crop foliar canopy has not yet developed. Furthermore, this may have also resulted in improved model performance and more detailed map outputs of foliar temperature and stomatal conductance across the study area. It is therefore recommended that future crop water stress studies explore the use of a camera with additional wavebands, although this needs to be weighed up against the additional cost of the camera sensor.

The measured chlorophyll, IRT and stomatal conductance data were limited by the study area, and thus, the study used two independent sets of data to train and test the model. Some studies achieved improved results through the incorporation of a third set of independent data to test the model. For example, total evapotranspiration data may have benefitted the study, especially towards the quantification of potential maize water stress. Thus, it is recommended that further analysis of model performance is undertaken in the future when more data becomes available. Finally, this study specifically examined a maize crop; therefore, it is recommended that research should focus on alternative crops cultivated by smallholder farmers. In addition, consideration of different climatic conditions and at different UAV temporal scales would be beneficial.

REFERENCES

- Abdel-Rahman, E.M., Ahmed, F.B. and Ismail, R., 2013. Random forest regression and spectral band selection for estimating sugarcane leaf nitrogen concentration using EO-1 Hyperion hyperspectral data. *International Journal of Remote Sensing*, 34(2): 712-728.
- Abraha, M. and Savage, M., 2006. Potential impacts of climate change on the grain yield of maize for the midlands of KwaZulu-Natal, South Africa. *Agriculture, ecosystems & environment*, 115(1-4): 150-160.
- Adam, E., Mutanga, O., Rugege, D. and Ismail, R., 2012. Discriminating the papyrus vegetation (*Cyperus papyrus* L.) and its co-existent species using random forest and hyperspectral data resampled to HYMAP. *International Journal of Remote Sensing*, 33(2): 552-569.
- Adisa, O.M., Botai, C.M., Botai, J.O., Hassen, A., Darkey, D., Tesfamariam, E., Adisa, A.F., Adeola, A.M. and Ncongwane, K.P., 2018. Analysis of agro-climatic parameters and their influence on maize production in South Africa. *Theoretical and applied climatology*, 134(3): 991-1004.
- Afzal, A. and Mousavi, S.-F., 2008. Estimation of moisture in maize leaf by measuring leaf dielectric constant. *Int J Agricul Biol*, 10: 66-68.
- Ahumada-Orellana, L., Ortega-Farías, S., Poblete-Echeverría, C. and Searles, P.S., 2019. Estimation of stomatal conductance and stem water potential threshold values for water stress in olive trees (cv. Arbequina). *Irrigation Science*, 37(4): 461-467.
- Anderson, H.B., Nilsen, L., Tømmervik, H., Karlsen, S.R., Nagai, S. and Cooper, E.J., 2016. Using ordinary digital cameras in place of near-infrared sensors to derive vegetation indices for phenology studies of High Arctic vegetation. *Remote Sensing*, 8(10): 847.
- Andersson, J., Zehnder, A.J., Jewitt, G.P. and Yang, H., 2009. Water availability, demand and reliability of in situ water harvesting in smallholder rain-fed agriculture in the Thukela River Basin, South Africa. *Hydrology and Earth System Sciences*, 13(12): 2329-2347.
- Aragon, B., Johansen, K., Parkes, S., Malbeteau, Y., Al-Mashharawi, S., Al-Amoudi, T., Andrade, C.F., Turner, D., Lucieer, A. and McCabe, M.F., 2020. A calibration procedure for field and UAV-based uncooled thermal infrared instruments. *Sensors*, 20(11): 3316.
- Baiphethi, M.N. and Jacobs, P.T., 2009. The contribution of subsistence farming to food security in South Africa. *Agrekon*, 48(4): 459-482.
- Ballester, C., Brinkhoff, J., Quayle, W.C. and Hornbuckle, J., 2019. Monitoring the effects of water stress in cotton using the green red vegetation index and red edge ratio. *Remote Sensing*, 11(7): 873.
- Bano, S., Aslam, M., Saleem, M., Basra, S. and Aziz, K., 2015. Evaluation of maize accessions under low temperature stress at early growth stages. *J. Anim. Plant Sci*, 25(2): 392-400.
- Berra, E. and Peppas, M., 2020. Advances and Challenges of UAV SFM MVS Photogrammetry and Remote Sensing: Short Review, 2020 IEEE Latin American GRSS & ISPRS Remote Sensing Conference (LAGIRS). IEEE, pp. 533-538.
- Boken, V.K. and Shaykewich, C.F., 2002. Improving an operational wheat yield model using phenological phase-based Normalized Difference Vegetation Index. *International Journal of Remote Sensing*, 23(20): 4155-4168.
- Bonada, M., Sadras, V., Moran, M. and Fuentes, S., 2013. Elevated temperature and water stress accelerate mesocarp cell death and shrivelling, and decouple sensory traits in Shiraz berries. *Irrigation Science*, 31(6): 1317-1331.
- Brenner, C., Thiem, C.E., Wizemann, H.-D., Bernhardt, M. and Schulz, K., 2017. Estimating spatially distributed turbulent heat fluxes from high-resolution thermal imagery acquired with a UAV system. *International Journal of Remote Sensing*, 38(8-10): 3003-3026.
- Broge, N.H. and Leblanc, E., 2001. Comparing prediction power and stability of broadband and hyperspectral vegetation indices for estimation of green leaf area index and canopy chlorophyll density. *Remote sensing of environment*, 76(2): 156-172.
- Cakir, R., 2004. Effect of water stress at different development stages on vegetative and reproductive growth of corn. *Field Crops Research*, 89(1): 1-16.

- Carroll, D.A., Hansen, N.C., Hopkins, B.G. and DeJonge, K.C., 2017. Leaf temperature of maize and Crop Water Stress Index with variable irrigation and nitrogen supply. *Irrigation Science*, 35(6): 549-560.
- Carter, G.A., 1998. Reflectance wavebands and indices for remote estimation of photosynthesis and stomatal conductance in pine canopies. *Remote Sensing of Environment*, 63(1): 61-72.
- Castellanos-Quiroz, H.O.A., Ramírez-Daza, H.M. and Ivanova, Y., 2017. Detection of open-pit mining zones by implementing spectral indices and image fusion techniques. *Dyna*, 84(201): 42-49.
- Ciganda, V.S., Gitelson, A.A. and Schepers, J., 2012. How deep does a remote sensor sense? Expression of chlorophyll content in a maize canopy. *Remote Sensing of Environment*, 126: 240-247.
- Clevers, J.G. and Gitelson, A.A., 2013. Remote estimation of crop and grass chlorophyll and nitrogen content using red-edge bands on Sentinel-2 and-3. *International Journal of Applied Earth Observation and Geoinformation*, 23: 344-351.
- Costa, C., Dwyer, L.M., Dutilleul, P., Stewart, D.W., Ma, B.L. and Smith, D.L., 2001. Interrelationships of applied nitrogen, SPAD, and yield of leafy and non-leafy maize genotypes. *Journal of plant nutrition*, 24(8): 1173-1194.
- Costa, C., Frigon, D., Dutilleul, P., Dwyer, L.M., Pillar, V.D., Stewart, D.W. and Smith, D.L., 2003. Sample size determination for chlorophyll meter readings on maize hybrids with a broad range of canopy types. *Journal of plant Nutrition*, 26(5): 1117-1130.
- Cucho-Padin, G., Loayza, H., Palacios, S., Balcazar, M., Carbajal, M. and Quiroz, R., 2020. Development of low-cost remote sensing tools and methods for supporting smallholder agriculture. *Applied Geomatics*, 12(3): 247-263.
- Curran, P.J., Dungan, J.L. and Gholz, H.L., 1990. Exploring the relationship between reflectance red edge and chlorophyll content in slash pine. *Tree physiology*, 7(1-2-3-4), pp.33-48.
- Dahms, T., Seissiger, S., Conrad, C. and Borg, E., 2016. MODELLING BIOPHYSICAL PARAMETERS OF MAIZE USING LANDSAT 8 TIME SERIES. *International Archives of the Photogrammetry, Remote Sensing & Spatial Information Sciences*, 41.
- Dai, Y., Dickinson, R.E. and Wang, Y.-P., 2004. A two-big-leaf model for canopy temperature, photosynthesis, and stomatal conductance. *Journal of climate*, 17(12): 2281-2299.
- Das, B., Sahoo, R.N., Pargal, S., Krishna, G., Verma, R., Viswanathan, C., Sehgal, V.K. and Gupta, V.K., 2021. Evaluation of different water absorption bands, indices and multivariate models for water-deficit stress monitoring in rice using visible-near infrared spectroscopy. *Spectrochimica Acta Part A: Molecular and Biomolecular Spectroscopy*, 247: 119104.
- Delegido, J., Verrelst, J., Alonso, L. and Moreno, J., 2011. Evaluation of sentinel-2 red-edge bands for empirical estimation of green LAI and chlorophyll content. *Sensors*, 11(7): 7063-7081.
- Dhau, I., Adam, E., Mutanga, O. and Ayisi, K.K., 2018. Detecting the severity of maize streak virus infestations in maize crop using in situ hyperspectral data. *Transactions of the Royal Society of South Africa*, 73(1): 8-15.
- Dobrowski, S., Pushnik, J., Zarco-Tejada, P.J. and Ustin, S.L., 2005. Simple reflectance indices track heat and water stress-induced changes in steady-state chlorophyll fluorescence at the canopy scale. *Remote sensing of environment*, 97(3): 403-414.
- Du Plessis, J., 2003. Maize production. Department of Agriculture Pretoria, South Africa.
- Dube, T. and Mutanga, O., 2015. Evaluating the utility of the medium-spatial resolution Landsat 8 multispectral sensor in quantifying aboveground biomass in uMgeni catchment, South Africa. *ISPRS Journal of Photogrammetry and Remote Sensing*, 101: 36-46.
- Duveiller, G., López-Lozano, R. and Baruth, B., 2013. Enhanced processing of 1-km spatial resolution fAPAR time series for sugarcane yield forecasting and monitoring. *Remote Sensing*, 5(3): 1091-1116.
- Dye, M., Mutanga, O. and Ismail, R., 2011. Examining the utility of random forest and AISA Eagle hyperspectral image data to predict *Pinus patula* age in KwaZulu-Natal, South Africa. *Geocarto International*, 26(4): 275-289.
- El-Hendawy, S.E., Al-Suhaibani, N.A., Elsayed, S., Hassan, W.M., Dewir, Y.H., Refay, Y. and Abdella, K.A., 2019. Potential of the existing and novel spectral reflectance indices for estimating the leaf water status and grain yield of spring wheat exposed to different irrigation rates. *Agricultural Water Management*, 217: 356-373.

- Fitzgerald, G., Rodriguez, D. and O'Leary, G., 2010. Measuring and predicting canopy nitrogen nutrition in wheat using a spectral index—The canopy chlorophyll content index (CCCI). *Field Crops Research*, 116(3): 318-324.
- Flynn, K.C., Frazier, A.E. and Admas, S., 2020. Performance of chlorophyll prediction indices for *Eragrostis tef* at Sentinel-2 MSI and Landsat-8 OLI spectral resolutions. *Precision Agriculture*: 1-15.
- Gao, B.-C., 1996. NDWI—A normalized difference water index for remote sensing of vegetation liquid water from space. *Remote sensing of environment*, 58(3): 257-266.
- Gerhards, M., Schlerf, M., Mallick, K. and Udelhoven, T., 2019. Challenges and future perspectives of multi-/Hyperspectral thermal infrared remote sensing for crop water-stress detection: A review. *Remote Sensing*, 11(10): 1240.
- Gitelson, A.A., Peng, Y. and Huemmrich, K.F., 2014. Relationship between fraction of radiation absorbed by photosynthesizing maize and soybean canopies and NDVI from remotely sensed data taken at close range and from MODIS 250 m resolution data. *Remote Sensing of Environment*, 147: 108-120.
- Göbel, L., Coners, H., Hertel, D., Willinghöfer, S. and Leuschner, C., 2019. The role of low soil temperature for photosynthesis and stomatal conductance of three graminoids from different elevations. *Frontiers in plant science*, 10: 330.
- González-Dugo, M., Moran, M., Mateos, L. and Bryant, R., 2006. Canopy temperature variability as an indicator of crop water stress severity. *Irrigation Science*, 24(4): 233.
- Goodbody, T.R., Tompalski, P., Coops, N.C., Hopkinson, C., Treitz, P. and van Ewijk, K., 2020. Forest inventory and diversity attribute modelling using structural and intensity metrics from multi-spectral airborne laser scanning data. *Remote Sensing*, 12(13), p.2109.
- Guo, Y., Yin, G., Sun, H., Wang, H., Chen, S., Senthilnath, J., Wang, J. and Fu, Y., 2020. Scaling Effects on Chlorophyll Content Estimations with RGB Camera Mounted on a UAV Platform Using Machine-Learning Methods. *Sensors*, 20(18): 5130.
- Haarhoff, S.J., Kotzé, T.N. and Swanepoel, P.A., 2020. A prospectus for sustainability of rainfed maize production systems in South Africa. *Crop Science*, 60(1): 14-28.
- Haboudane, D., Miller, J.R., Tremblay, N., Zarco-Tejada, P.J. and Dextraze, L., 2002. Integrated narrow-band vegetation indices for prediction of crop chlorophyll content for application to precision agriculture. *Remote sensing of environment*, 81(2-3): 416-426.
- Haghighian, F., Yousefi, S. and Keesstra, S., 2020. Identifying tree health using sentinel-2 images: a case study on *Tortrix viridana* L. infected oak trees in Western Iran. *Geocarto International*: 1-11.
- Han, L., Yang, G., Dai, H., Xu, B., Yang, H., Feng, H., Li, Z. and Yang, X., 2019. Modeling maize above-ground biomass based on machine learning approaches using UAV remote-sensing data. *Plant Methods*, 15(1): 1-19.
- Handiganoor, M.G., Patil, S. and Vasudevan, S., 2018. Effect of Seed Coating Polymer and Micronutrients on Stomatal Conductance and Resistance at Different Growth Stages of Pigeonpea. *Advances in Research*: 1-8.
- Hasanuzzaman, M., Nahar, K., Alam, M., Roychowdhury, R. and Fujita, M., 2013. Physiological, biochemical, and molecular mechanisms of heat stress tolerance in plants. *International journal of molecular sciences*, 14(5): 9643-9684.
- Hassanijalilian, O., Igathinathane, C., Doetkott, C., Bajwa, S., Nowatzki, J. and Esmaeili, S.A.H., 2020. Chlorophyll estimation in soybean leaves infield with smartphone digital imaging and machine learning. *Computers and Electronics in Agriculture*, 174: 105433.
- Hernández-Clemente, R., Hornero, A., Mottus, M., Peñuelas, J., González-Dugo, V., Jiménez, J., Suárez, L., Alonso, L. and Zarco-Tejada, P.J., 2019. Early diagnosis of vegetation health from high-resolution hyperspectral and thermal imagery: Lessons learned from empirical relationships and radiative transfer modelling. *Current forestry reports*, 5(3): 169-183.
- Hoffmann, H., Jensen, R., Thomsen, A., Nieto, H., Rasmussen, J. and Friborg, T., 2016. Crop water stress maps for an entire growing season from visible and thermal UAV imagery. *Biogeosciences*, 13(24): 6545-6563.

- Houshmandfar, A., O'Leary, G., Fitzgerald, G.J., Chen, Y., Tausz-Posch, S., Benke, K., Uddin, S. and Tausz, M., 2021. Machine learning produces higher prediction accuracy than the Jarvis-type model of climatic control on stomatal conductance in a dryland wheat agro-ecosystem. *Agricultural and Forest Meteorology*, 304: 108423.
- Hu, P., Chapman, S.C. and Zheng, B., 2021. Coupling of machine learning methods to improve estimation of ground coverage from unmanned aerial vehicle (UAV) imagery for high-throughput phenotyping of crops. *Functional Plant Biology*.
- Hutton, J., Lipa, G., Baustian, D., Sulik, J. and Bruce, R., 2020. High Accuracy Direct Georeferencing of the Altum Multi-Spectral Uav Camera and its Application to High Throughput Plant Phenotyping. *The International Archives of Photogrammetry, Remote Sensing and Spatial Information Sciences*, 43: 451-456.
- Jackson, R.D., Idso, S., Reginato, R. and Pinter Jr, P., 1981. Canopy temperature as a crop water stress indicator. *Water resources research*, 17(4): 1133-1138.
- Jamshidi, S., Zand-Parsa, S. and Niyogi, D., 2021. Assessing crop water stress index of citrus using in-situ measurements, Landsat, and Sentinel-2 Data. *International Journal of Remote Sensing*, 42(5): 1893-1916.
- Kamara, A., Conteh, A., Rhodes, E.R. and Cooke, R.A., 2019. The relevance of smallholder farming to African agricultural growth and development. *African Journal of Food, Agriculture, Nutrition and Development*, 19(1): 14043-14065.
- Kanning, M., Kühling, I., Trautz, D. and Jarmer, T., 2018. High-resolution UAV-based hyperspectral imagery for LAI and chlorophyll estimations from wheat for yield prediction. *Remote Sensing*, 10(12): 2000.
- Kayet, N., Pathak, K., Chakrabarty, A. and Sahoo, S., 2016. Urban heat island explored by co-relationship between land surface temperature vs multiple vegetation indices. *Spatial Information Research*, 24(5): 515-529.
- Khan, Z., Rahimi-Eichi, V., Haefele, S., Garnett, T. and Miklavcic, S.J., 2018. Estimation of vegetation indices for high-throughput phenotyping of wheat using aerial imaging. *Plant methods*, 14(1): 1-11.
- Kooistra, L. and Clevers, J.G., 2016. Estimating potato leaf chlorophyll content using ratio vegetation indices. *Remote Sensing Letters*, 7(6): 611-620.
- Kumar, A. and Sharma, P., 2013. Impact of climate variation on agricultural productivity and food security in rural India, *Economics Discussion Papers*.
- Kurukulasuriya, P. and Ajwad, M.I., 2007. Application of the Ricardian technique to estimate the impact of climate change on smallholder farming in Sri Lanka. *Climatic Change*, 81(1): 39-59.
- Li, F., Kang, S. and Zhang, J., 2004. Interactive effects of elevated CO₂, nitrogen and drought on leaf area, stomatal conductance, and evapotranspiration of wheat. *Agricultural Water Management*, 67(3): 221-233.
- Li, X., Liu, X., Liu, M., Wang, C. and Xia, X., 2015. A hyperspectral index sensitive to subtle changes in the canopy chlorophyll content under arsenic stress. *International Journal of Applied Earth Observation and Geoinformation*, 36: 41-53.
- Liang, L., Di, L., Huang, T., Wang, J., Lin, L., Wang, L. and Yang, M., 2018. Estimation of leaf nitrogen content in wheat using new hyperspectral indices and a random forest regression algorithm. *Remote Sensing*, 10(12): 1940.
- Lickley, M. and Solomon, S., 2018. Drivers, timing and some impacts of global aridity change. *Environmental Research Letters*, 13(10): 104010.
- Ling, Q., Huang, W. and Jarvis, P., 2011. Use of a SPAD-502 meter to measure leaf chlorophyll concentration in *Arabidopsis thaliana*. *Photosynthesis research*, 107(2): 209-214.
- Lipper, L., Thornton, P., Campbell, B.M., Baedeker, T., Braimoh, A., Bwalya, M., Caron, P., Cattaneo, A., Garrity, D. and Henry, K., 2014. Climate-smart agriculture for food security. *Nature climate change*, 4(12): 1068-1072.
- Lu, H.-d., Xue, J.-q. and Guo, D.-w., 2017. Efficacy of planting date adjustment as a cultivation strategy to cope with drought stress and increase rainfed maize yield and water-use efficiency. *Agricultural Water Management*, 179: 227-235.
- Luan, J., Zhang, C., Xu, B., Xue, Y. and Ren, Y., 2020. The predictive performances of random forest models with limited sample size and different species traits. *Fisheries Research*, 227: 105534.

- Maes, W.H. and Steppe, K., 2019. Perspectives for remote sensing with unmanned aerial vehicles in precision agriculture. *Trends in plant science*, 24(2): 152-164.
- Manfreda, S., McCabe, M.F., Miller, P.E., Lucas, R., Pajuelo Madrigal, V., Mallinis, G., Ben Dor, E., Helman, D., Estes, L. and Ciraolo, G., 2018. On the use of unmanned aerial systems for environmental monitoring. *Remote sensing*, 10(4): 641.
- Mangus, D.L., Sharda, A. and Zhang, N., 2016. Development and evaluation of thermal infrared imaging system for high spatial and temporal resolution crop water stress monitoring of corn within a greenhouse. *Computers and Electronics in Agriculture*, 121: 149-159.
- Markwell, J., Osterman, J.C. and Mitchell, J.L., 1995. Calibration of the Minolta SPAD-502 leaf chlorophyll meter. *Photosynthesis research*, 46(3): 467-472.
- Matongera, T.N., Mutanga, O., Dube, T. and Sibanda, M., 2017. Detection and mapping the spatial distribution of bracken fern weeds using the Landsat 8 OLI new generation sensor. *International journal of applied earth observation and geoinformation*, 57: 93-103.
- Messina, G. and Modica, G., 2020. Applications of UAV thermal imagery in precision agriculture: State of the art and future research outlook. *Remote Sensing*, 12(9): 1491.
- Miao, Y., Mulla, D.J., Randall, G.W., Vetsch, J.A. and Vintila, R., 2009. Combining chlorophyll meter readings and high spatial resolution remote sensing images for in-season site-specific nitrogen management of corn. *Precision Agriculture*, 10(1): 45-62.
- Miller, I.J., Schieber, B., De Bey, Z., Benner, E., Ortiz, J.D., Girdner, J., Patel, P., Coradazzi, D.G., Henriques, J. and Forsyth, J., 2020. Analyzing crop health in vineyards through a multispectral imaging and drone system, 2020 Systems and Information Engineering Design Symposium (SIEDS). IEEE, pp. 1-5.
- Mutanga, O., Adam, E. and Cho, M.A., 2012. High density biomass estimation for wetland vegetation using WorldView-2 imagery and random forest regression algorithm. *International Journal of Applied Earth Observation and Geoinformation*, 18: 399-406.
- Muzari, W., Gatsi, W. and Muvhunzi, S., 2012. The impacts of technology adoption on smallholder agricultural productivity in sub-Saharan Africa: A review. *Journal of Sustainable Development*, 5(8): 69.
- Naito, H., Ogawa, S., Valencia, M.O., Mohri, H., Urano, Y., Hosoi, F., Shimizu, Y., Chavez, A.L., Ishitani, M. and Selvaraj, M.G., 2017. Estimating rice yield related traits and quantitative trait loci analysis under different nitrogen treatments using a simple tower-based field phenotyping system with modified single-lens reflex cameras. *ISPRS Journal of Photogrammetry and Remote Sensing*, 125: 50-62.
- Nejad, T.S., 2011. Effect of drought stress on stomata resistance changes in corn. *Journal of American Science*, 7(9): 27-31.
- Nhamo, L., Magidi, J., Nyamugama, A., Clulow, A.D., Sibanda, M., Chimonyo, V.G. and Mabhaudhi, T., 2020. Prospects of Improving Agricultural and Water Productivity through Unmanned Aerial Vehicles. *Agriculture*, 10(7): 256.
- Nhamo, L., Matchaya, G., Mabhaudhi, T., Nhlengethwa, S., Nhemachena, C. and Mpandeli, S., 2019. Cereal production trends under climate change: Impacts and adaptation strategies in southern Africa. *Agriculture*, 9(2): 30.
- Nhamo, L., Van Dijk, R., Magidi, J., Wiberg, D. and Tshikolomo, K., 2018. Improving the accuracy of remotely sensed irrigated areas using post-classification enhancement through UAV capability. *Remote Sensing*, 10(5): 712.
- Nicholls, C.I., Altieri, M.A., Dezanet, A., Lana, M., Feistauer, D. and Ouriques, M., 2004. A rapid, farmer-friendly agroecological method to estimate soil quality and crop health in vineyard systems. *Biodynamics*: 33-39.
- Niu, H., Zhao, T., Wang, D. and Chen, Y., 2019. Estimating evapotranspiration with UAVs in agriculture: A review, 2019 ASABE Annual International Meeting. American Society of Agricultural and Biological Engineers, pp. 1.
- Noi, P.T., Degener, J. and Kappas, M., 2017. Comparison of multiple linear regression, cubist regression, and random forest algorithms to estimate daily air surface temperature from dynamic combinations of MODIS LST data. *Remote Sensing*, 9(5): 398.

- Okonya, J.S., Syndikus, K. and Kroschel, J., 2013. Farmers' perception of and coping strategies to climate change: Evidence from six agro-ecological zones of Uganda. *Journal of agricultural science*, 5(8): 252.
- Osakabe, Y., Osakabe, K., Shinozaki, K. and Tran, L.-S.P., 2014. Response of plants to water stress. *Frontiers in plant science*, 5: 86.
- Panigrahi, N. and Das, B., 2018. Canopy spectral reflectance as a predictor of soil water potential in rice. *Water Resources Research*, 54(4): 2544-2560.
- Park, S., Ryu, D., Fuentes, S., Chung, H., Hernández-Montes, E. and O'Connell, M., 2017. Adaptive estimation of crop water stress in nectarine and peach orchards using high-resolution imagery from an unmanned aerial vehicle (UAV). *Remote Sensing*, 9(8): 828.
- Pasqualotto, N., Delegido, J., Van Wittenberghe, S., Verrelst, J., Rivera, J.P. and Moreno, J., 2018. Retrieval of canopy water content of different crop types with two new hyperspectral indices: Water Absorption Area Index and Depth Water Index. *International journal of applied earth observation and geoinformation*, 67: 69-78.
- Peñuelas, J., Filella, I., Biel, C., Serrano, L. and Save, R., 1993. The reflectance at the 950–970 nm region as an indicator of plant water status. *International journal of remote sensing*, 14(10): 1887-1905.
- Pinter Jr, P.J., Hatfield, J.L., Schepers, J.S., Barnes, E.M., Moran, M.S., Daughtry, C.S. and Upchurch, D.R., 2003. Remote sensing for crop management. *Photogrammetric Engineering & Remote Sensing*, 69(6): 647-664.
- Prakash, A., 2000. Thermal remote sensing: concepts, issues and applications. *International Archives of Photogrammetry and Remote Sensing*, 33(B1; PART 1): 239-243.
- Psirofonía, P., Samaritakis, V., Eliopoulos, P. and Potamitis, I., 2017. Use of unmanned aerial vehicles for agricultural applications with emphasis on crop protection: Three novel case-studies. *International Journal of Agricultural Science and Technology*, 5(1): 30-39.
- Qiu, Z., Xiang, H., Ma, F. and Du, C., 2020. Qualifications of rice growth indicators optimized at different growth stages using unmanned aerial vehicle digital imagery. *Remote Sensing*, 12(19): 3228.
- Ramos, A.P.M., Osco, L.P., Furuya, D.E.G., Gonçalves, W.N., Santana, D.C., Teodoro, L.P.R., da Silva Junior, C.A., Capristo-Silva, G.F., Li, J. and Baio, F.H.R., 2020. A random forest ranking approach to predict yield in maize with uav-based vegetation spectral indices. *Computers and Electronics in Agriculture*, 178: 105791.
- Raper, T. and Varco, J., 2015. Canopy-scale wavelength and vegetative index sensitivities to cotton growth parameters and nitrogen status. *Precision Agriculture*, 16(1): 62-76.
- Rockstrom, J., 2000. Water resources management in smallholder farms in Eastern and Southern Africa: An overview. *Physics and Chemistry of the Earth, Part B: Hydrology, Oceans and Atmosphere*, 25(3): 275-283.
- Rostami, M., Koocheki, A.R., Mahallati, M.N. and Kafi, M., 2008. Evaluation of chlorophyll meter (SPAD) data for prediction of nitrogen status in corn (*Zea mays* L.). *American-Eurasian Journal Agriculture Science*, 3(1): 79-85.
- Salami, A., Kamara, A.B. and Brixiova, Z., 2010. Smallholder agriculture in East Africa: Trends, constraints and opportunities. African Development Bank Tunis.
- Sandbrook, C., 2015. The social implications of using drones for biodiversity conservation. *Ambio*, 44(4): 636-647.
- Sankaran, S., Maja, J.M., Buchanon, S. and Ehsani, R., 2013. Huanglongbing (citrus greening) detection using visible, near infrared and thermal imaging techniques. *Sensors*, 13(2): 2117-2130.
- Saseendran, S., Trout, T., Ahuja, L., Ma, L., McMaster, G., Nielsen, D., Andales, A., Chávez, J. and Ham, J., 2015. Quantifying crop water stress factors from soil water measurements in a limited irrigation experiment. *Agricultural Systems*, 137: 191-205.
- Sepulcre-Cantó, G., Zarco-Tejada, P., Sobrino, J., Jiménez-Muñoz, J. and Villalobos, F., 2005. Spatial variability of crop water stress in an olive grove with high-spatial thermal remote sensing imagery. *Proc. Precision Agric*: 267-272.

- Shi, Y., Thomasson, J.A., Murray, S.C., Pugh, N.A., Rooney, W.L., Shafian, S., Rajan, N., Rouze, G., Morgan, C.L. and Neely, H.L., 2016. Unmanned aerial vehicles for high-throughput phenotyping and agronomic research. *PloS one*, 11(7): e0159781.
- Sibanda, M., Mutanga, O., Dube, T. and Mafongoya, P.L., 2020. Spectrometric proximally sensed data for estimating chlorophyll content of grasslands treated with complex fertilizer combinations. *Journal of Applied Remote Sensing*, 14(2): 024517.
- Sibanda, M., Onisimo, M., Dube, T. and Mabhaudhi, T., 2021. Quantitative assessment of grassland foliar moisture parameters as an inference on rangeland condition in the mesic rangelands of southern Africa. *International Journal of Remote Sensing*, 42(4): 1474-1491.
- Singhal, G., Bansod, B., Mathew, L., Goswami, J., Choudhury, B. and Raju, P., 2019. Chlorophyll estimation using multi-spectral unmanned aerial system based on machine learning techniques. *Remote Sensing Applications: Society and Environment*, 15: 100235.
- Sishodia, R.P., Ray, R.L. and Singh, S.K., 2020. Applications of remote sensing in precision agriculture: A review. *Remote Sensing*, 12(19): 3136.
- Slagter, B., Tsendbazar, N.-E., Vollrath, A. and Reiche, J., 2020. Mapping wetland characteristics using temporally dense Sentinel-1 and Sentinel-2 data: A case study in the St. Lucia wetlands, South Africa. *International Journal of Applied Earth Observation and Geoinformation*, 86: 102009.
- Song, Y., Birch, C., Qu, S., Doherty, A. and Hanan, J., 2010. Analysis and modelling of the effects of water stress on maize growth and yield in dryland conditions. *Plant Production Science*, 13(2): 199-208.
- Soropa, G., Gwatibaya, S., Musiyiwa, K., Rusere, F., Mavima, G. and Kasasa, P., 2015. Indigenous knowledge system weather forecasts as a climate change adaptation strategy in smallholder farming systems of Zimbabwe: Case study of Murehwa, Tsholotsho and Chiredzi districts. *African Journal of Agricultural Research*, 10(10): 1067-1075.
- Taghizadeh-Mehrjardi, R., Mahdianpari, M., Mohammadimanesh, F., Behrens, T., Toomanian, N., Scholten, T. and Schmidt, K., 2020. Multi-task convolutional neural networks outperformed random forest for mapping soil particle size fractions in central Iran. *Geoderma*, 376: 114552.
- Taghvaeian, S., Chávez, J.L., Bausch, W.C., DeJonge, K.C. and Trout, T.J., 2014. Minimizing instrumentation requirement for estimating crop water stress index and transpiration of maize. *Irrigation Science*, 32(1): 53-65.
- Tahir, M.N., Naqvi, S.Z.A., Lan, Y., Zhang, Y., Wang, Y., Afzal, M., Cheema, M.J.M. and Amir, S., 2018. Real time estimation of chlorophyll content based on vegetation indices derived from multispectral UAV in the kinnow orchard. *International Journal of Precision Agricultural Aviation*, 1(1).
- Tefera, T., Kanampiu, F., De Groote, H., Hellin, J., Mugo, S., Kimenju, S., Beyene, Y., Boddupalli, P.M., Shiferaw, B. and Banziger, M., 2011. The metal silo: An effective grain storage technology for reducing post-harvest insect and pathogen losses in maize while improving smallholder farmers' food security in developing countries. *Crop protection*, 30(3): 240-245.
- Terashima, I., Fujita, T., Inoue, T., Chow, W.S. and Oguchi, R., 2009. Green light drives leaf photosynthesis more efficiently than red light in strong white light: revisiting the enigmatic question of why leaves are green. *Plant and cell physiology*, 50(4): 684-697.
- Thamaga-Chitja, J.M. and Morojele, P., 2014. The context of smallholder farming in South Africa: Towards a livelihood asset building framework. *Journal of Human Ecology*, 45(2): 147-155.
- Timothy, D., Onisimo, M. and Riyad, I., 2016. Quantifying aboveground biomass in African environments: A review of the trade-offs between sensor estimation accuracy and costs. *Tropical Ecology*, 57(3): 393-405.
- Ubisi, N.R., Mafongoya, P.L., Kolanisi, U. and Jiri, O., 2017. Smallholder farmer's perceived effects of climate change on crop production and household livelihoods in rural Limpopo province, South Africa. *Change and Adaptation in Socio-Ecological Systems*, 3(1): 27-38.
- Uddling, J., Gelang-Alfredsson, J., Piikki, K. and Pleijel, H., 2007. Evaluating the relationship between leaf chlorophyll concentration and SPAD-502 chlorophyll meter readings. *Photosynthesis research*, 91(1): 37-46.
- Unganai, L.S. and Murwira, A., 2010. Challenges and opportunities for climate change adaptation among smallholder farmers in southeast Zimbabwe, 2nd International Conference: Climate,

- Sustainability and Development in Semi-arid Regions, Ceará Convention Center, Fortaleza, pp. 16-20.
- Ustin, S.L. and Jacquemoud, S., 2020. How the optical properties of leaves modify the absorption and scattering of energy and enhance leaf functionality, Remote sensing of plant biodiversity. Springer, Cham, pp. 349-384.
- van der Vyver, C. and Peters, S., 2017. How do plants deal with dry days? *Front. Young Minds*, 5: 58.
- Vanlauwe, B., Coyne, D., Gockowski, J., Hauser, S., Huising, J., Masso, C., Nziguheba, G., Schut, M. and Van Asten, P., 2014. Sustainable intensification and the African smallholder farmer. *Current Opinion in Environmental Sustainability*, 8(0): 15-22.
- Veysi, S., Naseri, A.A., Hamzeh, S. and Bartholomeus, H., 2017. A satellite based crop water stress index for irrigation scheduling in sugarcane fields. *Agricultural water management*, 189: 70-86.
- Vincini, M. and Frazzi, E., 2011. Comparing narrow and broad-band vegetation indices to estimate leaf chlorophyll content in planophile crop canopies. *Precision Agriculture*, 12(3): 334-344.
- Vitrack-Tamam, S., Holtzman, L., Dagan, R., Levi, S., Tadmor, Y., Azizi, T., Rabinovitz, O., Naor, A. and Liran, O., 2020. Random Forest Algorithm Improves Detection of Physiological Activity Embedded within Reflectance Spectra Using Stomatal Conductance as a Test Case. *Remote Sensing*, 12(14): 2213.
- Vorovencii, I., 2009. The hyperspectral sensors used in satellite and aerial remote sensing. *Bulletin of the Transilvania University of Brasov. Forestry, Wood Industry, Agricultural Food Engineering. Series II*, 2: 51.
- Walker, B.J., Drewry, D.T., Slattery, R.A., VanLoocke, A., Cho, Y.B. and Ort, D.R., 2018. Chlorophyll can be reduced in crop canopies with little penalty to photosynthesis. *Plant Physiology*, 176(2): 1215-1232.
- Walker, N. and Schulze, R., 2006. An assessment of sustainable maize production under different management and climate scenarios for smallholder agro-ecosystems in KwaZulu-Natal, South Africa. *Physics and Chemistry of the Earth, Parts A/B/C*, 31(15-16): 995-1002.
- Waring, R. and Landsberg, J., 2011. Generalizing plant–water relations to landscapes. *Journal of Plant Ecology*, 4(1-2): 101-113.
- Whitford, W.G., De Soya, A.G., Van Zee, J.W., Herrick, J.E. and Havstad, K.M., 1998. Vegetation, soil, and animal indicators of rangeland health. *Environmental Monitoring and Assessment*, 51(1): 179-200.
- Wiratmoko, D., Prasetyo, A.E., Jatmiko, R.H., Yusuf, M.A. and Rahutomo, S., 2018. Identification of *Ganoderma boninense* infection levels on oil palm using vegetation index. *International Journal of Oil Palm*, 1(3): 110-120.
- Wu, B., Meng, J., Li, Q., Yan, N., Du, X. and Zhang, M., 2014. Remote sensing-based global crop monitoring: experiences with China's CropWatch system. *International Journal of Digital Earth*, 7(2): 113-137.
- Wu, C., Niu, Z., Tang, Q. and Huang, W., 2008. Estimating chlorophyll content from hyperspectral vegetation indices: Modeling and validation. *Agricultural and forest meteorology*, 148(8-9): 1230-1241.
- Xiang, H. and Tian, L., 2011. Development of a low-cost agricultural remote sensing system based on an autonomous unmanned aerial vehicle (UAV). *Biosystems engineering*, 108(2): 174-190.
- Xue, J. and Su, B., 2017. Significant remote sensing vegetation indices: A review of developments and applications. *Journal of sensors*, 2017.
- Yang, J. and Du, X., 2017. An enhanced water index in extracting water bodies from Landsat TM imagery. *Annals of GIS*, 23(3): 141-148.
- Yao, D., Yang, J. and Zhan, X., 2013. An improved random forest algorithm for class-imbalanced data classification and its application in PAD risk factors analysis. *The Open Electrical & Electronic Engineering Journal*, 7(1).
- Yordanov, I., Tsonev, T., Goltsev, V., Kruleva, L. and Velikova, V., 1997. Interactive effect of water deficit and high temperature on photosynthesis of sunflower and maize plants. 1. Changes in parameters of chlorophyll fluorescence induction kinetics and fluorescence quenching. *Photosynthetica*, 33(3): 391-402.

- Yun, S.K., Kim, S.J., Nam, E.Y., Kwon, J.H., Do, Y.S., Song, S.-Y., Kim, M., Choi, Y., Kim, G. and Shin, H., 2020. Evaluation of water stress using canopy temperature and crop water stress index (CWSI) in peach trees. *Protected Horticulture and Plant Factory*, 29(1): 20-27.
- Zarco-Tejada, P.J., González-Dugo, V. and Berni, J.A., 2012. Fluorescence, temperature and narrow-band indices acquired from a UAV platform for water stress detection using a micro-hyperspectral imager and a thermal camera. *Remote sensing of environment*, 117: 322-337.
- Zarco-Tejada, P.J., Pushnik, J., Dobrowski, S. and Ustin, S., 2003. Steady-state chlorophyll a fluorescence detection from canopy derivative reflectance and double-peak red-edge effects. *Remote Sensing of Environment*, 84(2): 283-294.
- Zhang, F. and Zhou, G., 2015. Estimation of canopy water content by means of hyperspectral indices based on drought stress gradient experiments of maize in the north plain China. *Remote Sensing*, 7(11): 15203-15223.
- Zhang, F. and Zhou, G., 2019. Estimation of vegetation water content using hyperspectral vegetation indices: A comparison of crop water indicators in response to water stress treatments for summer maize. *BMC ecology*, 19(1): 18.
- Zhang, L., Niu, Y., Zhang, H., Han, W., Li, G., Tang, J. and Peng, X., 2019a. Maize canopy temperature extracted from UAV thermal and RGB imagery and its application in water stress monitoring. *Frontiers in plant science*, 10: 1270.
- Zhang, L., Zhang, H., Niu, Y. and Han, W., 2019b. Mapping maize water stress based on UAV multispectral remote sensing. *Remote Sensing*, 11(6): 605.
- Zhang, X., He, Y., Wang, C., Xu, F., Li, X., Tan, C., Chen, D., Wang, G. and Shi, L., 2019c. Estimation of Corn Canopy Chlorophyll Content Using Derivative Spectra in the O₂-A Absorption Band. *Frontiers in plant science*, 10: 1047.
- Zhao, X., Tong, C., Pang, X., Wang, Z., Guo, Y., Du, F. and Wu, R., 2012. Functional mapping of ontogeny in flowering plants. *Briefings in bioinformatics*, 13(3): 317-328.

APPENDIX A

During the mid-vegetative growth stage, the lower portion of the field had not been weeded with the rest of the field which was weeded during the early vegetative stage. As a result, the maize crop in this portion of the field became visibly unhealthy and stressed. Figure 23a shows how the lower portion of the maize field appears more yellow in colour, due to the presence of grasses and weeds, as well as due to weed competition. Additionally, the soil found in the lower region of the field comprised of coarser sediment, which was a result of leaching and run-off deposition. Furthermore, the lower regions of slopes have been documented to obtain less nutrients and have less fertile soil.

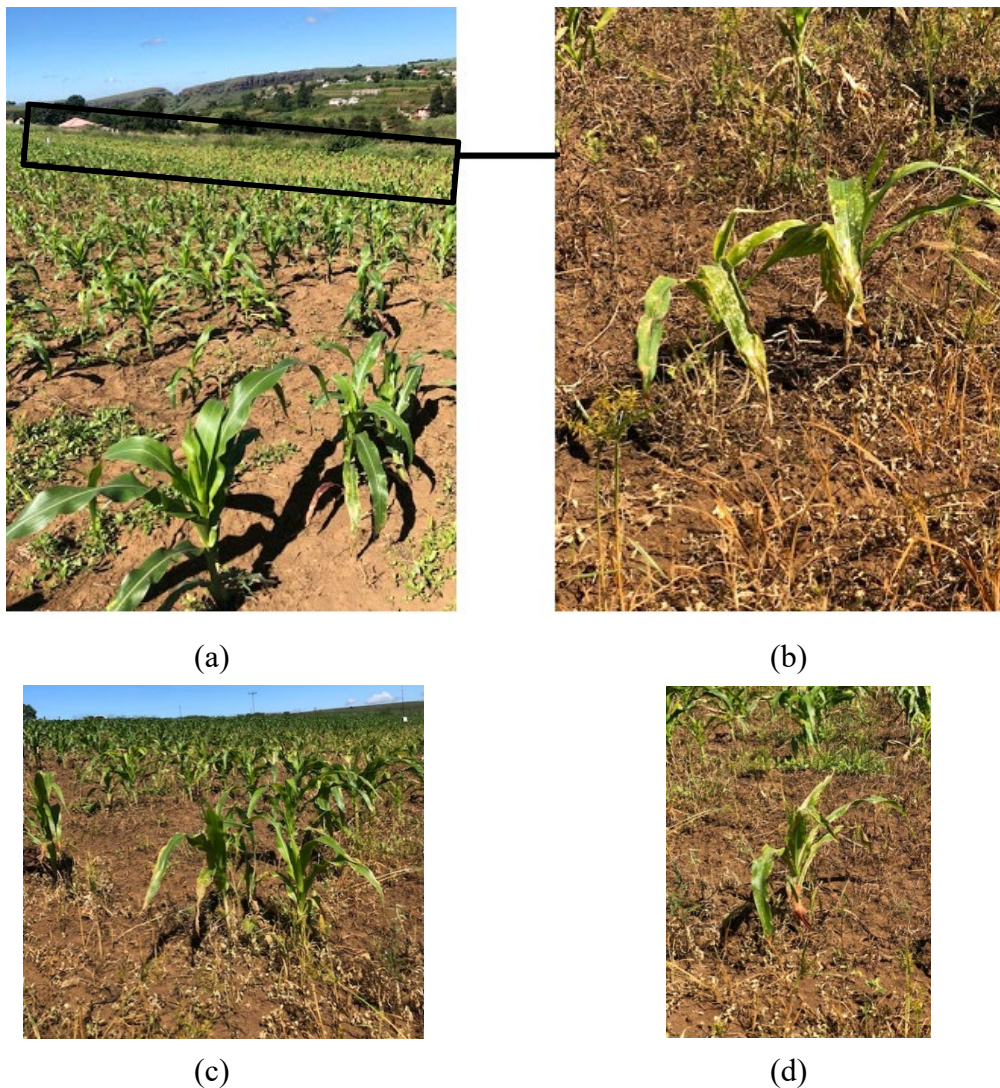


Figure 23 (a – d): Photographs of western portion of maize field (lower slope) where weeds/grasses were still present during mid-vegetative growth.

Furthermore, an unforeseen hailstorm on 23 April 2021 (DOY 114) damaged the maize foliar canopy structure. This resulted in foliar loss as leaves broke off the plant and began to senesce. The hail damage also introduced soil background exposure.



(a)



(b)

Figure 24: Photographs of maize (a) before the hailstorm, and (b) after hailstorm damaged the crop



Figure 25: Additional photographs of damaged maize foliar canopy due to the hailstorm